

<https://doi.org/10.15388/vu.thesis.789>

<https://orcid.org/0009-0008-8853-3368>

VILNIUS UNIVERSITY

CENTER FOR PHYSICAL SCIENCES AND TECHNOLOGY

Nadežda Traškina

# Preparation and Characterization of Active Components for Aqueous Sodium Ion Insertion Batteries

**DOCTORAL DISSERTATION**

Natural Sciences

Chemistry (N 003)

VILNIUS 2025

The dissertation was prepared between 2020 and 2025 at the Center for Physical Sciences and Technology in Vilnius, Lithuania.

**Academic supervisor** – Dr. Linas Vilčiauskas (Center for Physical Sciences and Technology, Natural Sciences, Chemistry, N 003)

This doctoral dissertation will be defended in a public meeting of the Dissertation Defence Panel:

**Chairman** – Prof. Dr. Artūras Katelnikovas (Vilnius University, Natural Sciences, Chemistry, N 003)

**Members:**

Prof. Dr. Aldona Beganskienė (Vilnius University, Natural Sciences, Chemistry, N 003),

Prof. Habil. Dr. Gediminas Niaura (Center for Physical Sciences and Technology, Natural Sciences, Chemistry, N 003),

Dr. Loreta Tamašauskaitė-Tamašiūnaitė (Center for Physical Sciences and Technology, Natural Sciences, Chemistry, N 003),

Dr. Sigita Trabesinger (Paul Scherrer Institute (Switzerland), Natural Sciences, Chemistry, N 003).

The dissertation shall be defended at a public meeting of the Dissertation Defence Panel at 14:00 1<sup>st</sup> of July 2025 in Room D401 of the Center for Physical Sciences and Technology.

Address: Saulėtekio al. 3, LT-10257, Vilnius, Lithuania.

Tel. +370 5 264 8884; e-mail: [office@ftmc.lt](mailto:office@ftmc.lt)

The text of this dissertation can be accessed at the library of the Vilnius University as well as on the website of Vilnius University:

[www.vu.lt/lt/naujienos/ivykiu-kalendorius](http://www.vu.lt/lt/naujienos/ivykiu-kalendorius)

<https://doi.org/10.15388/vu.thesis.789>

<https://orcid.org/0009-0008-8853-3368>

VILNIAUS UNIVERSITETAS  
FIZINIŲ IR TECHNOLOGIJOS MOKSLŲ CENTRAS

Nadežda Traškina

# Vandeninių natrio jonų įterpimo baterijų aktyvių komponentų paruošimas ir charakterizavimas

**DAKTARO DISERTACIJA**

Gamtos mokslai  
Chemija (N 003)

VILNIUS 2025

Disertacija rengta 2020–2025 metais Valstybiniame mokslinių tyrimų institute Fizinių ir technologijos mokslų centre.

**Mokslinis vadovas** – dr. Linas Vilčiauskas (Fizinių ir technologijos mokslų centras, gamtos mokslai, chemija, N 003).

Gynimo taryba:

**Pirmininkas** – prof. dr. Artūras Katelnikovas (Vilniaus universitetas, gamtos mokslai, chemija, N 003).

**Nariai:**

prof. dr. Aldona Beganskienė (Vilniaus universitetas, gamtos mokslai, chemija, N 003),

Prof. habil. dr. Gediminas Niaura (Fizinių ir technologijos mokslų centras, gamtos mokslai, chemija, N 003),

dr. Loreta Tamašauskaitė-Tamašiūnaitė (Fizinių ir technologijos mokslų centras, gamtos mokslai, chemija, N 003),

dr. Sigita Trabesinger (Paul Scherrer institutas (Šveicarija), gamtos mokslai, chemija, N 003).

Disertacija ginama viešame Gynimo tarybos posėdyje 2025 m. liepos mėn. 1 d. 14:00 val. Fizinių ir technologijos mokslų centro D401 auditorijoje.

Adresas: Saulėtekio al. 3, LT-10257, Vilnius, Lietuva.

Tel. +370 5 264 8884; el. paštas: [office@ftmc.lt](mailto:office@ftmc.lt).

Disertaciją galima peržiūrėti Vilniaus Universiteto bibliotekoje ir VU interneto svetainėje adresu:

<https://www.vu.lt/naujienos/ivykiu-kalendorius>



## LIST OF ABBREVIATIONS

ADP	Adenosine DiPhosphate
AM	Active Material
ASIB	Aqueous Sodium-ion Battery
a.u.	Arbitrary Unit
BET	Brunauer–Emmett–Teller
CA	Citric Acid
CB	Carbon Black
CE	Coulombic Efficiency
CS	Co-Solvents
CV	Cyclic Voltammetry
DA	Dopamine
DMSO	Dimethyl Sulfoxide
EC	Ethylene Carbonate
ECHA	EU Chemicals Agency
EDX	Energy-Dispersive X-ray Spectroscopy
ESW	Electrochemical Stability Window
FEC	Fluoroethylene Carbonate
FT-IR	Fourier-transform Infrared
GCD	Galvanostatic Charge/Discharge Cycling
HCF	Hexacyanoferrate
HER	Hydrogen Evolution Reaction
HMA	Hot-melt Adhesive
IPA	Isopropyl Alcohol
IPN	Interpenetrated Network
LIB	Lithium-ion Battery
LMO	Layered Metal Oxides
LSV	Linear Sweep Voltammetry
MSE	Mercury-mercurous Sulfate Electrode

NaFeHCF	Sodium Iron HexaCyanoFerrate
NASICON	Sodium SuperIonic Conductor
NaTFSI	Sodium bis(trifluoromethanesulfonyl)imide
NMP	N-methyl-2-pyrrolidone
NMR	Nuclear Magnetic Resonance
NTCDA	1,4,5,8-naphthalenetetracarboxylic Dianhydride
NTP	$\text{NaTi}_2(\text{PO}_4)_3$
NVP	$\text{Na}_3\text{V}_2(\text{PO}_4)_3$
NVPF	$\text{Na}_3\text{V}_2(\text{PO}_4)_2\text{F}_3$
NVTP	$\text{Na}_2\text{VTi}(\text{PO}_4)_3$
OCP	Open Circuit Potential
OER	Oxygen Evolution Reaction
ORR	Oxygen Reduction Reaction
PAA	Poly(acrylic acid)
PBA	Prussian Blue Analogue
PC	Propylene Carbonate
PDA	Polydopamine
PEVA	Poly(ethylene-co-vinyl acetate)
PFAS	Per- and Polyfluoroalkyl Substances
PS	1,3-propane sultone
PTFE	Polytetrafluoroethylene
PVA	Poly(vinyl alcohol)
PVBA	Poly(vinyl butyral-co-vinyl alcohol-co-vinyl acetate)
PVDF	Polyvinylidene Fluoride
RDE	Rotating Disc Electrode
SD	Self-Discharge
SEI	Solid Electrolyte Interphase
SEM	Scanning Electron Microscopy
SHE	Standard Hydrogen Electrode

SIB	Sodium-Ion Battery
TEM	Transmission Electron Microscopy
TGA	Thermogravimetric Analysis
TRIS	Tris(hydroxymethyl)aminomethane
WIS	Water-in-salt
XPS	X-ray Photoelectron Spectroscopy
XRD	X-ray Diffraction

## TABLE OF CONTENTS

LIST OF ABBREVIATIONS .....	5
INTRODUCTION.....	10
LITERATURE REVIEW.....	13
1.1. Current challenges.....	13
1.2. Electrochemical devices.....	14
1.3. “Rocking chair” batteries .....	15
1.4. Sodium-ion batteries .....	17
1.5. Aqueous sodium-ion batteries.....	18
Active materials for positive electrodes .....	18
Active materials for negative electrodes .....	19
Room for improvement .....	20
2. EXPERIMENTAL METHODOLOGY.....	22
2.1. Active material synthesis.....	22
2.2. Materials characterization .....	23
2.3. Electrode preparation .....	24
2.4. Electrochemical characterisation.....	25
3. RESULTS AND DISCUSSION.....	28
3.1. Carbon in electrodes.....	28
3.1.1. Carbon black .....	29
3.1.2. Particle carbon coating .....	30
Soluble carbohydrates .....	30
Polymer-derived coatings.....	33
3.1.3. Electrode preparation .....	43
3.1.4. Summary .....	48
3.2. Electrolyte solutions for aqueous batteries.....	49
3.2.1. Aqueous electrolytes .....	50

3.2.2. Hybrid aqueous electrolytes .....	55
Half-cells .....	60
Full cells .....	66
Capacity balanced full-cells .....	70
3.2.3. Organic solvent-based electrolytes.....	74
3.2.4. Summary .....	78
3.3. Electrode composite binders for aqueous batteries .....	80
3.3.1. Indirect (noncovalent) binders .....	81
Polyvinylidene fluoride .....	81
Polyimides .....	86
Poly(ethylene-co-vinyl acetate).....	89
3.3.2. Direct binders .....	90
Poly(vinyl butyral-co-vinyl alcohol-co-vinyl acetate) .....	91
Poly(vinyl alcohol-acrylic acid) .....	92
3.3.3. Summary .....	94
MAIN RESULTS AND CONCLUSIONS .....	96
SANTRAUKA .....	98
ACKNOWLEDGEMENTS .....	114
CURRICULUM VITAE .....	115
PUBLICATIONS AND CONFERENCES .....	117
LIST OF REFERENCES .....	119

## INTRODUCTION

As we transition to sustainable energy, efficient and safe storage systems become crucial. Aqueous sodium-ion batteries stand out as a promising alternative to traditional lithium-ion batteries for several reasons. Firstly, they use water-based electrolytes, which significantly enhance safety by reducing the risk of fire and explosion. Secondly, their raw materials, such as sodium, are abundant and inexpensive, lowering production costs and addressing resource scarcity concerns. Their environmental impact is also lower, avoiding the use of toxic and hazardous materials. Moreover, the unique chemistry of aqueous batteries offers high power density and long cycle life, making them ideal for a wide range of energy storage applications. Overall, aqueous sodium-ion batteries provide an affordable, safe, and environmentally friendly alternative for stationary energy storage.

NASICON (Na SuperIonic CONductor) materials are a class of electrode materials known for their high ionic conductivity and structural stability. They have a unique three-dimensional framework structure that allows for efficient sodium ion transport, making them ideal for use in sodium-ion batteries. These materials, however, face several challenges among which poor electronic conductivity and inferior stability in aqueous media.

The **main goal** of this work is to design, prepare, characterize, and optimize active components for aqueous sodium-ion batteries. Specifically, the active components are defined as the composite electrodes containing NASICON-structured materials such as  $\text{NaTi}_2(\text{PO}_4)_3$  and  $\text{Na}_2\text{VTi}(\text{PO}_4)_3$ , and electrolyte solutions based on aqueous simple salt systems. The optimization process is defined as the relevant preparation, formation, and modification steps necessary for the best electrochemical performance of these components in aqueous sodium-ion batteries.

The **specific objectives** of this work are as follows:

1. Develop and optimize preparation methods for composite  $\text{NaTi}_2(\text{PO}_4)_3$  electrodes in aqueous sodium-ion batteries, including carbon coating, slurry formulation, and electrode fabrication. Evaluate the influence of preparation processes on structural, morphological, and electrochemical properties.
2. Develop and optimize electrolyte solutions for aqueous sodium-ion batteries, using organic co-solvents and active additives to improve their stability and performance. Analyze these electrolytes using physico-chemical, spectroscopic, and electrochemical methods.
3. Identify, prepare, and characterize alternative polymeric binders with enhanced hydrophilicity for aqueous sodium-ion battery composite

electrodes. Evaluate their properties within the composite electrodes using physico-chemical and electrochemical methods.

The **novelty** of this work stems from the first focused attempt to investigate the influence of active battery components beyond the active material itself on the performance of aqueous sodium-ion batteries and the methods to optimize them. There is a very limited number of prior studies on these topics as most of the studies are primarily focused on the search and characterization of new electrode active phases. Moreover, most of the other studies of active battery components focused on organic-based electrolyte systems.

The **statements for the defence** are as follows:

1. The charge capacity and cycling stability of  $\text{NaTi}_2(\text{PO}_4)_3$  electrodes strongly depends on the active material particle carbon coating. Citric acid coating quality outperforms glucose due to differences in graphitization temperature. Polydopamine-derived coatings offer the most uniform and reproducible results, requiring only half of the carbon loading as that of citric acid pyrolysis to show similar capacity retention.

2. The optimal carbon black content in lab-scale  $\text{NaTi}_2(\text{PO}_4)_3$  electrodes is found to be 20 wt%. Hydraulic pressing at 6 t improves tap density and reduces porosity, enhancing electrochemical performance. A mixing protocol of 1 h dry premixing followed by 2 h slurry mixing ensures optimal carbon dispersion and electrode structure.

3. Self-discharge and pH increase in  $\text{NaTi}_2(\text{PO}_4)_3$  electrodes are mainly caused by  $\text{Ti}^{3+}$ -catalyzed oxygen reduction and hydrogen evolution. Alkaline conditions drive degradation, not through Ti dissolution but via formation of a surface-blocking, Ti-rich interphase. Oxygen removal and pH buffering improves capacity retention.

4. Organic co-solvents like glycerol and DMSO reduce water activity by altering hydrogen bonding, expanding the electrochemical stability window and suppressing gas evolution. This improves self-discharge and capacity retention. Full cells with  $\text{NaTi}_2(\text{PO}_4)_3\text{--Na}_{1.86}\text{Fe}[\text{Fe}(\text{CN})_6] \cdot 2.28\text{H}_2\text{O}$  benefit from wider operating voltage window. Additionally, small amounts of hydrazine successfully scavenge oxygen, enabling capacity-balanced  $\text{Na}_2\text{VTi}(\text{PO}_4)_3\text{--Na}_2\text{VTi}(\text{PO}_4)_3$  cells with enhanced capacity retention.

5. Electroactive polyimides like Kapton offer good electrode binding but poor adhesion to metal foils, likely due to their own electrochemical activity. PEVA ensures strong adhesion to stainless steel foil and good cycling performance, making it the most promising binder for aqueous systems. PVBA copolymer delivers great electrochemical performance, supports higher mass loadings and use of less toxic solvents; however, does not provide adhesion to metal foil current collector. PVA-acrylic acid copolymer shows

good retention but swells in alkaline conditions; however, its water solubility makes it the most eco-friendly option.



# LITERATURE REVIEW

## 1.1. Current challenges

The rising consumption of fossil fuels, world's primary energy source, and subsequent CO<sub>2</sub> pollution have led to the escalation of multiple environmental challenges associated with climate change to the point where urgent action is required (Fig. 1).<sup>1</sup> In order to align with the Paris climate agreement goals of future energy requirements, as well as the climate neutrality by 2050,<sup>2</sup> the development of renewable energy sources has become critical. Moreover, the historic reliance on gas from certain regions has made consumers particularly vulnerable to energy supply disruptions and price fluctuations.<sup>3</sup> Ongoing energy crisis powered by catastrophic levels of pollution, post-pandemic energy demand surge and geopolitical tensions have propelled the developments in renewable energy technologies.<sup>4</sup> While wind and solar turbines or solar panels offer green and safe energy, their intermittent nature requires large-scale energy storage solutions for grid stability.

Electrochemical energy storage offers an attractive solution with several advantages such as eco-friendly operation, high efficiency, versatile power and energy capabilities, durability, and uncomplicated integration into the existing grid infrastructure.<sup>5</sup> These attributes make electrochemical energy storage a key component in the transition to sustainable energy systems, capable of smoothing out the fluctuations in energy supply from renewable sources and ensuring a reliable and steady power supply.

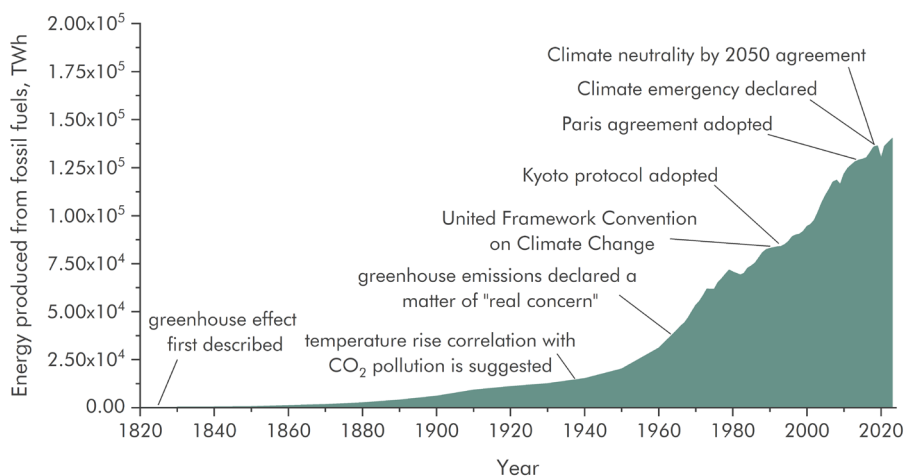


Figure 1. Energy produced from fossil fuels by year.<sup>6</sup>

## 1.2. Electrochemical devices

Battery cells, as electrochemical devices, effectively convert between chemical energy and electrical energy through oxidation-reduction reactions. Electrochemical energy storage has grown increasingly important, a trend that began in 1800 when Alessandro Volta constructed his “pile”.<sup>7</sup> This early battery featured alternating layers of copper and zinc, separated by tissue and connected by an electrolyte. While Volta's initial goal was to perform biological experiments, his pile laid the groundwork for modern batteries. The 19th and 20th centuries saw significant technological advances and the development of electrical applications, bringing electrical power sources to the forefront of research (Fig. 2). During this period, both non-rechargeable (primary) and rechargeable (secondary) batteries were developed.<sup>8</sup> An important feature of the latter is that reversing the electrochemical process can be carried out many times.<sup>9</sup> Among these, the lead-acid battery was a major breakthrough and remains a significant part of the battery market today.<sup>10</sup> Over 150 years ago, it powered the first electric vehicles, which were prevalent before combustion engines took over in the early 20th century. As technology progressed and electronic and mechanical applications diversified in the latter half of the 20th century, the demand for batteries with longer operation times, smaller size, lighter weight, rechargeability, high safety, and low cost increased.<sup>11</sup> This demand has driven chemists, physicists, materials scientists, and engineers to develop new battery designs and concepts that meet these evolving needs.

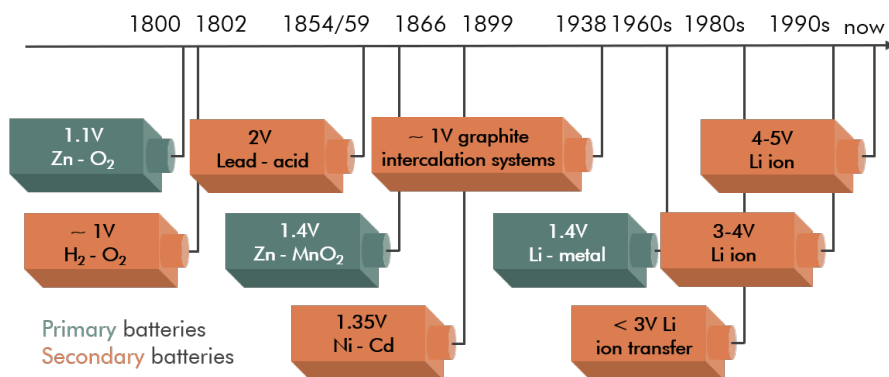


Figure 2. Development of battery technology over time.<sup>12</sup>

As illustrated in Fig. 3, the rechargeable electrochemical cell, a cornerstone of modern energy storage, comprises negative electrode, positive electrode

and electrolyte.<sup>13</sup> Typically, a separator is placed in between the electrodes submerged in electrolyte not allowing the physical contact and preventing shorting. Despite that, the electrodes are still connected ionically through the electrolyte and electronically by an external circuit.<sup>14</sup> During discharge, the negative electrode facilitates oxidation, while electrons travel through an external circuit to the positive electrode, enabling reduction. During both charge and discharge processes, the electrolyte conducts ions, thus, ensuring electro-neutrality.<sup>15</sup>

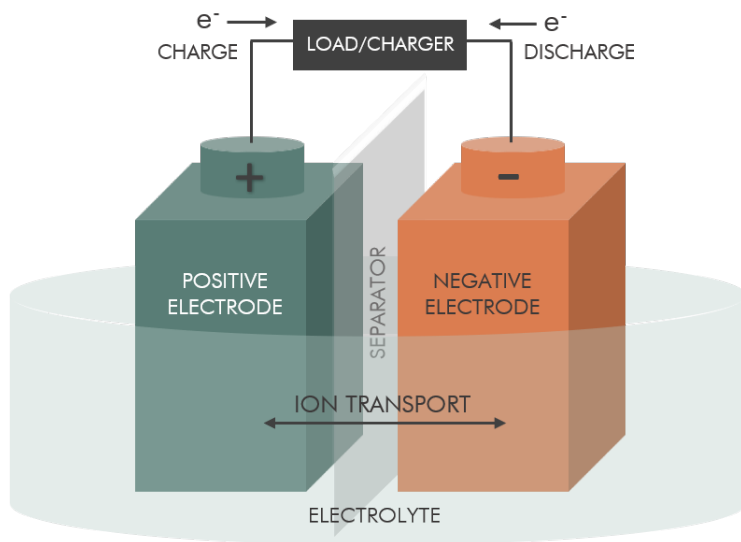


Figure 3. Schematic representation of rechargeable battery.

### 1.3. “Rocking chair” batteries

“Rocking chair” batteries are prominent electrochemical energy storage systems for both mobile and stationary applications owing to their long cycle life and impressive energy densities.<sup>16</sup> The “rocking chair” operational principle of majority modern batteries, is based on a charge carrier (ion) undergoing repeated insertion and de-insertion, shuttling back and forth between the electrodes through the internal circuit (electrolyte). Redox reactions taking place at the negative and positive electrodes yield electrons that produce a current by commuting through an external circuit.<sup>17</sup> Fig. 4 demonstrates the working principle of the most popular “rocking chair” battery – commercial lithium-ion battery (LIB).

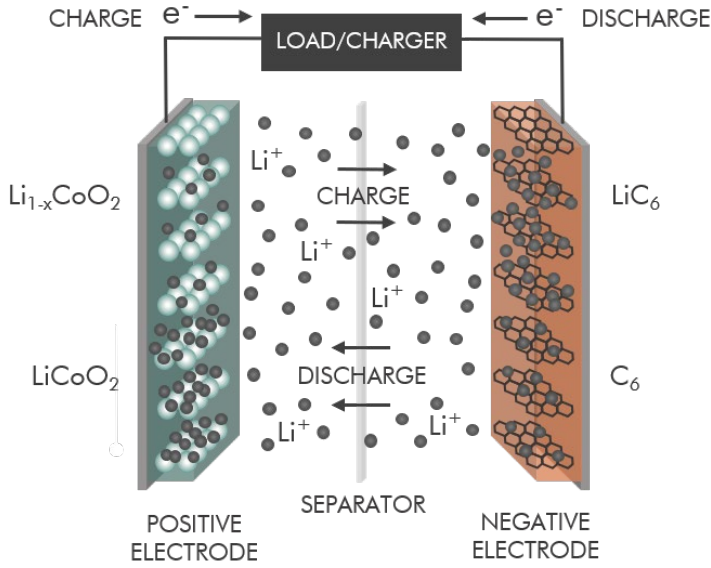
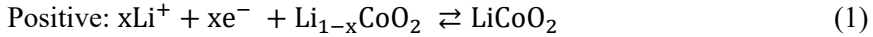


Figure 4. Schematic representation of a “rocking chair” Li-ion battery.

The reactions occurring during the charge/discharge processes can be written as follows:<sup>18</sup>



where  $\rightarrow$  represents discharging and  $\leftarrow$  charging processes of the battery.

Lithium ion battery – a Nobel Prize winning technology - offers high voltage, exceptional energy density, longer lifespan and rapid charging capabilities.<sup>8</sup> The steady advancements in this technology have contributed to the increased efficiency of portable devices and acceleration of the global transition towards sustainable transportation and grid solutions.<sup>19</sup> With the ongoing scientific efforts focused on enhancing performance and safety, LIBs are poised to maintain their flagship status.<sup>20</sup>

The increasing demand for lithium and its limited availability in remote or geopolitically sensitive regions present substantial challenges to its extraction, leading to volatile prices.<sup>21,22</sup> Additionally, cobalt and nickel, which are critical for the LIB industry, are either toxic or scarce.<sup>23</sup> This underlines the urgent need to discover novel, cost-effective, and abundant materials that are environmentally sustainable for the future generations of rechargeable batteries.

## 1.4. Sodium-ion batteries

Sodium, being the fourth most abundant metal within the Earth's crust (Fig. 5), is undeniably superior to lithium in terms of extraction and distribution. High abundance of sodium conditions a 30-fold lower cost of raw materials for SIBs than for those for LIBs.<sup>24</sup> Also, costly copper foil acting as current collector can be replaced by cheaper aluminum as sodium does not form alloys with the latter.<sup>25</sup> Furthermore, the manufacturing process and infrastructure installed for LIBs can be used for SIBs due to the similarities in charge storage, material and fabrication process.<sup>26</sup>

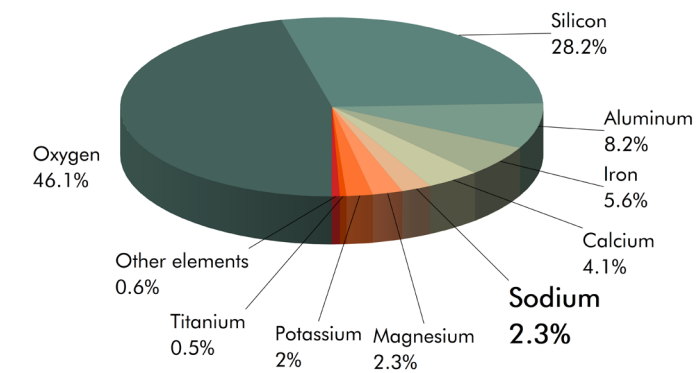


Figure 5. Abundance of the elements in the crust.<sup>27</sup>

In terms of safety, sodium ion batteries are way less susceptible to thermal runaway due to physical damage or overcharging. Hard carbon negative electrodes, often used in SIBs, are compatible with less flammable organic electrolytes resulting in enhanced safety characteristics.<sup>28</sup> Furthermore, SIBs do not require a particular state of charge for storing and transportation. The studies show, that prolonged periods of keeping SIBs at zero charge had minimal effects on overall electrochemical performance of the cell.

While sodium bears some resemblances to lithium, their differences result in different chemical properties and electrochemical performance.<sup>29</sup> Sodium ions, as opposed to ions of other alkaline group elements such as Li and K, cannot be stably and reversibly intercalated into graphitic structures resulting in diminished graphite capacities.<sup>30,31</sup>

The lack of anode as successful as graphite is partially responsible for underdevelopment of the SIB technology.<sup>32</sup> Also, larger atomic weight leads to diminished volumetric and gravimetric capacities, which accompanied by limited operational voltage is restricting the feasibility of SIBs for portable

and mobile applications.<sup>33</sup> However, safe, sustainable, and cost-effective SIBs with high-rate capabilities are fully capable of entering the market as candidates for large-scale stationary energy storage applications where the size of the energy storage device is not crucial.<sup>26,28,32</sup>

### 1.5. Aqueous sodium-ion batteries

Recently the aqueous modifications of SIBs have been paving their way as an appealing substitute to LIBs owing to the elimination of highly toxic and flammable organic electrolytes and cost-effectiveness.<sup>28,34</sup> Moreover, water-based electrolytes bring the prospects of recyclability to a completely new level, enabling re-employment of retired batteries.<sup>35</sup> Lower viscosities and superb ionic conductivities of aqueous electrolytes lead to higher rate capabilities than their organic counterparts.<sup>36,37</sup> More importantly, in terms of manufacturing, SIBs and LIBs are similar in terms of architecture, working mechanisms, components, and fabrication steps, which makes it easy for battery manufacturers to transfer the production lines of LIBs to SIBs.<sup>38</sup>

#### Active materials for positive electrodes

Generally, sodium ion positive electrodes can be divided into three categories:

- 1) **Layered metal oxides** (LMO) are composed of edge-sharing transition metal oxide [MeO<sub>6</sub>] octahedral sheets and with Na<sup>+</sup> ions squeezed between the layers. Many LMOs with a simple synthetic procedure, easily achieve capacities  $\geq 300 \text{ mAh g}^{-1}$ , and allow to use various low-price and nontoxic metals like manganese or iron.<sup>39,40</sup> Their practical applications, however, are hindered by poor stability, complex phase transitions and irreversible oxygen loss.<sup>41–44</sup> Moreover, they tend to exhibit moisture or air sensitivity and suffer from sodium deficiency, which requires complicated posttreatment procedures or sacrificial agents.<sup>45,46</sup>
- 2) **Prussian blue analogues** (PBAs) comprise hexacyanoferrate (HCF) units and transition metals forming a 3D structure, which is suited for accommodating alkali metal ions with minor volume deformation and efficient sodium transport.<sup>47</sup> Apart from excellent structural stability, PBAs offer economically feasible synthesis and abundant raw materials.<sup>48–50</sup> Additionally, PBAs feature two distinct redox pairs and, consequently, demonstrate decent specific capacities up to  $170 \text{ mAh g}^{-1}$  at  $25 \text{ mA g}^{-1}$ .<sup>51</sup> However, lattice defects arising from non-homogeneous nucleation rates taking place during co-precipitation reaction or

decomposition of structural water at high voltages might result in inferior cycle life and structural decay.<sup>52,53</sup>

- 3) **Polyanion-type** materials are composed of sodium, transition metal and a polyanion (phosphate, borate, sulphate, silicate, etc.).<sup>54</sup> These cathodes are characterized by excellent structural stability brought in by strong covalent bonds in polyanions.<sup>24,55</sup> Such materials usually exhibit higher redox potentials, but lower capacities than, for example, layered oxide compounds owing to their higher molar masses.<sup>28,56</sup> Another drawback of polyanions is their inferior electronic conductivity which hinders the electrochemical performance of the material.<sup>57</sup>

**Na Super Ionic Conductor (NASICON)** phosphate materials are a class of polyanionic compounds which can be generally described by a formula  $\text{Na}_x\text{M}_2(\text{PO}_4)_3$ , where  $x = 1 - 4$ , M is a transition metal/main group metal.<sup>58,59</sup> Depending on the oxidation states of involved elements, a structural formula unit can accommodate up to 4 alkali ions.<sup>60</sup> This type of materials are recognized for their high  $\text{Na}^+$  conductivity arising from durable 3-dimensional open framework, which provides abundance of channels for uninterrupted  $\text{Na}^+$  diffusion.<sup>61</sup>

### Active materials for negative electrodes

Recent research of negative electrodes for aqueous sodium-ion batteries (ASIBs) has mostly been focused on the same types of compounds as positive electrode materials as well as some promising organic materials. Among the most extensively studied materials are:

- 1)  $\text{NaTi}_2(\text{PO}_4)_3$  (NTP) with NASICON structure has been paired with various cathodes to assemble asymmetric high-performance batteries.<sup>62</sup> NTP with redox potential slightly more positive than that of hydrogen evolution reaction (HER) has a theoretical capacity of  $133 \text{ mAh g}^{-1}$  and expanded output voltage if the side reactions are properly mitigated.<sup>63</sup> However, NTP suffers from poor electronic conductivity and challenged diffusion kinetics as well as other materials of this kind.<sup>64</sup>
- 2) Majority of reported organic materials suitable for ASIBs are either small organic molecules with  $\text{C}=\text{O}$ ,  $\text{C}=\text{N}$  or  $\text{N}=\text{N}$  bond or polymers, whose inherent flexibility makes insertion and deinsertion of large  $\text{Na}^+$  ions easier. Azobenzene-4,4'-dicarboxylic acid sodium salt has been recently reported to exhibit a capacity of  $170 \text{ mAh g}^{-1}$  at 0.2 C, and a stable capacity of  $98 \text{ mAh g}^{-1}$  following 2000 cycles at 20 C. Quinone-based pyrene-4,5,9,10-tetraone anode paired with NVP cathode showed an

unprecedented reversible capacity of 201 mAh g<sup>-1</sup>, and retained 79% of capacity after 80 cycles at 1 C.<sup>65</sup> A full cell was assembled with polyimide derived from 1,4,5,8-naphthalenetetracarboxylic dianhydride (NTCDA) and LiCoO<sub>2</sub> exhibited a great capacity of 71 mAh g<sup>-1</sup> and an excellent rate capability and cycling stability.<sup>66</sup> Based on this study one can assume polyimide anodes exhibit potential for application in ASIBs.

### Room for improvement

Despite the rampant growth of academic attention, the application prospects are still clouded by drawbacks that are yet to be overcome. The main bottlenecks in commercialization of aqueous sodium ion batteries are:

**Poor electronic conductivity.** Most inorganic materials are, unfortunately, plagued by inherently poor electronic conductivity and slow diffusion processes in the framework.<sup>38</sup> The lack of efficient transport of electrons, results in unsatisfying capacity retentions, slow charge and discharge rate as well as energy losses due to increased internal resistance.<sup>67</sup>

**Electrochemical stability window (ESW).** The narrow ESW of aqueous electrolyte solutions brings a great deal of challenges to the enhancement of energy density. Not only it limits the output voltage narrowing the choice of active materials, but also inhibits the capacities.<sup>68,69</sup> Moreover, already limited capacities often decay at rapid rates due to the interface instability and side reactions.<sup>38</sup> Therefore, the inhibition of water splitting and prevention of interactions between free water and the surface of electrode is of great priority for creating high-power and stable batteries.

**Lack of alternative binder.** Well-performing ASIBs are a combination of comprehensive cell design, electrolyte chemistry, and precisely selected electrode composition.<sup>70</sup> A polymeric binder plays a crucial role in the preparation of high-performance electrodes.<sup>71</sup> Currently, most state-of-the-art ASIBs are processed using fluorine-containing polyvinylidene fluoride (PVDF).<sup>72</sup> Despite the undeniable advantages, poor hydrophilicity and adhesion to metal foil current collectors act as main motivation for the search of alternative binding materials. Moreover, this binder is associated with a number of safety and environmental red flags. The most concerning of which is the presence of highly toxic N-methyl-2-pyrrolidone (NMP) in electrode formulations.<sup>73</sup> Fluorinated carbohydrates, also called “forever chemicals” have been a target of ever-expanding regulations due to their persistence, bioaccumulation and potential health risks.<sup>74,75</sup>

**Limited selection of positive electrode materials.** In most materials the sites for sodium ion storage are finite, making it difficult to achieve great



specific capacities.<sup>66</sup> Moreover, using electrode materials with redox potential nearing the stability limit of aqueous electrolyte bears the risks of triggering oxygen evolution rather than reversible sodium insertion/deinsertion. Therefore, engineering of active materials with high capacities and suited redox potentials must remain in the focal field of researchers.

**Limited selection of negative electrode materials.** Sodium metal with its capacity of 1165 mAh g<sup>-1</sup>, the most convenient option for a negative SIB electrode, cannot be used in aqueous media for ASIBs.<sup>76</sup> Graphite, the most popular anode for LIBs, cannot be implemented in sodium counterparts due to the bigger radius of Na<sup>+</sup> and subsequent inefficient intercalation as well as highly unstable formed NaC<sub>x</sub> compounds.<sup>77</sup> Additionally, the voltage plateau of the reaction is well beyond the aqueous electrochemical stability window. The suitable materials require elaborate synthetic procedures and cannot offer high capacity. Moreover, as well as positive electrodes, they face dissolution and capacity fade related to parasitic reactions.<sup>78</sup>

## 2. EXPERIMENTAL METHODOLOGY

### 2.1. Active material synthesis

The majority of investigations presented in this thesis were carried out using **NaTi<sub>2</sub>(PO<sub>4</sub>)<sub>3</sub>** particles synthesised via conventional co-precipitation method as an active material. In a typical synthesis, 7.282 g of concentrated H<sub>3</sub>PO<sub>4</sub> (Reachem, 85 wt%) was poured into a beaker with 30 mL of water to reduce viscosity. 1.317 g of Na<sub>2</sub>CO<sub>3</sub> powder was added into H<sub>3</sub>PO<sub>4</sub> solution and left to react under continuous stirring to form Na<sub>2</sub>HPO<sub>4</sub>. Then, 14.112 g of Ti(OC<sub>4</sub>H<sub>9</sub>)<sub>4</sub> (Acros Organics, ≥98%) was added into isopropanol (20 mL) to prevent contact with air and agitated. Then it was immediately poured into the intermediate product Na<sub>2</sub>HPO<sub>4</sub> containing solution. The mixture was kept at room temperature to react completely for 30 min under constant stirring. In order to obtain the desired precursor, water and isopropanol were evaporated from the mixture on a hotplate. The resulting powder was ground and calcined in a muffle furnace at 700 °C in air atmosphere for 8 h. The obtained particles were reground and additionally ball-milled in a planetary ball-mill (Retsch PM400) for 1 h at 900 rpm in isopropanol with subsequent drying at 80 °C.

In investigations requiring positive electrodes following materials were used: Na<sub>3</sub>V<sub>2</sub>(PO<sub>4</sub>)<sub>3</sub> (NVP), Na<sub>2</sub>VTi(PO<sub>4</sub>)<sub>3</sub> (NVTP) and Na<sub>1.86</sub>Fe[Fe(CN)<sub>6</sub>] · 2.28H<sub>2</sub>O (NFCN).

**Na<sub>3</sub>V<sub>2</sub>(PO<sub>4</sub>)<sub>3</sub>** (NVP) samples were synthesized via solid-state method. In a typical synthesis, stoichiometric amounts of V<sub>2</sub>O<sub>5</sub> (Thermo Fisher, 99.2%), Na<sub>2</sub>CO<sub>3</sub> (Chempur, 99.8%), and NH<sub>4</sub>H<sub>2</sub>PO<sub>4</sub> (Honeywell, 99%) were mixed in 2-propanol and ball-milled (Retsch, PM400) at 350 rpm for 2 h. The mixture was then dried at 80 °C and the resulting powder was annealed in a tube furnace under the forming gas flow (5% H<sub>2</sub> + 95% N<sub>2</sub>) for 4 h at 400 °C and 8 h at 800 °C followed by regrinding after every annealing step. The final powder was obtained by milling in a planetary ball-mill at 350 rpm for 1 h.

For the synthesis of **Na<sub>2</sub>VTi(PO<sub>4</sub>)<sub>3</sub>** (NVTP), Na<sub>2</sub>CO<sub>3</sub> (Chempur, 99.8%), V<sub>2</sub>O<sub>5</sub> (Chempur, 99%), TiO<sub>2</sub> (Acros Organics, 98%), NH<sub>4</sub>H<sub>2</sub>PO<sub>4</sub> (Honeywell, >99%) were used. Na<sub>2</sub>VTi(PO<sub>4</sub>)<sub>3</sub> was synthesized by a conventional solid-state method. V<sub>2</sub>O<sub>3</sub> was prepared by heating V<sub>2</sub>O<sub>5</sub> in N<sub>2</sub>/H<sub>2</sub> (5% H<sub>2</sub>) atmosphere in three consecutive stages with intermediate regrinding: the first at 600 °C, the second at 900 °C, and the third at 1000 °C. Each stage lasted 8 h. Na<sub>2</sub>CO<sub>3</sub>, V<sub>2</sub>O<sub>3</sub>, TiO<sub>2</sub> and NH<sub>4</sub>H<sub>2</sub>PO<sub>4</sub> were mixed with isopropanol at the appropriate molar ratio and milled in a planetary ball-mill (Retsch PM400) at 450 rpm for 2 h. After ball-milling, the mixture was dried at 80 °C, fired at 400 °C for 4 h, reground, and finally calcined at 800 °C for

8 h in a tube furnace under a flowing N<sub>2</sub> atmosphere. The obtained particles were reground and additionally ball-milled for 1 h at 350 rpm in isopropanol with subsequent drying at 80 °C.

Monoclinic Na<sub>1.86</sub>Fe[Fe(CN)<sub>6</sub>] · 2.28H<sub>2</sub>O particles were synthesized via co-precipitation route. In a typical co-precipitation synthesis, Na<sub>4</sub>Fe(CN)<sub>6</sub> · 10H<sub>2</sub>O (Acros Organics, >98%) and L-ascorbic acid (C<sub>6</sub>H<sub>8</sub>O<sub>6</sub>) (Thermo Scientific, >99%) are dissolved in 200 mL of distilled water. The solution is bubbled with N<sub>2</sub> to remove O<sub>2</sub> for 24 h at 80 °C under constant stirring. The obtained light blue powder was washed several times by centrifugation with distilled water and ethanol, and subsequently dried at 80 °C overnight.

## 2.2. Materials characterization

**Powder X-ray diffraction** (XRD) was used to determine the phase composition of synthesised materials. The XRD patterns were recorded on a X-ray diffractometer (Bruker D2 Phaser) within the range  $10^{\circ} < 2\theta < 60^{\circ}$  using Ni-filtered Cu K<sub>α</sub> radiation. The scanning speed and step width were 1° min<sup>-1</sup> and 0.01°, respectively.

Morphological investigations of particles and electrodes were carried out using **Scanning electron microscopy** (SEM) (Hitachi TM-6000) and **Transmission electron microscopy** (TEM) (G2 F20 X-TWIN FEI). Samples for TEM analysis were prepared by coating <1 mg mL<sup>-1</sup> the dispersion of particles in 2-propanol on lacey carbon grid. ImageJ software<sup>79</sup> was used for carbon layer thickness determination.

The **Energy-dispersive x-ray spectroscopy** (EDX) analysis of the electrodes was performed using a table-top SEM (Hitachi TM-6000) equipped with an EDX detector.

The surface area was measured by a **Brunauer–Emmett–Teller** (BET) analyser (Anton Paar NOVA 600). Adsorption isotherms were obtained for the samples after outgassing them in vacuum at 120 °C for at least 3 h. The surface area was estimated by the Brunauer-Emmett-Teller model.

**Fourier-transform infrared** (FT-IR) **spectroscopy** was used to obtain information about functional groups of the material. The infrared spectra were obtained by FT-IR spectrometer (Frontier, Perkin-Elmer), equipped with Attenuated Total Reflectance (ATR) accessory. The measurements were performed in the 4000–450 cm<sup>-1</sup> range with 4 cm<sup>-1</sup> resolution.

The **Thermogravimetric analysis** (TGA) of the surface carbon and nitrogen content was carried out on a PerkinElmer STA6000 analyser in the

range of 30 to 700 °C and a heating rate of 10 °C min<sup>-1</sup> in flowing air atmosphere (20 mL min<sup>-1</sup>).

**X-ray photoelectron spectroscopy** (XPS) analyses were used to determine composition on the surface of the particles with Kratos AXIS Supra spectrometer using monochromatic Al-K<sub>α</sub> radiation (hν = 1486.7 eV) at 225 W X-ray gun power at 1 × 10<sup>-8</sup> torr pressure and room temperature.

The **elemental analysis** revealing carbon and nitrogen contents was performed by organic elemental analyser (Thermo Scientific Flash 200).

**Raman spectroscopy** was conducted using a Renishaw QONTOR instrument with a 532 nm laser. Each spectrum was recorded in the 2700 – 3900 cm<sup>-1</sup> range for 50 s (5 acquisitions × 10s) at 10% laser power.

**Nuclear magnetic resonance** (NMR) spectroscopy experiments were carried out on Bruker AVANCE III HD spectrometer operating at resonance frequencies of 400 and 162 MHz for <sup>1</sup>H and <sup>31</sup>P, respectively (magnetic field of 9.4 T). The concentrations of phosphates in electrolytes were estimated using 60 mM/L adenosine diphosphate (ADP) solution in H<sub>2</sub>O.

For the *in-situ* **pH monitoring**, a pH meter (Mettler Toledo SevenCompact s220) equipped with a combination pH probe (Mettler Toledo InLab Micro Pro-ISM) was used.

For the **conductivity measurements**, a pH meter (Mettler Toledo SevenCompact s220) equipped with conductivity sensor (Mettler Toledo InLab 741-ISM) was used.

### 2.3. Electrode preparation

The electrode slurry was typically prepared by mixing 70 wt% of active material, 20 wt% of carbon black (CB) (Super-P, TIMCAL) and 10 wt% of polyvinylidene fluoride (PVDF) (HSV1800, Kynar) in N-methyl-2-pyrrolidone (NMP) (Sigma Aldrich, 99.5%). Dry components were premixed in a high-energy ball-mill for 1 h at 175 rpm (Fig. 6). The slurry was then homogenised for 2 h at 350 rpm and subsequently casted as a film. After drying in vacuum for 3 h at 120 °C the resulting electrode film was punch-cut into 14 mm diameter disks and transferred onto 316L stainless steel mesh (#325) by hydraulic pressing.

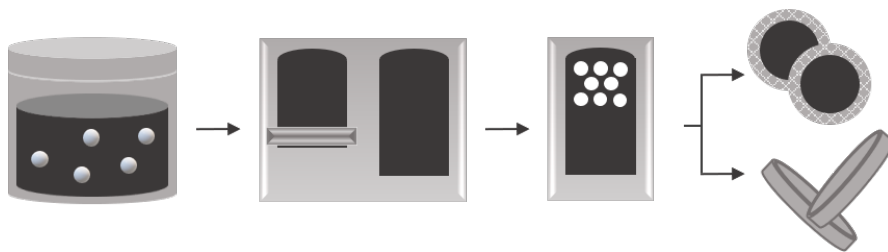


Figure 6. Electrode and coin-cell preparation process, including slurry mixing, casting, and electrode punching.

For the binder investigations, PVDF was replaced by other polymeric binders. In some cases, the amount of binder varied between 10-30%. Adhesive properties were investigated by casting the slurry directly onto the stainless-steel foil substrate.

For investigations in organic electrolytes, electrodes were prepared by dispersing active material, PVDF and CB in a respective weight ratio of 80%, 10%, 10% in appropriate amounts of NMP in Thinky mixer for 20 min at 6000 rpm. The resulting homogeneous slurry was casted on carbon-coated aluminium foil using doctor blade technique. After drying, electrodes with a diameter of 12 mm are punched and dried overnight at 80 °C under dynamic vacuum in a Büchi glass oven and later transferred inside the glovebox. CR 2032 coin half-cells (MTI Corp.) were assembled using the prepared electrodes, 150  $\mu$ l of electrolyte, and two 16 mm  $\varnothing$  separators (Whatman).

## 2.4. Electrochemical characterisation

**Cyclic voltammetry (CV)** was used to determine the redox processes, the potential at which they occur, and their reversibility. In this work, cyclic voltametric measurements were performed on a potentiostat-galvanostat (SP-240, Biologic and PGSTAT-302 Metrohm Autolab).

**Linear sweep voltammetry (LSV)** measurements were performed in order to determine gas evolution potential onsets using a potentiostat-galvanostat (Biologic SP-300).

**Self-discharge (SD)** measurements were performed using battery cycler (Neware CT-4008) by charging the electrode to a chosen potential and monitoring the open current potential in time.

The longevity of the electrodes was evaluated by **galvanostatic charge/discharge cycling (GCD)**. The change of voltage over time, capacity, and energy density is measured while a known current is applied to continuously charge and discharge the electrode between the chosen potential limits.

The total amount of charge consumed or produced by an electrochemical reaction is called **charge/discharge capacity** (Ah or Ah kg<sup>-1</sup> for specific capacity) and can be calculated from the applied current and total time.<sup>80</sup>

The **theoretical capacity** of a sodium aqueous battery refers to the maximum amount of charge it can store per unit and is calculated as follows:

$$Q_{\text{theoretical}} \text{ (mAh/g)} = \frac{n \times F}{M} \times \frac{1}{3.6}$$

where  $n$  is the number of moles of electrons transferred per mole of active material,  $F$  is Faraday's constant (96485,3 C mol<sup>-1</sup>),  $M$  is the molecular weight of the active material (g/mol). The factor  $\frac{1}{3.6}$  is used to convert from C mol<sup>-1</sup> to mAh g<sup>-1</sup>.<sup>81</sup>

**Coulombic efficiency (CE)** is a measure of how effectively a material can convert charge during its charge and discharge cycles. It's calculated as the ratio of the total charge extracted from the material to the total charge put into the material over a full cycle (%).<sup>82</sup>

The **C-rate** is a measure of the rate at which active material can be charged or discharged relative to its theoretical capacity. A 1C corresponds to completion of charge or discharge processes in 1 h.<sup>83</sup>

Galvanostatic charge-discharge cycling/self-discharge experiments were carried out on battery testers (MACCOR, Series 4000 and Neware CT-4008).

The electrochemical characterisation of half-cells was mostly performed in an three-electrode bottom-mount beaker-type cell (Fig. 7 b) or decoupled three-electrode bottom-mount beaker-type cell (Fig. 7 a) designed for flat samples in Na<sub>2</sub>SO<sub>4</sub> (aq.) (10 ml, 1 M) electrolyte solution.

In the latter setup the working NTP and graphite rod counter electrodes were placed in separated compartments connected by 1 M NaNO<sub>3</sub> agarose salt bridge. Hg/Hg<sub>2</sub>SO<sub>4</sub>/K<sub>2</sub>SO<sub>4</sub> (aq. sat) (MSE) was used as a reference electrode. The electrolytes were naturally aerated during the most experiments. The electrochemical characterisation of full cells was performed in CR 2032 coin cells (Fig. 7 c). Linear sweep voltammetry (LSV) measurements were performed in a three-electrode custom-made cell with a glassy carbon rotating disc electrode, carbon rod counter electrode and Hg/Hg<sub>2</sub>SO<sub>4</sub>/(1 M K<sub>2</sub>SO<sub>4</sub> (aq)) reference electrode (Fig. 7 d).

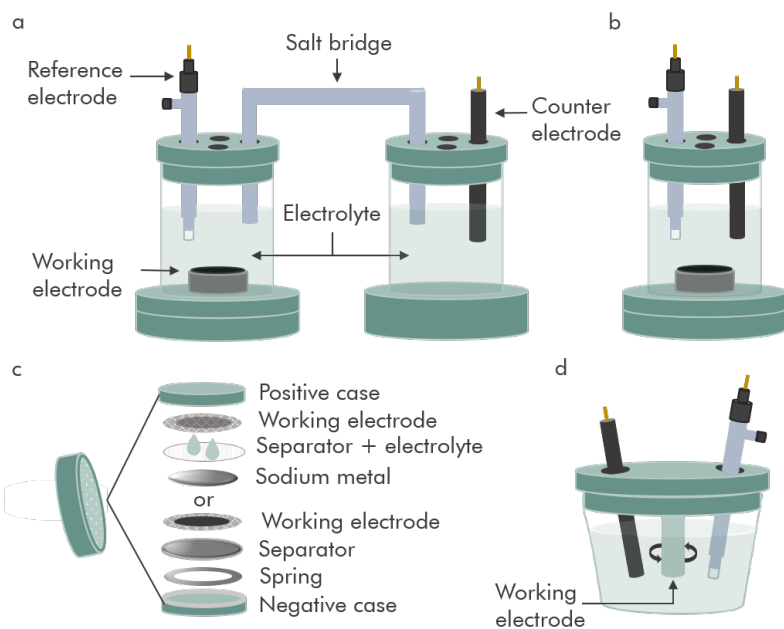


Figure 7. Schematic illustration of (a) decoupled three electrode cell, (b) three electrode cell, (c) coin cell, and (d) three electrode cell with rotating disc electrode.

### 3. RESULTS AND DISCUSSION

#### 3.1. Carbon in electrodes

The improvement of electronic conductivity in NTP as in other NASICON-structured materials is crucial for practical applications of this material in real electrochemical devices where high currents are needed.<sup>84</sup> The attempts aimed at enhancing the electronic conductivity are primarily focused on the particle size reduction, aliovalent doping and introduction of various conductive materials.<sup>85–87</sup> The latter method provides a unique external conducting network which ensures rapid electron migration in the electrode, resulting in superior reversibility and kinetics of electrode reactions.<sup>88</sup> It has been shown that low-cost and environmentally-friendly carbonaceous materials including porous carbon, carbon nanowires, carbon nanotubes, and graphene effectively diminish the interfacial resistance by forming extensive highly-conductive agglomerate structures that effectively frame the insulating active material particles.<sup>89,90</sup> Moreover, carbon layer on the surface of the particles has been reported to suppress some of the electrolyte-assisted side reactions by minimizing direct contact of active material and electrolyte, hence, acting as a protective layer.<sup>91–93</sup>

Although conductive carbons improve the overall conductivity and stability of the electrode, their content needs to be kept minimal not to compromise a practical mass loading of the active material. Also, carelessly chosen amount of carbon can result in inhibited ion diffusion rates.<sup>94</sup> Thus, electrode components and their ratios need careful consideration and optimisation. A sensible approach to creating uninterrupted pathway for electron transfer with as little carbon as possible would be introducing it during slurry preparation as well as forming a layer of carbon on the surface of the active material (Fig. 8).



Figure 8. Preferred carbon distribution in the composite electrode.



### 3.1.1. Carbon black

The role of carbon in the electrode is not limited to being the conductive additive. Carbon also helps to create a more uniform electrode structure, which aids in maintaining mechanical integrity during cycling, thereby extending the battery lifespan and reliability and also allows for faster charge and discharge rates.<sup>95,101,102</sup> Additionally, it prevents the loss of the contact upon the degradation of anode materials during cycling, ensuring stability.<sup>96,97</sup> Moreover, carbon helps in dissipating heat, which is vital for preventing overheating, which is of particular importance for batteries with organic electrolytes.<sup>98</sup>

Introducing carbon black – a low cost, safe, and reasonably stable carbon filler into the electrode composite has been a common manufacturing practice for virtually all electrochemical applications.<sup>99</sup> It has previously been mentioned that minimal amounts of auxiliary components are expected in the formulation not to compromise the energy density of electrode. However, for carbon black (CB), the optimum amount of conductive additive required to significantly enhance electrical conductivity through a well-connected "point to point" network is relatively high in comparison with other carbonaceous materials.<sup>100</sup> Different carbon nanotubes, nanofibers, and graphene derivatives could potentially lower the percolation threshold if used instead, however, their high prices make such replacement unfeasible for practical applications.<sup>101–103</sup> Simultaneously, while higher conductivity is achieved with higher carbon black contents, the maximum stress and Young's modulus are reported to be weakened, resulting in diminished flexibility and, potentially, shorter lifespan of the electrode itself.<sup>104–106</sup> This underlines the need for a careful and sensible approach to the slurry and electrode preparation.

Different NTP electrodes with three different carbon black (CB) contents were prepared and their electrochemical performance was evaluated by GCD cycling (Fig.9). The binder content was kept constant at 10%, and the amount of active material was adjusted depending on the carbon content (100% – 10% (binder) – x% (carbon)). As expected, the sample with lowest carbon black wt% delivered the lowest initial capacity and had the worst capacity retention upon cycling. The lower discharge capacity as well as inferior capacity retention can be explained by lower electrical conductivity, leading to inefficient electron transport and reduced battery performance.<sup>107</sup> Doubling of the CB wt% in the electrode composition contributed mainly to the increased capacity retention (from 27.7% to 59.9%) and slightly elevated initial discharge capacity (from 81.1 to 85.4 mAh/g). Further increase in conductive

additive wt% benefited the initial capacity (from 85.4 to 94.6 mAh/g) but improved the retention only slightly (from 59.9% to 62.5%).

Further increase of carbon wt% in the slurry composition does not seem feasible for practical applications. However, part of CB can be substituted by more conductive carbonaceous counterparts without drastically compromising the cost of production.

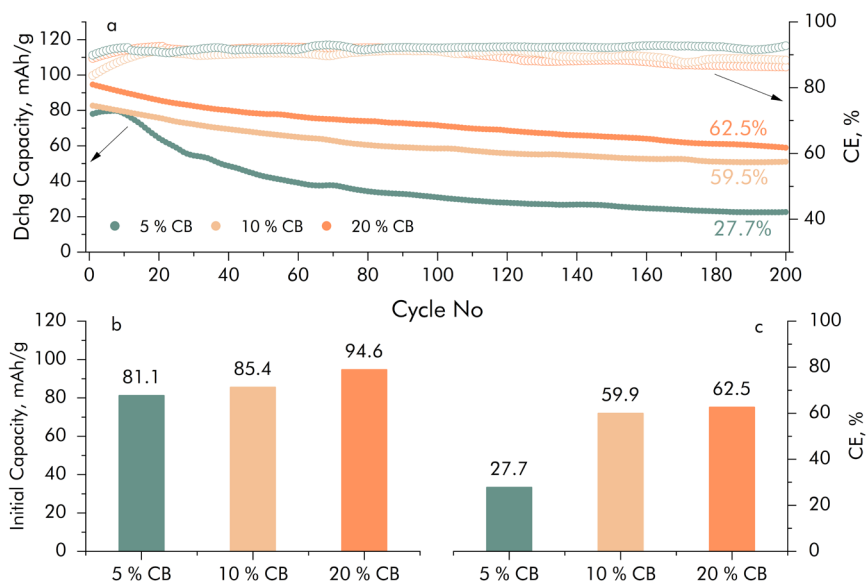


Figure 9. (a) GCD cycling performance, (b) initial capacities and (c) capacity retentions of NVP-based electrodes in naturally aerated 1 M  $\text{Na}_2\text{SO}_4$  (aq).

### 3.1.2. Particle carbon coating

#### Soluble carbonaceous compounds

Currently, there are several widely utilized approaches for forming carbon layers on ceramic materials. One is based on simple mechanical dispersion and mixing of powder with carbonaceous additive (Fig. 10 a).<sup>108</sup> While this method offers the least time-consuming procedure, most forms of carbonaceous materials are not easily dispersible or readily soluble in traditional solvents, thus, this approach is mostly reserved for the treatment of active materials with poor thermal stability. Another class of methods use the pyrolysis of carbon precursors introduced during the synthesis or after-treatment (Fig. 10 b).<sup>109</sup> During pyrolysis, the organic compounds break down

in the absence of oxygen, leaving behind a carbon residue. Additionally, by tailoring pyrolysis conditions one can optimize the properties of the resulting carbon.<sup>110</sup> The organic pyrolysis approach provides a controlled conversion of precursors into carbon layer typically resulting in better conductivities and charge capacities.<sup>111</sup> Consequently, as NTP is characterised by thermal stability allowing a high-temperature pyrolysis procedure, the latter method was chosen for this study.

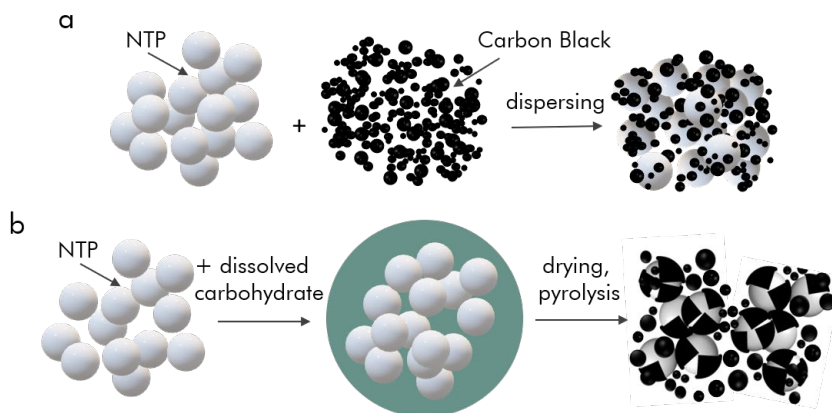


Figure 10. Schematic view of carbon-coated NTP particle preparation by (a) mechanical dispersion of carbonaceous additive; (b) soluble carbon-based compound encapsulation with subsequent pyrolysis.

The effect of two conventional carbon precursors – citric acid (CA) and glucose on the electrochemical performance of NTP was investigated. Two series of electrodes were prepared by homogeneously mixing NTP powder and citric acid/glucose in distilled water (50 mL). The amounts of carbon-based compounds were set to be 10, 15, 20, 30 wt% of total component weight (denoted by sample codes accordingly CA $x$  or GLU $x$ , where  $x$  represents the weight percentage of carbon precursor). The resulting mixture was heated at 60 °C under magnetic stirring, and subsequently dried at 70 °C for water elimination. The obtained white powder was reground and pyrolyzed at 700 °C for 2 h in a tube furnace under N<sub>2</sub> gas flow. The resulting powder was additionally ball-milled for 1 h at 350 rpm in isopropanol and subsequently dried at 70 °C in a drying oven.

Carbon content of as-prepared particles was determined by thermogravimetric analysis (TGA) and is presented in Fig. 11. The TGA curves show carbon content ranging from 1.74 wt% to 4.94 wt% for citric acid series (Fig. 11 a), and from 3.14 wt% to 10.24 wt% for glucose series (Fig. 11

b). Interestingly, analysis shows almost double the content of carbonaceous residue for glucose-coated samples (Fig. 11 c) despite similar carbon contents in initial compounds (40% and 37.5% for glucose and citric acid, respectively). As the final mass of a carbon is indicative of pyrolysis progress, it is safe to assume that breaking and rearranging of the chemical bonds requires higher pyrolysis temperatures when glucose is used as a precursor.<sup>112,113</sup>

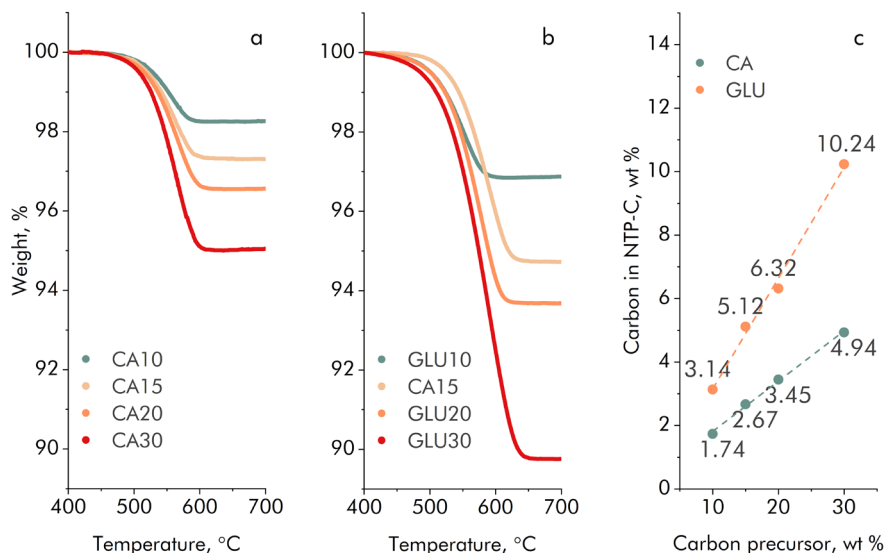


Figure 11. TGA determined final carbon wt% in (a) CA and (b) GLU series and (c) carbon content plotted as a function of precursor wt %.

In order to evaluate the electrochemical performance of these carbon-coated powders, electrodes were prepared following the procedure described in Electrode preparation section. Galvanostatic charge/discharge (GCD) cycling was performed in a beaker-type three electrode cell, and results are presented in Fig. 12. They show that, generally, higher amount of carbon resulted in improvement of charge-discharge cycling stability with no obvious effect on initial discharge capacities (Fig. 12 a-b). It seems that in both series there is a plateau reached at around 80% of capacity retention (Fig. 12 c) which is, notably, reached at quite different carbon contents (3.45 wt% and 6.32 wt% for citric acid and glucose, respectively). These findings suggest that citric acid yields a carbonaceous film providing better buffering layer for active material and facilitates less water-induced degradation and capacity loss.

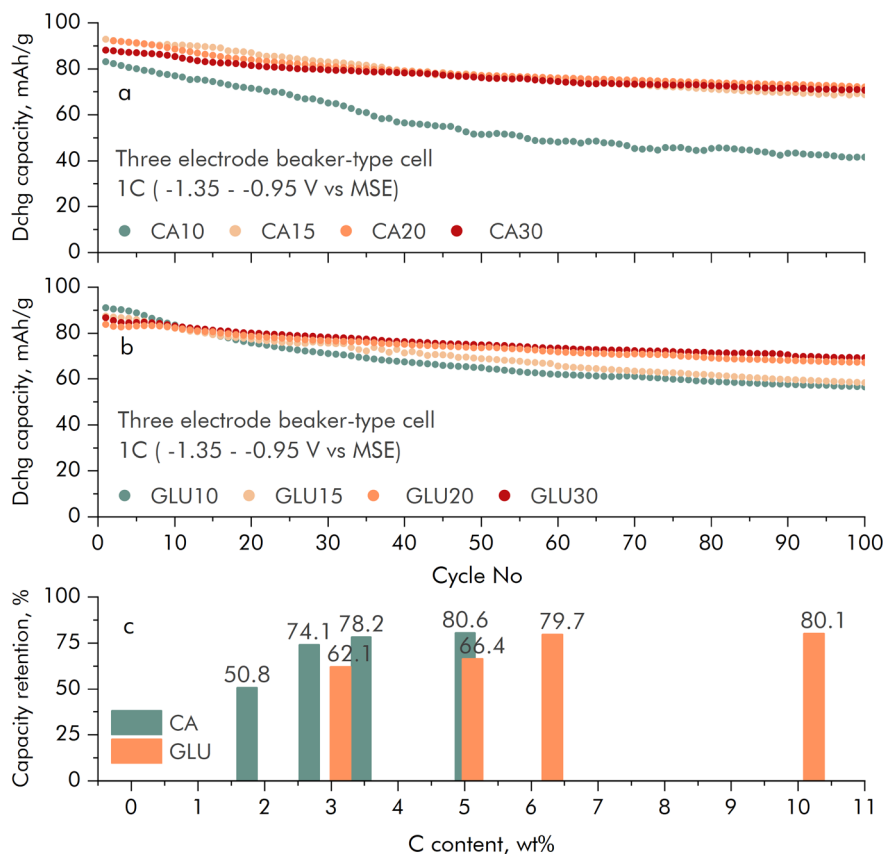


Figure 12. GCD cycling performance of NTP based electrodes with (a) CA, (b) GLU as a carbon precursor and (c) capacity retention as a function of carbon content.

### Polymer-derived coatings

Despite the evident simplicity of previously described coating approaches, suspending active material particles in carbohydrate solutions prior to pyrolysis does not typically yield uniform coatings because unquantified amount of carbon inevitably remains disconnected from the surface of active material.<sup>114,115</sup> Additional grinding and homogenization can slightly mitigate those irregularities; however, uneven coverage still remains a subject to be addressed. A coating method based on selective precursor adsorption and controlled shell growth by *in-situ* polymerization on the particle surface could be the key to manufacturing uniformly carbon-coated particles.<sup>116–118</sup>

Dopamine (DA) is a natural compound recognized for its remarkable adhesion properties, which stem from its multiple catechol and amine

functional groups.<sup>119</sup> These features enable DA to adhere effectively to a wide range of substrates, making it a versatile material for various applications. The self-polymerization of DA in a weakly basic medium, particularly under aerobic conditions, leads to the formation of a uniform and densely packed polydopamine (PDA) film.<sup>120</sup> The subsequent pyrolysis of PDA results in graphitization of the polymerized shell yielding a thin and uniform carbon layer on the surface of a particle (Fig. 13).<sup>121</sup> In this section we study resultant carbon coating which serves as both a protective barrier and an conductive medium, facilitating the transport of ions and electrons while protecting the material from the environment.<sup>114,122,123</sup>

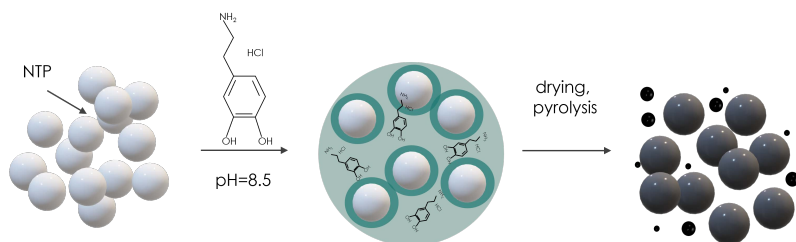


Figure 13. Schematic view of carbon-coated NTP particle preparation by PDA encapsulation approach.

For this study pre-synthesized NTP particles were carbon coated by homogeneously mixing NTP powder and citric acid in distilled water (50 mL). The amount of citric acid was set to be 10, 25, 40, 100, 150 wt% of active material weight (denoted by sample codes CA1, CA2, CA3, CA4, and CA5, respectively). The bulk of water was evaporated at 60 °C under magnetic stirring, and water elimination was completed at 70 °C in drying oven. The obtained powder was reground and pyrolyzed at 700 °C for 2 h in a tube furnace under constant N<sub>2</sub> gas flow. The resulting dark powder was additionally ball-milled for 1 h at 350 rpm in isopropanol and subsequently dried at 70 °C in a drying oven.

The polydopamine coating of the NTP particles was carried out through an *in-situ* polymerization. First, a series of tris(hydroxymethyl)aminomethane (TRIS) and HCl buffers were prepared for keeping the ratio (1:6) between DA and TRIS constant. In this procedure 0.9 g of as-prepared NTP was dispersed in TRIS-HCl (pH = 8.5, 30 ml) buffer solution. Then, dopamine hydrochloride was added in the amount of 5, 10, 30, 60, 100 wt% of active material weight (denoted as samples PDA1, PDA2, PDA3, PDA4, and PDA5, respectively). The mixture was vigorously stirred at room temperature between 16 and 70 h, and then centrifuged at 7000 rpm for 10 min in order to isolate the precipitate. The collected precipitate was washed with deionized water three times and

dried in a drying oven at 70 °C. The obtained brownish powder was reground and pyrolyzed at 700 °C for 2 h in a tube furnace under constant N<sub>2</sub> gas flow. The resulting particles were ball-milled for 1 h at 350 rpm in isopropanol and subsequently dried at 70 °C.

First of all, XRD analysis confirmed the structure and phase composition of samples. The patterns of pure NTP, PDA5\*, CA5\*, PDA5, and CA5 shown in Fig. 14 indicate that neither coating nor pyrolysis procedures had affected the composition and crystallinity of the bulk NTP. There is a good agreement between diffraction peaks of all samples and the standard PDF card. The recorded patterns identified highly crystalline NASICON-type structure with  $R\bar{3}c$  (No. 167) space group. The investigation clarified that even in high carbon content samples such as PDA5 and CA5, no extra carbon peaks are observed. This further proves that surface carbon is mostly of amorphous nature and does not affect the NTP structure and composition.

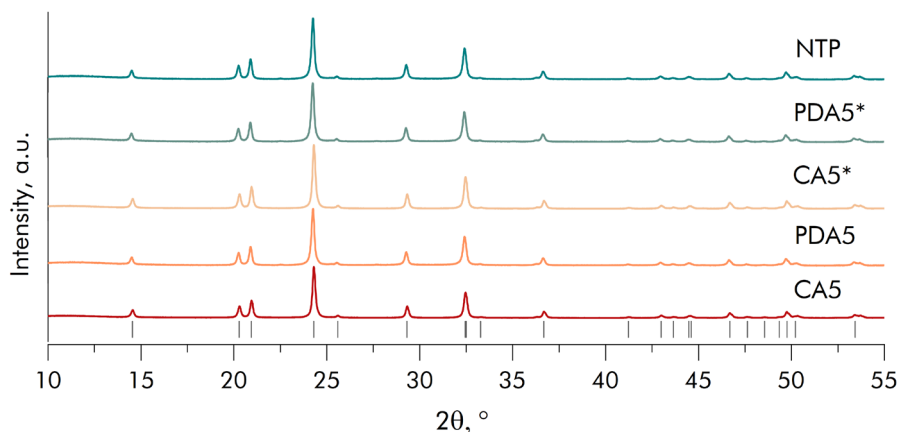


Figure 14. Powder XRD patterns of pure and carbon-coated NTP.

Secondly, the successful completion of self-polymerization reaction (Fig. 15) has to be confirmed.

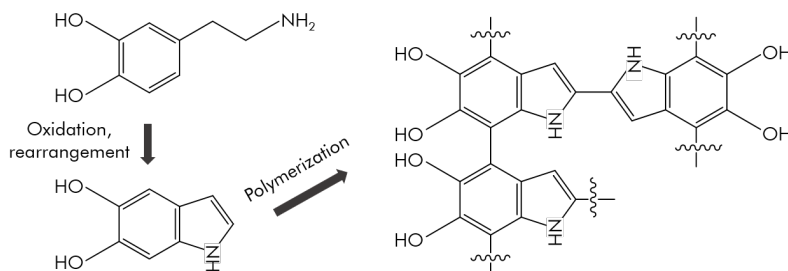


Figure 15. Representation of mechanism of dopamine self-polymerization.

The particle surface of pure NTP, PDA-coated and pyrolyzed samples was first characterized by FTIR spectroscopy (Fig. 16). The recorded bands in the 500 - 1500  $\text{cm}^{-1}$  region (Fig. 16 a) represent characteristic vibrations of P-O bonds in  $\text{PO}_4$  tetrahedra (574 and 1015  $\text{cm}^{-1}$ ) and of Ti-O bonds in  $\text{TiO}_6$  octahedra (642 and 983  $\text{cm}^{-1}$ ).<sup>124-126</sup> No clear difference between the three samples is noticed in this region of acquired spectra. The characteristic bands related to PDA lie mostly in the 1400 - 1650  $\text{cm}^{-1}$  spectral range (Fig. 16 b). In the spectrum recorded for PDA5\* (coated, but not pyrolyzed) the broad feature at 1615  $\text{cm}^{-1}$  is associated with either N-H bending or asymmetric C=C stretching characteristic for indole derivatives.<sup>127</sup> The pronounced band at 1486  $\text{cm}^{-1}$  is associated with CH bending vibrations.<sup>128,129</sup> The spectrum of a pyrolyzed PDA5 sample shows only one distinguishable band at 1558  $\text{cm}^{-1}$  (C=C stretching) confirming that PDA was successfully pyrolyzed.

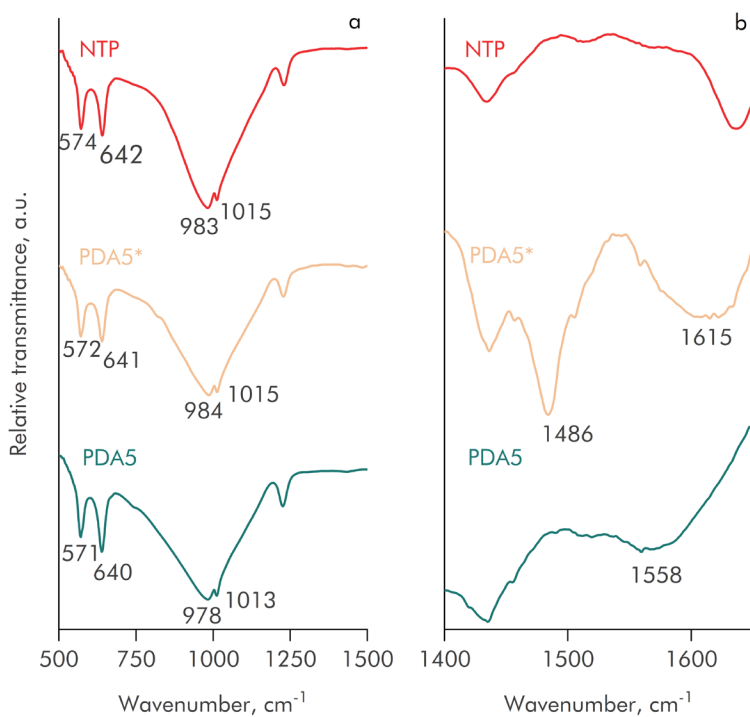


Figure 16. FTIR spectra of pure NTP, PDA5\* and PDA5 samples in the spectral range (a) 500 - 1500  $\text{cm}^{-1}$  and (b) 1400 - 1650  $\text{cm}^{-1}$ .

The broad band observed at 1558  $\text{cm}^{-1}$  most probably contains contribution from C=N bonds suggesting that carbon may exhibit enhanced nitrogen doping. N-doped carbonaceous phases were shown to enhance catalytic activity and electronic conductivity.<sup>130,131</sup> To precisely determine



nitrogen content in these composites, combustion elemental analysis was conducted. As summarized in Fig. 17, the analysis, indeed, confirms the presence of an N-containing carbon phase in these samples. The calculated carbon-to-nitrogen (C/N) ratio across the series remains around 15, indicating stable composition in the PDA-derived carbon coatings. The PDA1 sample, with 5 wt% PDA coating, was near the nitrogen detection limit, potentially introducing higher measurement error, hence is not present in Fig. 17.

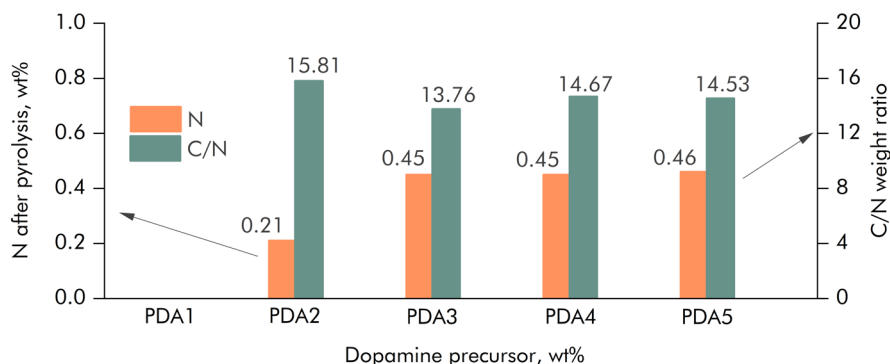


Figure 17. The nitrogen content and calculated C/N weight ratio for PDA sample series as determined by combustion elemental analysis.

Fig. 18 demonstrates that the carbon loading achieved via the PDA route differs significantly from that of the CA route. For the conventional CA approach, the carbon content of NTP samples is linearly dependent on the precursor concentration before pyrolysis. However, in the case of PDA linear dependence is observed only at low precursor concentrations, followed by a plateau that begins at around 20 wt% precursor concentration. This indicates that a final carbon loading of approximately 6.5 wt% is reached, regardless of DA concentration prior to polymerization. This indicates that a final carbon loading of approximately 6.5 wt% is reached, regardless of DA concentration prior to polymerization.

Another set of identical samples was prepared with an extended polymerization time (70 h). A dotted line in Fig. 18 shows that the general trend persists – a linear dependence at low DA concentrations followed by a plateau – but with a higher final carbon loading. A more than four-fold increased reaction duration resulted in approximately double final carbon loading. This suggests that, in the presence of surplus DA monomer, the reaction steadily proceeds at a slow rate and is limited by slow reaction kinetics. As the unreacted monomer could be easily eliminated by repeated washing, this careful optimization approach, in principle, allows for highly controllable and reproducible carbon loading in NTP and similar materials.

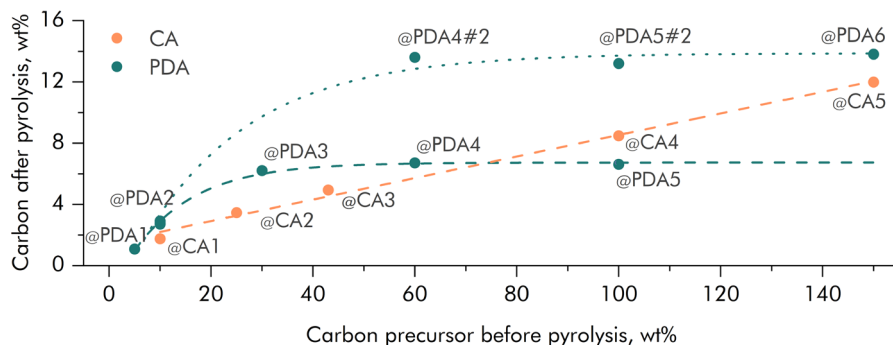


Figure 18. TGA determined carbon content in CA and PDA series.

The results of BET surface area investigation of NTP-carbon composites, presented in Fig. 19, suggest a linear relationship between the measured specific surface area and the carbon content. While the overall trends are similar, there are slight but consistent differences. The CA-coated series shows more variability in values, whereas the PDA series demonstrates a highly consistent dependence, suggesting better reproducibility. Additionally, samples produced via the PDA method systematically exhibit higher specific surface areas, which may influence their electrochemical properties.

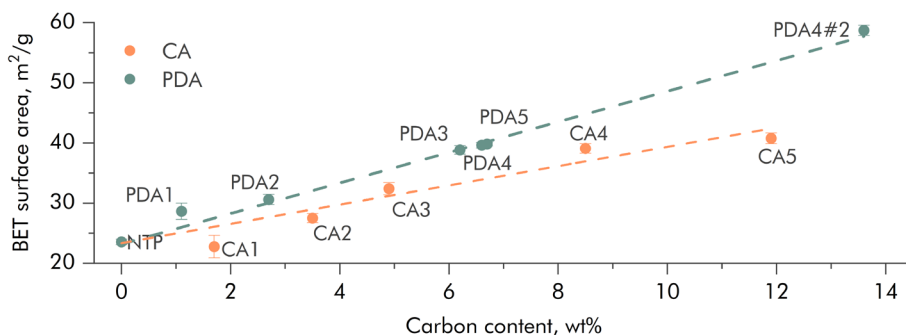


Figure 19. BET determined specific surface area dependence on final carbon content.

TEM imaging was conducted to additionally study uniformity of carbon layers on NTP particles (Fig. 20). TEM images of PDA series before (\*) and after pyrolysis confirms the presence of both highly crystalline NTP phase and a 3.5 – 4.7 nm wide amorphous polymeric layer for coated samples and 2.9 – 4.1 nm wide carbonaceous phase for the samples after pyrolysis. In both cases, phase distributed evenly on the surface of material resulting in core-shell structure with some decrease in the thickness of layer upon pyrolysis.

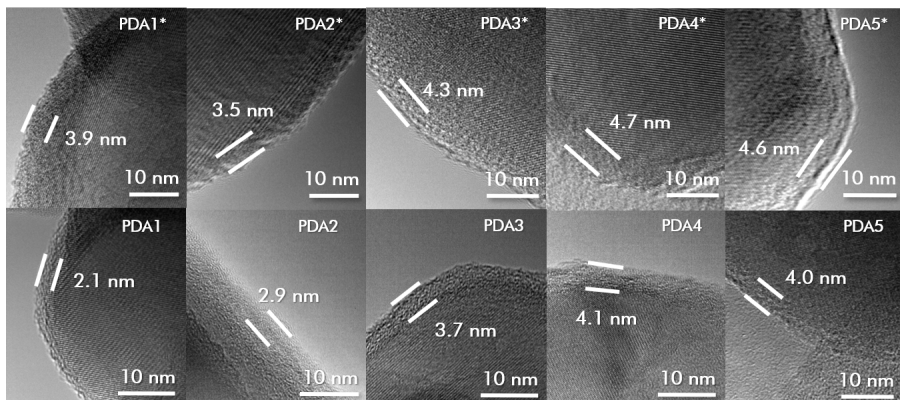


Figure 20. TEM images of PDA series before and after pyrolysis.

Subsequent examination of citric acid derived sample revealed not only significantly lower regularity of carbon layer (Fig. 21 a), but also the presence of additional phase (Fig. 21 b-d) at lower magnifications. The lacey structures are believed to be loose interparticular carbon flakes. Images of the samples prepared by polymerization indicated no presence of occasional chunks of carbon - a side product from pyrolysis process (Fig. 21 f-h).

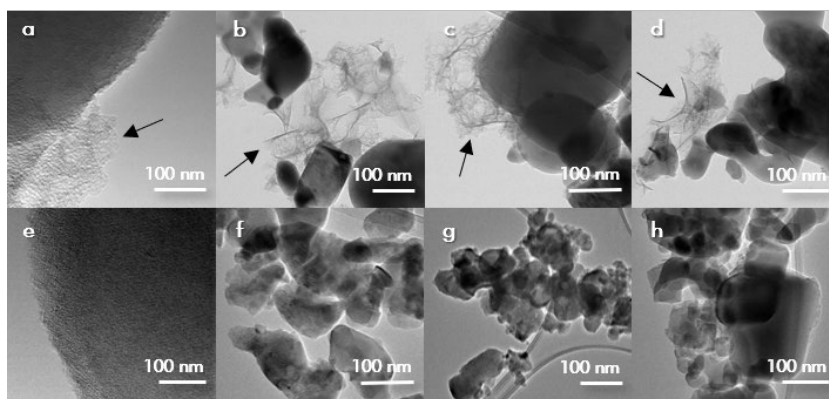


Figure 21. TEM images of CA3 (a-d) and PDA3 (e-h) samples.

For better understanding of the chemical differences at the surface of the material, XPS quantitative analysis was performed on two samples from both series with carbon content of 4.92 wt% (CA) and 4.31wt % (PDA). Fig. 22 presents summarised surface atomic compositions based on XPS analysis. Despite TGA revealing consistently lower carbon loading for PDA derived samples, surface investigation indicates slightly higher C/Ti ratio (Fig. 22 a). This result suggests presence of a more uniform carbon distribution on NTP

particles. Another interesting observation provided by XPS analysis is that the ratios of elements in PDA-coated samples are closer to those stoichiometrically expected. This is indicative of more crystalline, hence, closer to the nominal NTP composition at the surface of the coated samples.

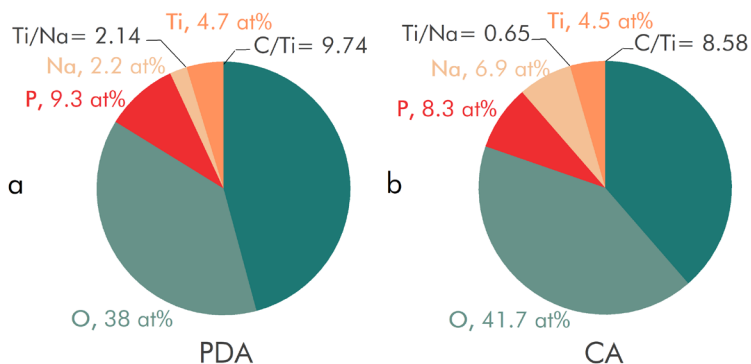


Figure 22. XPS analysed surface atomic composition of (a) PDA- and (b) CA-coated samples.

The electrochemical performance of NTP-based electrodes prepared from coated particles were studied by GCD cycling. The obtained data on initial capacities and cycling stability clearly demonstrate the consistent superiority of the PDA samples over the CA samples (Fig. 23). PDA-derived composites (Fig. 23 b) exhibit initial discharge capacities between 98-111 mAh/g, whereas CA-derived (Fig. 23 a) composites deliver around 90-95 mAh/g. This is, likely, due to enhanced electronic conductivity from a more uniform, N-rich carbon coating. In the same series a clear increase in capacity values from PDA1 to PDA3 is observed, indicating that greater carbon loadings improved the performance of electrodes. Conversely, in the CA-coated series, the carbon content has minimal impact on the initial capacity. However, after 200 cycles, the difference in capacity retention between the series is notably pronounced, with both sample series showing improved capacity retention as carbon content increases overall (Fig. 23 c). The best retention of 38% after 200 cycles is observed for the highest carbon content samples in both series.

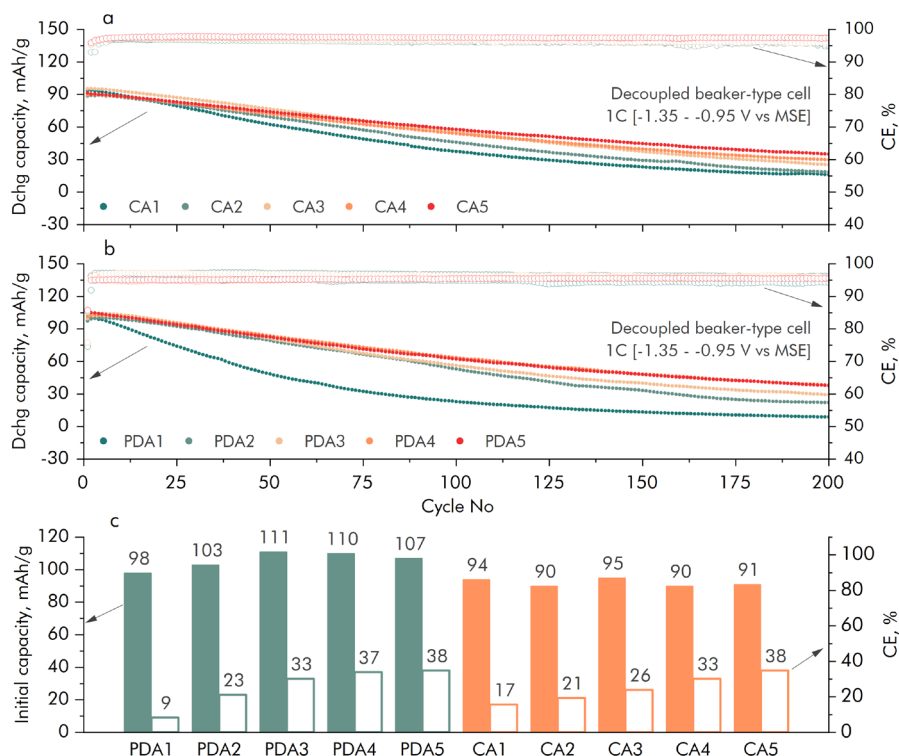


Figure 23. GCD cycling performance of (a) PDA1-5 and (b) CA1-5 electrodes, (c) their initial capacities and capacity retentions in naturally aerated 1 M Na<sub>2</sub>SO<sub>4</sub> (aq).

Notably, the carbon loadings responsible for such retention are extremely different (Fig. 24): 6.7 and 11.9 wt% for PDA5 and CA5 samples, respectively. Oxygen-assisted self-discharge is known for being the main cause for the local pH increase and subsequent degradation and dissolution of active material into the electrolyte.<sup>132,133</sup> More integral and uniform carbon layer in core-shell composite in PDA-derived samples offers more feasible protection from O<sub>2</sub> attack which is occurring in naturally aerated electrolytes.

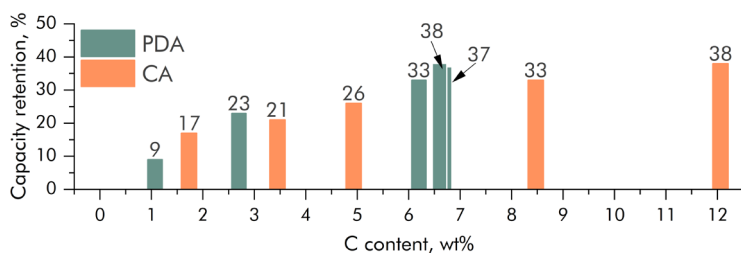


Figure 24. Capacity retention as a function of carbon content for CAx and PDAx series.

The enhancement in cycling stability with higher carbon loading might be due to the formation of an aqueous interphasial layer similar to the solid-electrolyte interphase in organic electrolytes.<sup>132,134</sup> This layer consisting of insoluble titanium-rich degradation products is reported to grow at the aqueous/NTP interface and is capable of slowing down, but not entirely preventing the degradation of active material. The growth of the said layer during GCD cycling is substantially more pronounced in the composites with higher carbon loading.<sup>124</sup>

The investigation of PDA coated NASICON-structured material  $\text{Na}_3\text{V}_2(\text{PO}_4)_3$  (Fig. 25) further supports this theory. Despite great performance in common organic electrolytes, this material is renowned for instant dissolution into the aqueous electrolytes.<sup>135,136</sup>

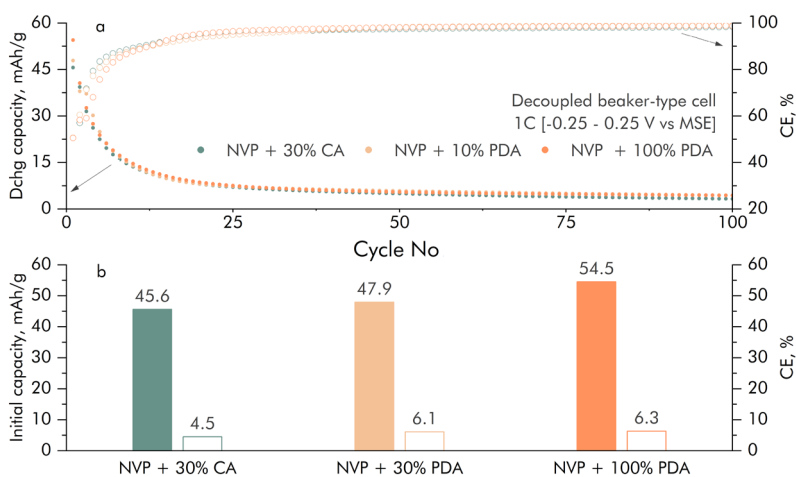


Figure 25. (a) GCD performance, (b) initial capacities and capacity retentions of NVP-based electrodes in naturally aerated 1 M  $\text{Na}_2\text{SO}_4$  (aq).

Differently from water-assisted NTP degradation, carbon coating does not improve cycling stability of the NVP active material. It is evident from Fig. 25, which contains the results of GCD cycling for NVP-based electrodes, that rapid capacity degradation occurs regardless of the carbon source and loading. Fig. 25 b reveals very similar capacity retention values; however, initial capacities suggest that similarly as in the NTP investigation, PDA-derived carbon shell had a favourable effect on the initial capacities. These findings suggest that rather than acting as a protective layer preventing material and electrolyte contact, carbon coating provides a favourable media for such layer to form.

### 3.1.3. Electrode preparation

In battery slurries, carbon black forms micron-scale clusters, known as agglomerates, whose size and distribution depend on the slurry formulation and the details of the coating process.<sup>137</sup> The distribution of the carbon affects the utilization of the active material in the electrode. The process of electrode preparation in experimental section is a result of an investigation presented here. In this section the electrodes prepared by different preparational procedures are studied.

Tap density of an electrode composite is indicative of homogeneity of microstructure and optimized composition of an electrode. In industry, the as-prepared electrodes undergo calendaring in order to improve the adhesion and increase the tap density. Studies show that as electrode density increases, the cycling stability is increased until a certain threshold.<sup>138</sup> This is demonstrated by the study of the effect of the calendaring on electrochemical performance (Fig. 26). Electrodes, transferred onto mesh of size 200, show increasing cycling stability as the transfer pressure increases (from 35.5% to 40.1% to 44.2%). Initial capacity has a slight upward tendency (from 82.55 mAh/g to 85.98 mAh/g to 87.65 mAh/g).

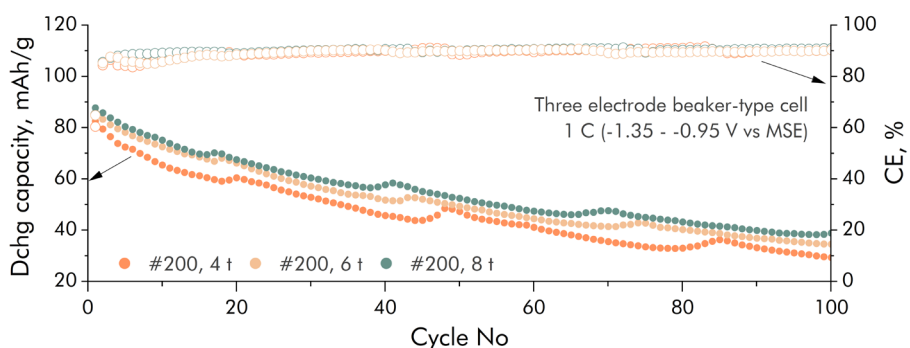


Figure 26. GCD cycling performance of NTP-based electrodes transferred onto mesh No. 200 with 4/6/8 tons weight in 1 M Na<sub>2</sub>SO<sub>4</sub> (aq).

However, electrochemical performance also depends on the properties of the current collector. Fig. 27 shows GCD cycling data for the electrodes on stainless steel mesh of different sizes with minimal pressure applied required for a successful transfer. As expected, capacity retention increases from 4 t to 6 t (from 35.5% to 58.9%) and remains stable. Samples, pressed with more than 6 t exhibited resistance to aluminium foil delamination, which elevates the risk of introducing bits off foil into aqueous media as well as incorrectly determining mass loading of the electrode. Interestingly, sample pressed onto

mesh №80 exhibits diminished stability of 24.4%, despite similar initial capacity. It might be that mesh is not fine enough to simultaneously distribute charged species to all points of electrode, resulting in inferior performance.

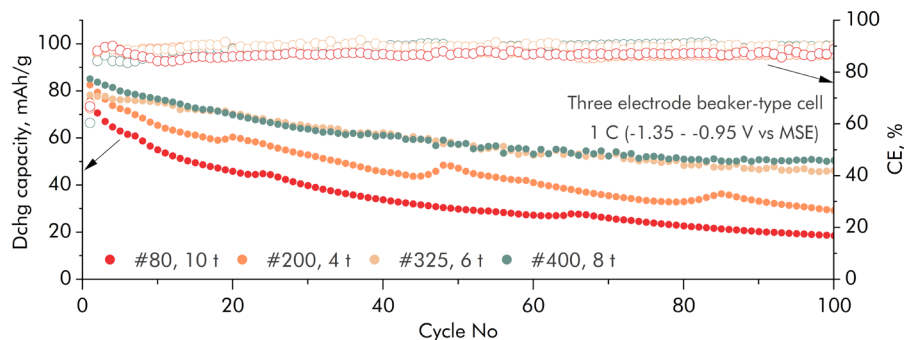


Figure 27. GCD cycling performance of NTP-based electrodes transferred onto different meshes with minimal weight in 1 M  $\text{Na}_2\text{SO}_4$  (aq).

In this investigation, the dependence of uniformity on ball-milling is studied. Fig. 28 shows scanning electron microscopy (SEM) images of electrodes prepared by mixing active material, carbon additive, polymeric binder, and solvent (5x times of AM wt.%) for 30-180 minutes with ceramic 5 mm beads in a planetary ball-mill. It can be seen that the mechanical treatment clearly reduces the particle size of the composite. It is expected for the slurry to initially have some distribution in size of material as the co-precipitation synthesis does not guarantee monodispersity. The quantity of agglomerates, however, varies dramatically throughout the ball-milling. At 30 min of mixing (Fig. 28 a) the slurry is full of large particles of the electrode components whilst after 3 h of mixing (Fig. 28 d) there are nearly no noticeable big chunks of neither carbon or active material.

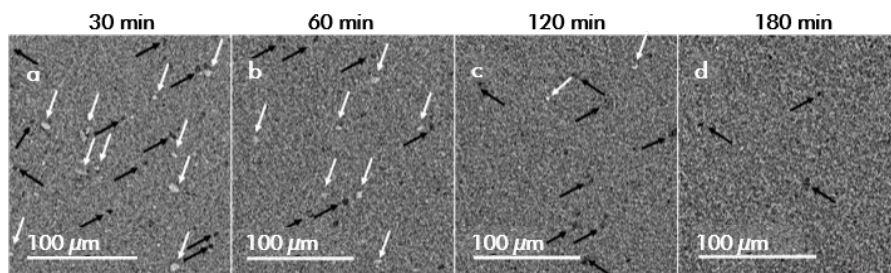


Figure 28. SEM x100k images of electrodes prepared by (a) 30, (b) 60, (c) 120, and (d) 180 min ball-milling of AM + CA + PVDF + NMP.



Tap densities of electrodes were calculated from mass loading and thickness of the electrodes (15 electrodes of each batch analysed) are presented in Table 1. Increased density signifies that particles are better distributed and closely packed ensuring better pathways for mass transport.

**Table 1.** Tap densities of electrodes prepared by varying the mixing time.

Pre-mixing	-	-	-	-
Mixing	30 min ball-milling	60 min ball-milling	120 min ball-milling	180 min ball- milling
Tap density	$0.60 \pm 0.01$ g/cm <sup>3</sup>	$0.61 \pm 0.02$ g/cm <sup>3</sup>	$0.65 \pm 0.01$ g/cm <sup>3</sup>	$0.65 \pm 0.01$ g/cm <sup>3</sup>

Effective de-agglomeration at the lab-scale is achieved by prolonged ball-milling times, which is less technologically convenient and energy efficient. It is common, that manufacturing process requires knowing a few “tricks” as well as investing additional equipment such as pre-mixers.<sup>139</sup> It has been known for a while that pre-treating the active material by ball-milling reduces the particle size, enhances the capacity and the rate capabilities of the cell due to the improved contact between electrode components.<sup>140</sup> However, dry mixing of powdery constituents of the electrode – a critical process step – is often overlooked. The inclusion of pre-mixing without liquid components is a normal manufacturing practice, that results in alterations of electrode properties.<sup>141</sup>

In this part of investigation, active material was premixed for 1 h with carbon prior to the addition of polymeric binder and solvent. Pre-mixing was conducted using 2 mm/3 mm/5 mm ceramic beads at 250 rpm in the planetary ball-mill. Uniformity of active materials was studied through scanning electron microscopy (SEM). SEM images of electrodes prepared by premixing with 2 mm (Fig. 29 a-d), 3mm (Fig. 29 e-h) and 5 mm ceramic beads (Fig. 29 i-l) indicate that pre-mixing step resulted in decreased size of agglomerates and their quantity in the electrode compared to not pre-treated samples in Fig. 28. Even samples with the shortest mixing time show increased homogeneity after premixing is introduced (Fig. 29 a,e,i). Mostly, 120 min of mixing produce uniform electrodes (Fig. 29 c,g,k). Pre-mixing seems to affect carbon dispersion more than active material particles.

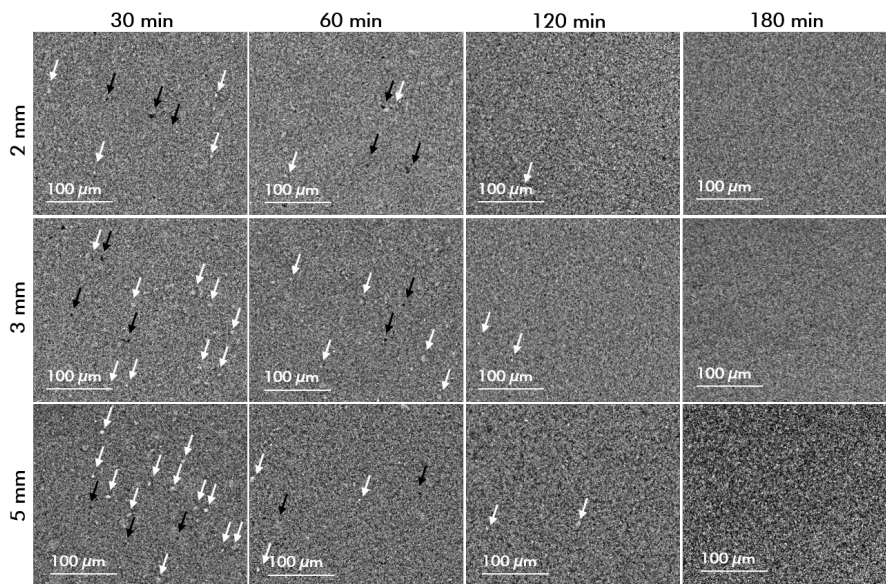


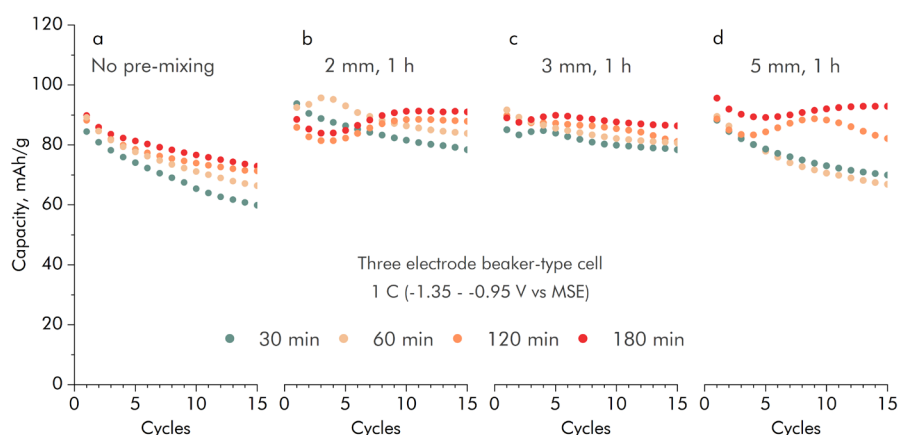
Figure 29. SEM x100k images of electrodes prepared by premixing AM+CA for 1 hour with (a-d) 2 mm beads (e-h) 3 mm beads (i-l) 5 mm beads followed by mixing with PVDF and NMP for 30/60/120/180 minutes.

The calculated density values correlate with SEM images (Table 2). It is evident, that the tap density was affected by introducing pre-milling of solid components. Even after short mixing of 30 min the tap density of electrodes on average increased by 41% ( $0.60 \rightarrow 0.846 \text{ g/cm}^3$ ). The density, as well as homogeneity, reached their maximum at about 2 h of mixing. The electrodes with the highest density and good reproducibility in thickness were obtained through premixing carbon and active material with 3 mm beads for 1 h followed by 2 h of ball milling with solvent and binder. Higher density can be attributed to the effective dispersion of carbon network as well as milling occurring simultaneously with the mixing of the inorganic active material.

**Table 2.** Tap densities of electrodes dependency on preparation procedure.

Pre-mixing	2 mm, 60 min			
Mixing	30 min ball-milling	60 min ball-milling	120 min ball-milling	180 min ball-milling
Tap density	$0.87 \pm 0.07$ g/cm <sup>3</sup>	$0.90 \pm 0.04$ g/cm <sup>3</sup>	$0.94 \pm 0.12$ g/cm <sup>3</sup>	$0.90 \pm 0.05$ g/cm <sup>3</sup>
Pre-mixing	3 mm, 60 min			
Mixing	30 min ball-milling	60 min ball-milling	120 min ball-milling	180 min ball-milling
Tap density	$0.88 \pm 0.03$ g/cm <sup>3</sup>	$0.91 \pm 0.02$ g/cm <sup>3</sup>	$0.96 \pm 0.06$ g/cm <sup>3</sup>	$0.98 \pm 0.13$ g/cm <sup>3</sup>
Pre-mixing	5 mm, 60 min			
Mixing	30 min ball-milling	60 min ball-milling	120 min ball-milling	180 min ball-milling
Tap density	$0.79 \pm 0.06$ g/cm <sup>3</sup>	$0.82 \pm 0.09$ g/cm <sup>3</sup>	$0.85 \pm 0.02$ g/cm <sup>3</sup>	$0.85 \pm 0.04$ g/cm <sup>3</sup>

Electrochemical investigation in standard aqueous setup is performed after mechanical calendaring, thus, is less informative regarding effect of initial density than it would be if measurements were carried out without pre-mixing step. However, due to their poor adhesion to metal surfaces in aqueous media, polymeric binders lose contact with the metal-based current collectors and compromise the electrode. Nonetheless, the GCD cycling study revealed there is no detrimental effect of two-step mixing or longer mixing on the electrodes as well as slightly better cycling stability after short cycling (Fig. 30).

**Figure 30.** GCD cycling of NTP-based electrodes prepared by (a) non-, (b) 2 mm 1h, (c) 3 mm 1h, and (d) 5 mm 1 h premixing in 1M Na<sub>2</sub>SO<sub>4</sub> (aq).

### 3.1.4. Summary

In this part of the work, the preparation processes for composite  $\text{NaTi}_2(\text{PO}_4)_3$  electrodes to be used in aqueous sodium-ion battery cells is studied in detail. The obtained results are summarized as:

- The particles of  $\text{NaTi}_2(\text{PO}_4)_3$  active material are carbon coated by pyrolysis of citric acid and glucose. The particles coated with citric acid pyrolysis show better capacity retention at lower carbon loading than those coated by glucose pyrolysis. This could be related to different pyrolyzation and graphitization temperatures of these compounds.
- The particles of  $\text{NaTi}_2(\text{PO}_4)_3$  active material are carbon coated by pyrolysis of surface polymerized polydopamine. The resulting carbon coating is significantly more uniform, controllable and reproducible. The required carbon loading to ensure the same capacity retention is only half of that as in the case of citric acid pyrolysis.
- The optimal amount of conductive carbon black additive in the composite  $\text{NaTi}_2(\text{PO}_4)_3$  electrodes is determined to be 20 wt%. The increasing content of carbon black from 5 wt% to 20 wt% results in better initial capacity and capacity retention from 27.7% to 62.5%. The further increase of carbon black filler is not feasible for practical applications.
- The mechanical pressing of the electrodes during the transfer onto stainless steel mesh results in higher tap density and lower porosity. The optimal electrochemical properties in terms of initial capacities and retentions during cycling are achieved by pressing with 6 t.
- The duration of slurry mixing during electrode preparation shows significant effects on carbon dispersion and electrode tap density. The introduction of an additional step of dry component pre-mixing results in even better electrode tap density and uniformity. 1 h of dry premixing and 2 h of slurry mixing results in optimal carbon conductive network inside of the electrode.

These results form the basis of electrode preparation and formation procedures for the rest of this work.

### 3.2. Electrolyte solutions for aqueous batteries

Over the past few decades, organic electrolytes have proven to be highly versatile in various applications.<sup>142</sup> Their unique properties, such as electrolytic stability and compatibility with a wide range of electrode materials, have made them indispensable in fields like lithium-ion batteries, supercapacitors, and redox-flow batteries.<sup>143,144</sup> Organic electrolytes offer a wide electrochemical window, enhancing the energy density and cycle life of these devices.<sup>19</sup> Moreover, their tunable physicochemical properties allow for the optimization of electrochemical performance in energy storage devices.

Currently, significant efforts are being made to replace organic electrolytes, known for their hazards such as explosions, fires, and harmful leaks, with their aqueous counterparts.<sup>145,146</sup> Water-based electrolytes offer superior thermal stability, environmental friendliness, and high ionic conductivity ( $\sim 10^{-1} \Omega^{-1} \text{ cm}^{-1}$ ) compared to organic ( $10^{-3}$ – $10^{-2} \Omega^{-1} \text{ cm}^{-1}$ ), polymeric ( $10^{-7}$ – $10^{-3} \Omega^{-1} \text{ cm}^{-1}$ ), and solid inorganic ( $10^{-7}$ – $10^{-2} \Omega^{-1} \text{ cm}^{-1}$ ) electrolytes.<sup>147</sup> The hydrogen bond network in water facilitates fast ion diffusion to the surface of electrodes containing redox species. However, low electrochemical stability of water leads to parasitic reactions (Fig. 31), such as hydrogen and oxygen evolution reactions (HER and OER), which reduce the Coulombic efficiency (CE) of the charge-discharge cycle.<sup>148</sup>

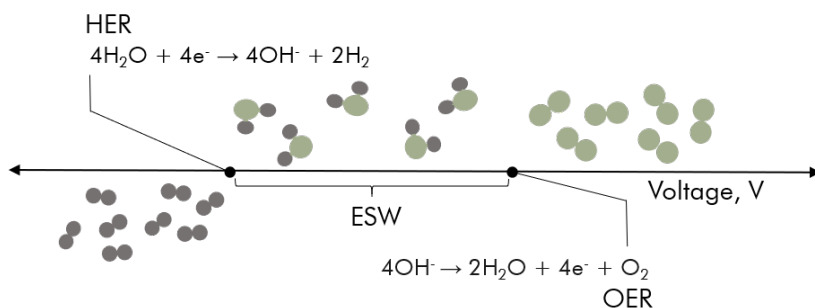


Figure 31. Water electrochemical stability window and two major parasitic reactions HER and OER.

Additionally, these reactions cause local pH changes that, over time, deteriorate the active material, compromising the cycle life stability of the electrodes.<sup>132,149</sup> Furthermore, hydrogen gas formation can result in unwanted increase in internal pressure, potentially causing the cell to rupture.<sup>150</sup> Different pathways such as growing a protective layer, adjusting pH, using highly concentrated “water in salt” (WIS) electrolytes, or restricting oxygen

access to the electrode are employed to address this problem (Fig. 32).<sup>151–154</sup> However, these approaches are not free from drawbacks: growing a protective layer requires costly and complicated postproduction procedures, high pH can be deteriorating for electrode active materials and there is currently no reported satisfactory gas evolution inhibition for common non-toxic and cheap salts.

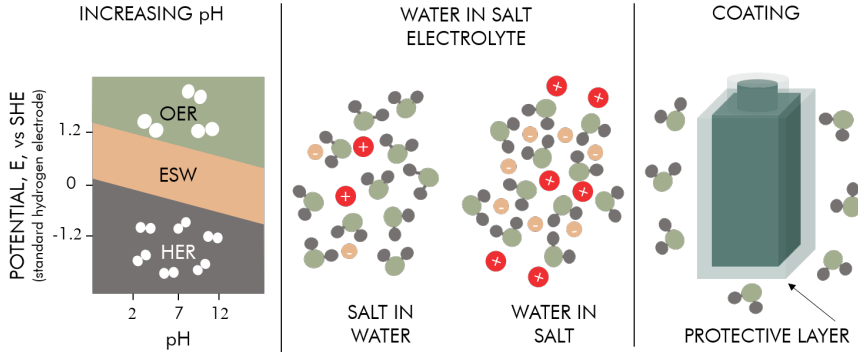


Figure 32. Common strategies for water ESW expansion: changing of pH, “water-in-salt” electrolytes, and protective coatings.

### 3.2.1. Aqueous electrolytes

Despite their unquestionable superiority over organic electrolytes in terms of conductivity and safety, aqueous electrolytes have not yet realized their full potential in practical applications due to parasitic reactions competing with sodium ion de/insertion.<sup>155</sup> Theoretically, NTP, as an active material, is particularly susceptible to HER as the redox potential of the  $\text{Ti}^{+3}/\text{Ti}^{+4}$  pair ( $\sim -1.25$  V vs  $\text{Hg}/\text{Hg}_2\text{SO}_4$ ) lies on the edge of water stability window:



In practice, however, the effects of HER towards degradation are minimal compared with pH increase occurring over GCD cycling due to the oxygen reduction:<sup>156</sup>

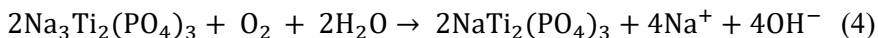


or



Chemical oxygen reduction reaction (ORR) has recently been found to be responsible for the local pH rise and consequent degradation, resulting in

diminished performance and lifespan of the cell.<sup>157,158</sup> Typically, it is a slowly occurring process accommodated by the surfaces commonly present in electrochemical cells such as stainless steel, carbon, titanium, etc. It is highly likely, that the presence of  $Ti^{III}$  species in the charged state of NTP mediates this process, which explains rapid self-discharge and compromised efficiencies at slow GCD cycling rates.<sup>132</sup> Chemical ORR can be written down as follows:



This reaction can be prevented by restricting the access of oxygen species, which is abundant in naturally aerated electrolytes, to the surface of the electrode. This is well illustrated by voltage profiles of GCD cycling and corresponding local pH changes presented in Fig. 33. During the GCD cycling pH was monitored by placing microelectrode tip in close proximity to the surface of working electrode. This way the interferences that could possibly arise from processes happening locally at the surface of counter electrode were avoided. In order to eliminate the oxygen from electrolyte, the cell was purged with  $N_2$  gas for 4 h prior to cycling. Forced convection was avoided by keeping the gas flow as low as possible during cycling. In the experiment carried out in ambient air conditions (Fig. 33 a) in the first charging cycle the pH showed a rapid increase up to  $\sim 9$  followed by a sudden drop to  $\sim 7.5$  once the charging plateau was reached. Such behaviour is believed to be caused by the consumption of dissolved oxygen at the electrode-electrolyte interface by electrochemical oxygen reduction. Another jump in pH appearing towards the end of charging stage can be attributed to either HER or chemical ORR. Subsequently, pH dropped and remained constant during the discharge stage. In the following 20 charge-discharge cycles the similar behaviour is observed with pH jump becoming less and less pronounced, until pH reaches  $\sim 10.5$ . In case of  $N_2$  gas-sparged electrolyte (Fig. 33 b), the growth in local pH was steady and slow from  $\sim 5$  to  $\sim 8.5$  with small bumps attributable to HER and/or some residual oxygen participating in ORR. The absence of other sorts of peaks indicates a strong contribution of ORR towards the rise of local pH and self-discharge processes. Bumps in pH observed in aerated electrolytes are proportional to the fraction of  $Ti^{III}$  which readily reacts with oxygen and promotes self-discharge. The subsequent pH saturation, likely, arises from NTP capacity loss and self-limiting nature of (4) reaction.

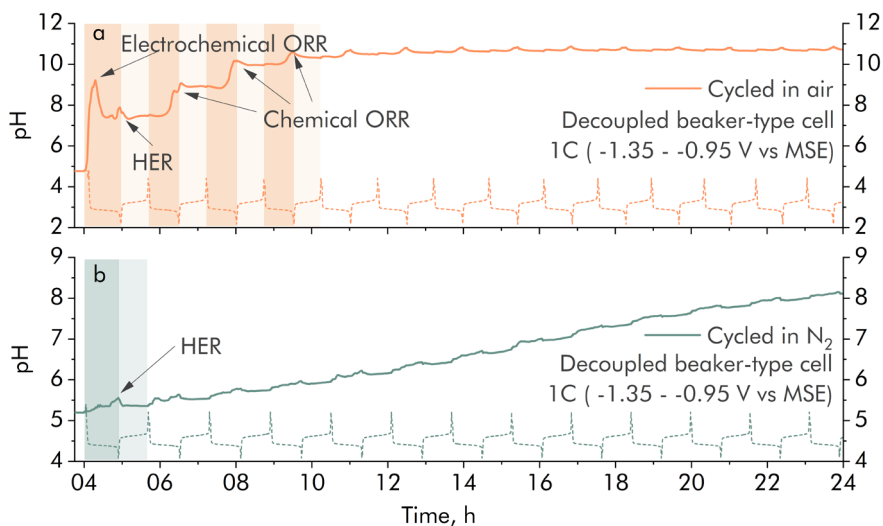


Figure 33. Potential profiles and local pH in (a) naturally aerated and (b) in  $\text{N}_2$ -sparged 1 M  $\text{Na}_2\text{SO}_4$ .

This theory is further supported by the GCD data displayed in Fig. 34. The efficiency in inert gas sparged setup reached  $\sim 99\%$  in 10 cycles and stayed stable in the next 90 cycles. The capacity fade was only 6%. This supports the idea that oxygen elimination strongly inhibits parasitic reactions leading to pH changes and capacity loss. Air-exposed electrode, however, demonstrated only around 92% of CE and 24% of initial capacity after 100 cycles. It is obvious that pH is detrimental to the electrode performance.

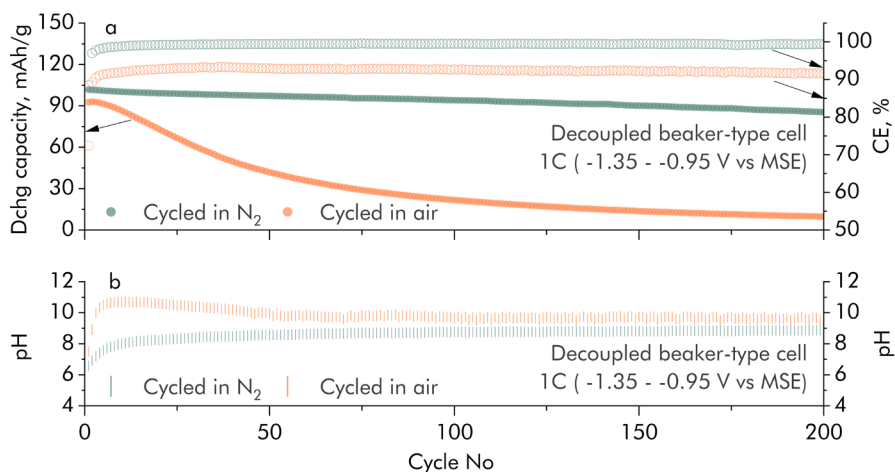


Figure 34. (a) GCD cycling performance of NTP-based electrodes in naturally aerated and  $\text{N}_2$ -sparged 1 M  $\text{Na}_2\text{SO}_4$  (aq) and (b) their local pH.



In this study, we investigate the effects of local pH changes on active material degradation and cycling stability of NTP-based electrodes. Fig. 35 displays GCD cycling results in three buffered electrolytes with pH 4, 7, and 10. The results shown in Fig. 35 a) indicate that at the lowest pH, the initial efficiency is very low ( $\sim 24\%$ ), however, it reaches  $\sim 75\%$  after 100 cycles. It is, with great certainty, a result of hydrogen evolution because bubble formation ( $H_2$ ) was visually observed in the presence of minimal oxygen amounts. The *post mortem* investigation of electrolyte solution showed an increase of pH to 5.8, which indicates the consumption of buffer capacity and explains consequent increase in CE, which inhibits the HER. It looks like the gas evolution introduced some limitations to mass transport; hence, initial capacity is much lower than theoretical. However, capacity retention of 90% symbolizes great cycling stability. From the higher CE exhibited by a sample in neutral pH (Fig. 35 b) it is obvious that contribution of HER is less pronounced. Notably, unbuffered neutral electrolyte (Fig. 34 b) reached the pH of 8.5 in the first 20 cycles. Moreover, the buffered electrolyte promoted higher capacity (99%) retention in comparison with the unbuffered one. In the pH 10 experiment, CE is close to 100% during the entire experiment (Fig. 35 c). This is a result of virtually no HER occurring thanks to the elevated pH value. Additionally, no pH drift of electrolyte was recorded after the investigation. The fact that almost half of the capacity was lost during the 100 cycles suggests that alkaline pH is the main contributor to NTP electrochemical performance in aqueous media. Summing up, this investigation suggests that electrolyte buffering is viable method for prevention of capacity fade in NTP electrodes. However, buffering is not considered ideal, especially in real-life electrolyte-starved devices, where both electrodes have to be taken into consideration.

In order to estimate how much of capacity loss is due to material degradation, the content of NTP phase was evaluated by recording *post mortem* powder XRD patterns and EDX analysis at the different stages of cycling at 1C rate in pH 10 buffered and inert gas sparged electrolyte. The amount of NTP was quantified analysing the ratio of Ti to Hf.  $HfO_2$  a highly crystalline and inert material was used as an inner standard. Fig. 36 presents summarised results of investigation as well as GCD cycling performance of the electrode. It can be concluded that NTP phase deteriorates linearly, around 85% of crystalline NTP is retained after 200 cycles. These findings do not correlate well with capacity loss identified by GCE (Fig. 36 a).

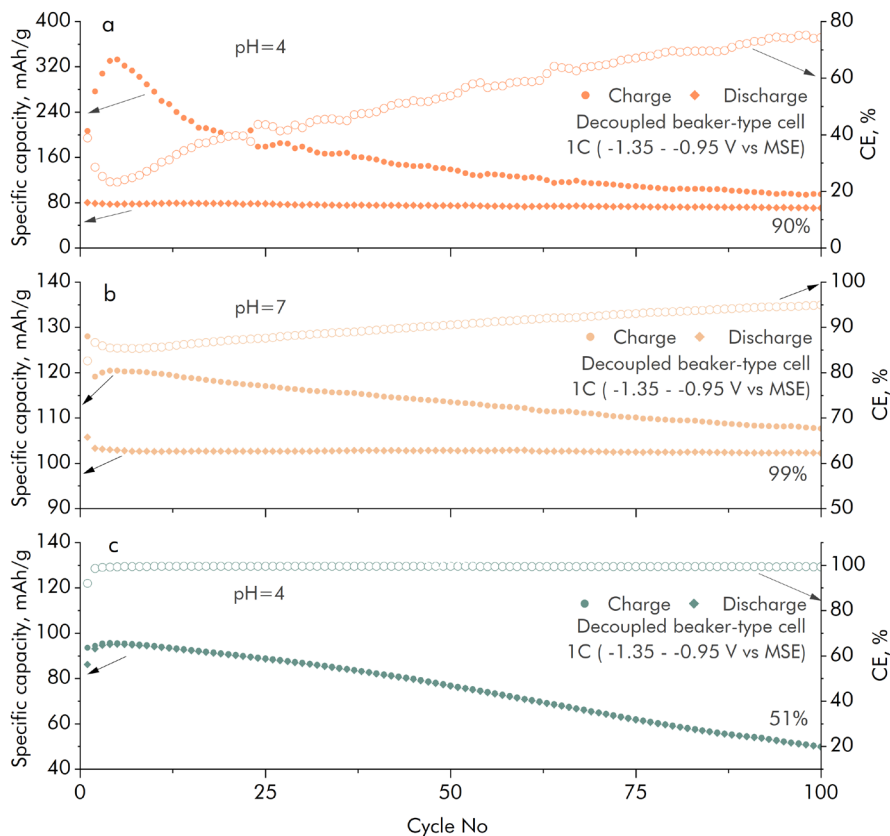


Figure 35. GCD cycling results of NTP in  $N_2$ -sparged and buffered at (a) pH = 4, (b) pH = 7 and (c) pH = 10 1M  $Na_2SO_4$  electrolytes.

Peculiarly, EDX Ti/Hf element ratio analysis (Fig. 36 b) revealed that titanium content in the electrode is almost constant. The combined results suggest that capacity loss is neither directly proportional to decomposition nor to dissolution into the electrolyte. To the opposite, it is caused by the formation of insoluble Ti-rich phase on the surface of the electrode. The layer growth causes blockage on the surface of electrochemically active phase, resulting in contact loss, hence, capacity loss. Although indirectly, aqueous interphase formation consisting of Ti rich phases such as  $Ti(HPO_4)_2 \cdot H_2O$  is backed by previous investigation of surface carbon where NTP electrodes are compared to NVP anodes. These findings suggest that exploring the controlled growth of this layer could enable achieving the full potential of NTP for aqueous applications.

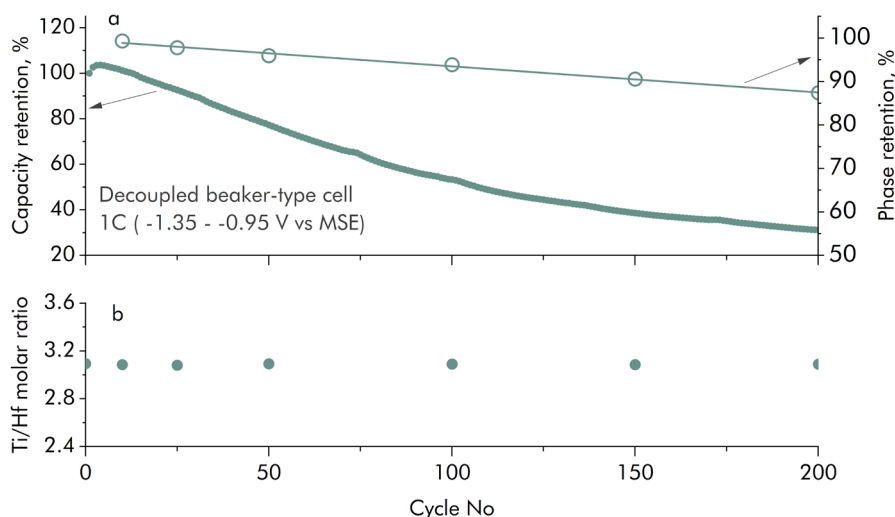


Figure 36. (a) Amount of NTP crystalline phase as obtained by XRD along with relative capacity retention and (b) EDX obtained Ti/Hf atomic ratios.

### 3.2.2. Hybrid aqueous electrolytes

Literature suggests that previously discussed unfavourable parasitic reactions induce most of the damage while ‘unbounded’ water is the prevailing component of electrolytes.<sup>159</sup> Implementing co-solvents in aqueous electrolytes facilitates broader operational voltage range by restraining water molecules with hydrogen bonds formed between co-solvent and water (Fig. 37).<sup>160</sup> As a result, water activity drops significantly, therefore, water-assisted reactions are substantially reduced.<sup>161,162</sup> Safe and cheap glycerol with three -OH groups per molecule as well as greatly polar DMSO have the potential to be employed as co-solvents.<sup>163</sup>

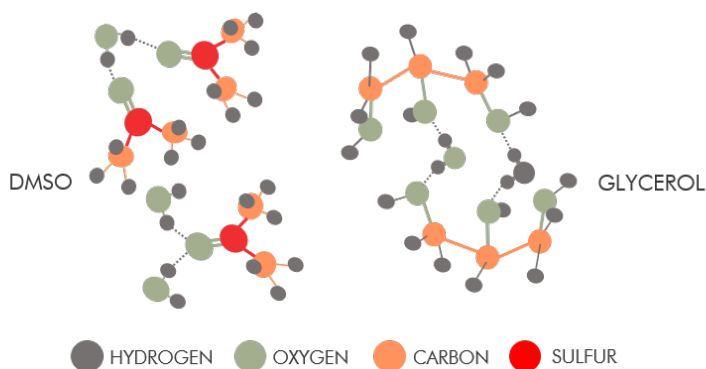


Figure 37. Interactions between water and crowding molecules.

For this investigation two series of electrolytes based on two co-solvents (CS) dimethyl sulfoxide (DMSO) and glycerol (GLY) are prepared by dissolving 1 M NaNO<sub>3</sub> (defined as CSx, where x represents the mol% of CS in the solvent). For comparison, 1 M NaNO<sub>3</sub> aqueous solutions are also prepared and denoted as H<sub>2</sub>O. For convenience, the compositions of CSx electrolytes are shown in Table 3.

**Table 3.** Compositions of aqueous hybrid electrolytes aqueous electrolytes.

Sample name	Salt	CS	Solvent, (mol%)	
			CS	Water
H <sub>2</sub> O	1 M NaNO <sub>3</sub>	-	0	100
DMSO10	1 M NaNO <sub>3</sub>	DMSO	10	90
GLY10		GLY		
DMSO25	1 M NaNO <sub>3</sub>	DMSO	25	75
GLY25		GLY		
DMSO40	1 M NaNO <sub>3</sub>	DMSO	40	60
GLY40		GLY		
DMSO50	1 M NaNO <sub>3</sub>	DMSO	50	50
GLY50		GLY		
DMSO60	1 M NaNO <sub>3</sub>	DMSO	60	40
GLY60		GLY		

In the first part of the electrochemical study, hybrid electrolyte solutions are investigated in a half-cell, focusing on how NTP-based anode is affected. In the second part, full cells with Na<sub>1.86</sub>Fe[Fe(CN)<sub>6</sub>] · 2.28H<sub>2</sub>O material as cathode are assembled and their electrochemical performance is evaluated.

Initially, the physical and electrochemical properties of hybrid electrolyte solutions were studied. The viscosity and conductivity values of the series are presented in Fig. 38 a-b. The measured ionic conductivity of pure aqueous electrolyte is 47.9 mS cm<sup>-1</sup>, which is higher than the mixed composition electrolytes. Although GLYx series show a noticeable drop in conductivities compared with water, the 60GLY sample still reaches a 1.08 mS cm<sup>-1</sup> value, which is comparable if not higher than conductivities reported for other “water in salt” electrolyte solutions.<sup>164–166</sup> Moreover, the corresponding viscosity of 171 mPa s is well within the range reported for some ionic liquids-based electrolytes.<sup>167</sup> The investigation of DMSO series shows, that conductivity follows the same downward trend with the increase of co-solvent (from 47.9 to 9.88 mS cm<sup>-1</sup>). At the same time, the rise in viscosity is substantially less evident (from 1.1 to 5.7 mPa s) than that of the glycerol series.

Dashed lines in Fig. 38 c) show water activity dependence on the molar composition of the mixture taken from literature and the points represent the activity values for electrolyte series obtained in this investigation. The diagrams reveal that, within the range of molar composition of the series, water activity decreases more than twice (from 1 to 0.41 and from 1 to 0.32) for both co-solvents. Glycerol shows slightly stronger interactions, hence, stronger effect on the water activity in the mixtures. Overall, these findings indicate great potential of such mixtures for applications in water decomposition-resistant electrolytes.

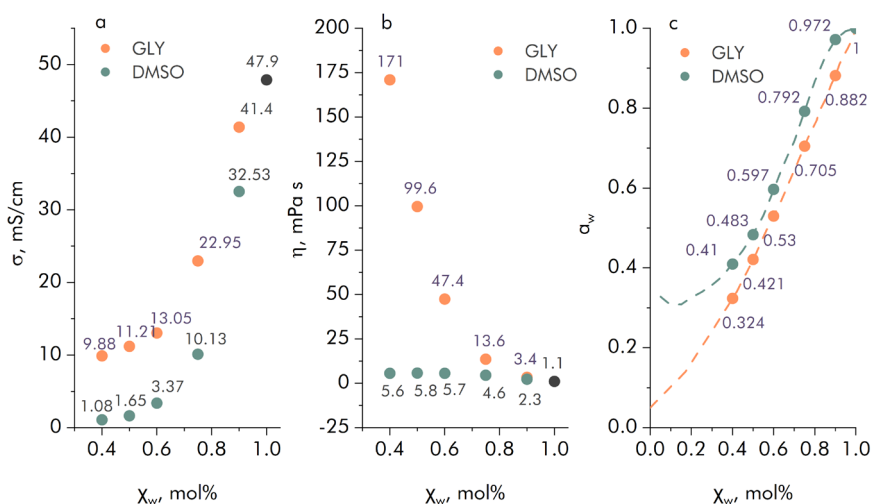


Figure 38. Physicochemical characterization of the electrolytes: (a) conductivity of electrolytes at 25 °C, (b) viscosity of electrolytes, (c) relative water activity at different co-solvent contents as reported in literature.<sup>168,169</sup>

The relationship between the composition of electrolytes and their electrochemical stability was established by the linear sweep voltammetry (LSV). Possible transport limitations caused by increased viscosity were eliminated by using a rotating disc electrode (RDE) during investigation. As shown in Fig. 39, two simultaneous reactions (ORR and HER) are taking place on the cathodic side, hence, HER onset potential can hardly be quantitatively expressed. However, it is obvious that with increasing the substitution with co-solvents, the potential shifts towards more negative potentials. These results are in good agreement with the studies of water activity (Fig. 38 c) and indicate that decreased water amounts, hence, activities, extend ESW for electrolyte solutions. Moreover, the addition of glycerol further expanded the stability window by noticeably pushing oxygen evolution potential to more

positive values. This shift might be explained by the viscosity input towards the onset of OER, which persisted even at 1000 rpm. These results imply that electrolyte stability range can be significantly broadened ( $\sim 2\text{ V} \rightarrow \sim 3.5\text{ V}$ ) as a result of intramolecular bonding.

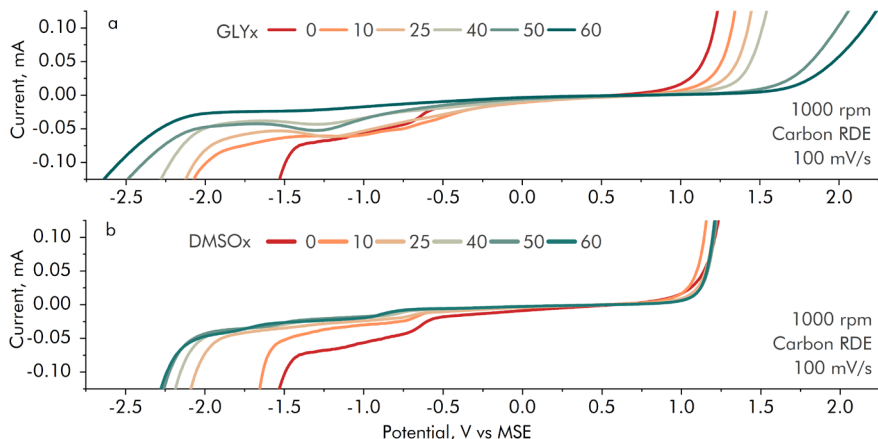


Figure 39. ESWs of (a) GLY- and (b) DMSO-based electrolytes determined by LSV tests at  $100\text{ mV s}^{-1}$  and 1000 rpm of RDE.

To understand the improved stability and the rearrangement of H-bonding in electrolytes, Raman spectroscopy in the OH stretch region was employed (Fig. 40). Vibrational spectra of water in the OH-bonds stretching region ( $2800\text{--}3800\text{ cm}^{-1}$ ) are very complex because of the presence of symmetric and asymmetric vibrations and Fermi resonances. In addition, these bands are perturbed by hydrogen bonding interactions. In this spectral region aqueous  $1\text{ M NaNO}_3$  consists of three distinctive bands at  $3262\text{ cm}^{-1}$  (band I),  $3451\text{ cm}^{-1}$  (band II), and  $3599\text{ cm}^{-1}$  (band III). Band I is dominated by Fermi resonance resulting from the intramolecular (coupling between the OH symmetric stretching and the overtone of the HOH bending) and intermolecular vibrational coupling (mutually interacting water molecules). Band II is characteristic of asymmetric fragmentary hydrogen bonding of water molecules. Band III is associated with stretching of OH which forms no hydrogen bonds.<sup>170</sup> The introduction of DMSO (Fig. 40 a) into the solution resulted in two additional peaks attributed to symmetric ( $2925\text{ cm}^{-1}$ ) and Fermi resonance interaction band coupled with asymmetric stretching vibration ( $3012\text{ cm}^{-1}$ ) of  $\text{CH}_3$  groups. In the case of glycerol (Fig. 40 b) the peaks were assigned to symmetric ( $2886\text{ cm}^{-1}$ ) and asymmetric stretching of  $\text{CH}_2$  coupled with Fermi resonance bands ( $2945\text{ cm}^{-1}$ ). Subsequent deconvolution of the spectra produced 3 peaks in the studied region until the threshold of 40 mol%

and 25 mol% was not reached for GLY and DMSO series, accordingly. The intensity of the band III is reduced with the increasing molar fraction of co-solvent indicating decreased relative population of very weakly H-bonded water in the hydration shell. In the region of the OH stretch band I a noticeable decrease in intensity is observed for glycerol and even more so for DMSO. It is important to note that the contribution of OH groups is unquantified in present analysis, hence, the higher intensity of band I is highly likely due to the presence of OH in the co-solvent itself. Generally, lower intensity of band I could be attributed to reduced intra- and inter-molecular vibrational coupling of water in the hydration shells of co-solvents.

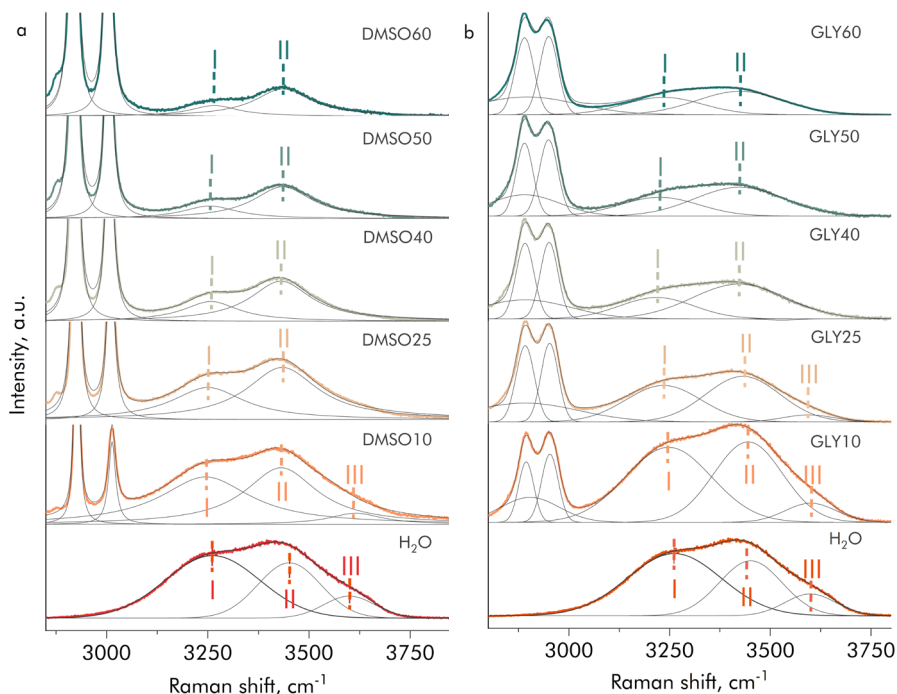


Figure 40. Raman spectra of (a) DMSOx and (b) GLYx electrolytes between 2750 and 3750  $\text{cm}^{-1}$ .

The calculated ratios of the areas under the bands I and II presented in Fig. 41 a agree well with the earlier observations, implying that water was efficiently bound by co-solvent molecules. A deeper look into the band shifts (Fig. 41 b) provides the essential insights about perturbations in water bonding. Both O-H stretching bands are shifting towards low frequency wavenumbers at  $X \leq 25$  mol% and  $X \leq 40$  mol% for DMSO and GLY, respectively. The red shift is indicating the strengthening of the intermolecular hydrogen bonds at the expense of weakening of the

intramolecular O-H stretching.<sup>171</sup> This is a result of stronger H-bonds forming between water and co-solvent than other water molecules. Hence, as the critical threshold is reached, co-solvent molecules do not replace water in “orderly” tetrahedral structure, but dismantle it leading to the severed connection between co-solvent and water.<sup>172</sup> Literature suggests that 1DMSO-2H<sub>2</sub>O aggregates with strong H-bond networks between water molecules are dominant in water-rich DMSO solutions.<sup>173</sup> The shift of the wavenumbers in the opposite direction is assumed to be indicative of transition when 2DMSO-1H<sub>2</sub>O aggregates prevail over 1DMSO-2H<sub>2</sub>O in the electrolyte solutions. Glycerol-water mixtures exhibit very similar band shifting trends, presumably, also caused by the changes in prevailing agglomerate type phase switch.<sup>174</sup>

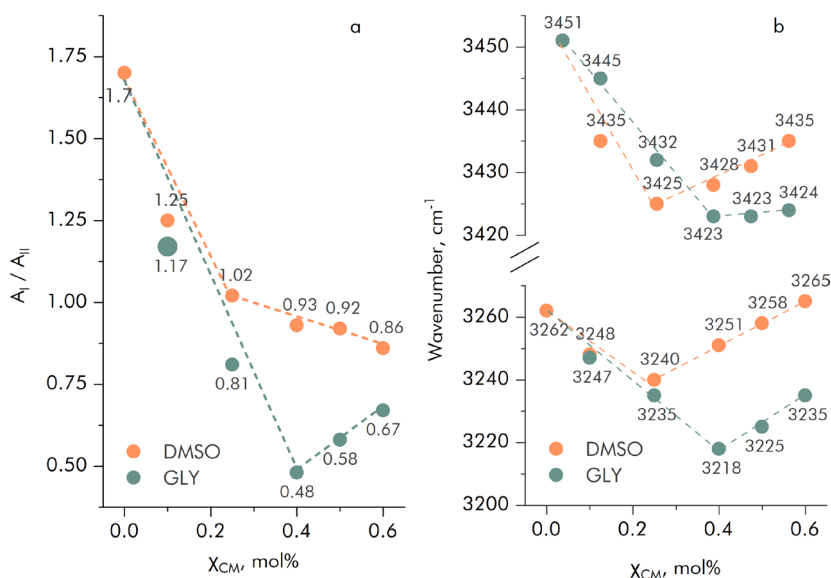


Figure 41. (a) Ratio of I and II calculated areas and (b) I and II band wavenumber shifts.

### Half-cells

The benefits of employing co-solvents are best illustrated by the electrochemical performance investigation. Fig. 42 a-b shows the GCD curves at a charge rate of 1C. The initial capacities as well as capacity retentions after 200 cycles are presented in Fig. 42 c. The results show that introducing more co-solvent results in better capacity retention in the range from 10 to 50 mol% for DMSO and from 10 to 40 mol% for GLY series. The retained capacity



after 200 cycles has greatly increased from 28% (without crowding compound) to 88% and 95%, respectively. The increase in GCD cycling stability is believed to be due to suppression of the detrimental water-assisted reactions:



and



Both reactions are responsible for the local pH increase and are contributing to the irreversible capacity fade.<sup>175</sup> The mitigation might be happening due to restricted access to the inner double layer surface and unavailability of the adsorption sites as they are occupied by co-solvent molecules. Alternative explanation would be the inhibition of water decomposition due to stronger hydrogen bonds formed between water and co-solvent than in-between water molecules.<sup>176</sup>

An opposite behaviour was observed once the threshold of the co-solvent has reached 60 mol%; where rapid capacity deterioration ensued for DMSO-H<sub>2</sub>O electrolyte. The electrode was observed *post mortem* and it was revealed that substantial swelling and delamination from the stainless-steel mesh took place. Solubility of PVDF in DMSO have only been reported at elevated temperatures; however, it is highly possible that once a certain level of ‘free’ DMSO is reached, the gradual dissolution of electrode occurs causing unpredictable capacity loss.<sup>177</sup> The prolonged exposures to unbounded DMSO during GCD cycling led to swelling of the PVDF. Changes in volume occurring during swelling conditioned the loss of the contact with a metal mesh. The galvanostatic cycling experimental setup used for this investigation was not suitable to characterize 60GLY, a sample with high viscosity and resistance, at the rate of 1C.

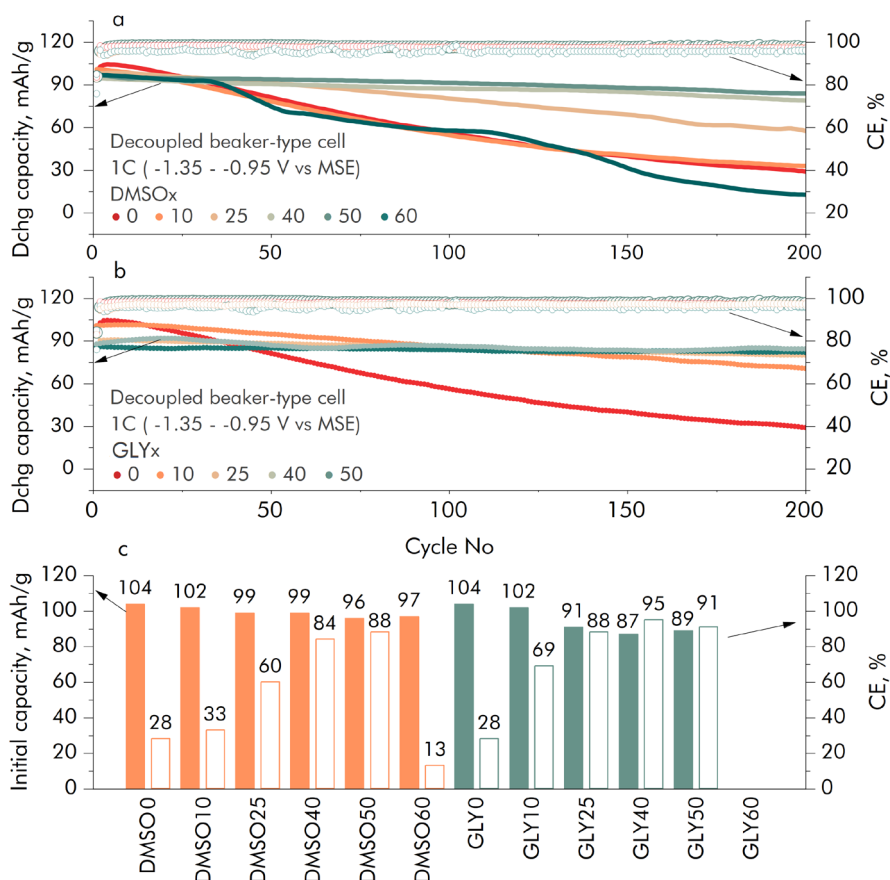
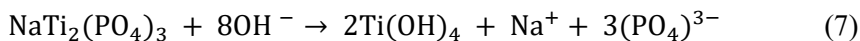


Figure 42. Galvanostatic charge/discharge cycling performance in (a) DMSO and (b) GLY series a 1C rate and initial capacity with capacity retentions after 200 charge/discharge cycles of (c) DMSO and (d) GLY.

The enhanced cyclability has been further confirmed by NMR investigation. The most representative electrolytes were collected after GCD cycling investigation and examined for the presence and concentrations of phosphates - a signature sign of electrode degradation as a result of electrochemically catalysed dissolution, which could be described by reaction:



The results in Fig. 43 suggest that less deterioration occurs when co-solvent is present. Notably, there is no linear correlation between concentration of phosphate species and the fraction of substituted water, which repeatedly confirms the synergetic effect of a few simultaneously happening processes on suppression of NTP dissolution. Interestingly, greater

dissolution was observed in the samples with better capacity retention, implying that chemical dissolution is only partially responsible for the capacity loss in aqueous environment. Further deterioration is assumed to be due to the disruption of electronic pathways inside the electrode as a result of formation and growth of interphasial layers. Raman spectroscopy investigation (Fig. 41 b) suggested that DMSOx forms stronger intermolecular hydrogen bonds than GLYx at substitution levels lower than 25 mol%, thus, are more resistant to electrochemical water splitting and subsequent degradation of the active material.

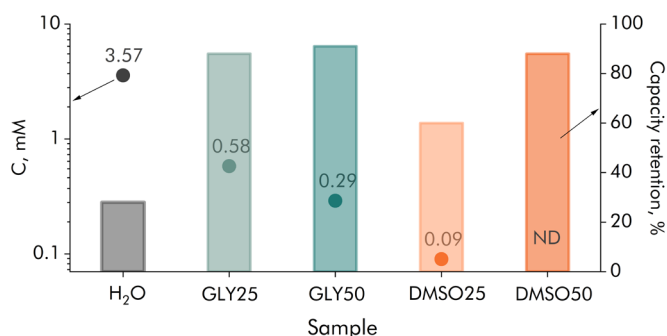


Figure 43. NMR-determined concentration of  $(\text{PO}_4)^{3-}$  ions in electrolytes after 200 cycles of GCD. Estimated using 60 mM/L ADP solution in  $\text{H}_2\text{O}$ .

More benefits of improved stabilities are revealed in a self-discharge (SD) study (Fig. 44 a-b). Introducing the co-solvent contributes to significantly prolonged SD times for DMSOx (from 23 h to 160 h at  $x=50$ ) and even more so for GLYx electrolytes (from 23 h to 865 h at  $x = 50$ ). The gradual consumption of charge in the charged state in water-based batteries is mostly attributed to the diffusion of ions and/or previously mentioned reactions with water itself.<sup>111</sup> While substituting water with DMSO alleviates only the effects arising from contact with water, glycerol alters stability by additionally impeding the diffusion-controlled Faradaic reaction. Higher viscosities of GLY slow down diffusion of interphasial charges and result in slower charge redistribution.<sup>178</sup> SD duration dependence on the degree of water substitution is presented in Fig. 44 c-d. Though both electrolytes seem to positively affect the stability, the slope values reveal that reorganized networks of hydrogen bonds work better when accompanied with transport restriction of charged species.

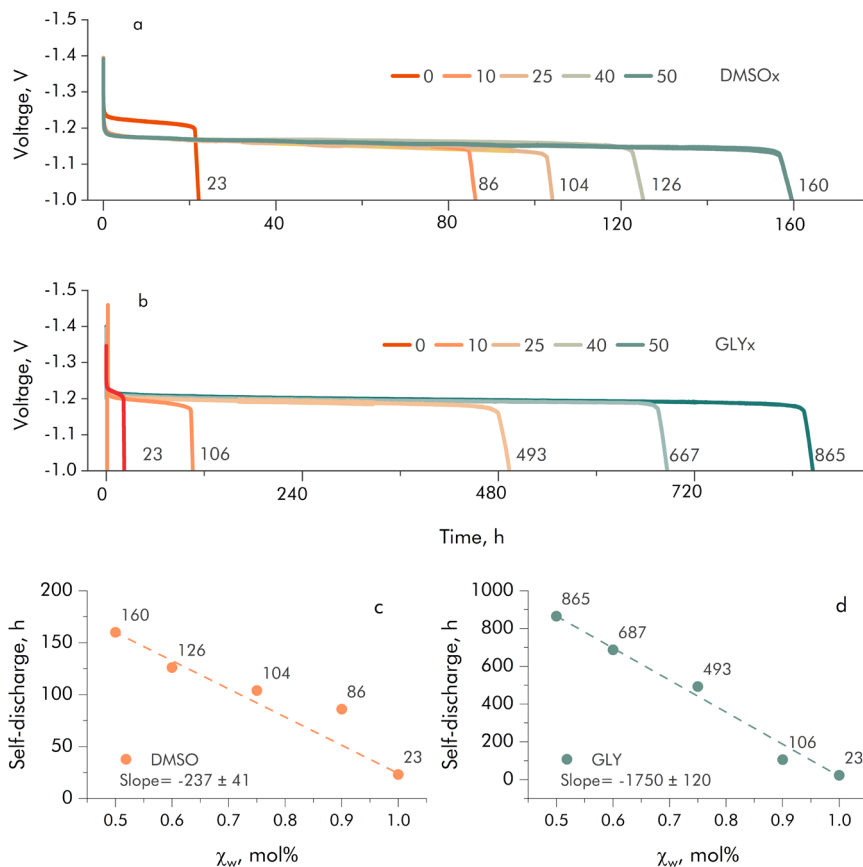


Figure 44. Self-discharge profiles for (a) DMSO and (b) GLY series, and plotted dependence of SD time on water fraction in DMSO (c) and GLY (d) electrolytes.

As the effect of hybrid electrolytes on negative electrode was established, the question is if it bears the same benefits for cathodes and overall battery performance. Electrochemical study with a  $\text{Na}_3\text{V}_2(\text{PO}_4)_2\text{F}_3$  (NVPF) cathode – highly unstable in aqueous media - was carried out in the best-performing electrolytes from both series (DMSO50 and GLY50). Fig. 45 presents the results of GCD cycling for NVPF electrode. The results suggest that although the capacity decays at a much slower rate (Fig. 45 a) when a co-solvent is present, the overall stability (Fig. 45 b) is far from satisfactory (from 2.7% to 12.6% and 30.5 %). Moreover, the initial capacities (Fig. 45 b) are far from the theoretical (128 mAh/g) value. Apparently, decreased water activity does not contribute sufficiently to suppressing the dissolution of vanadium into electrolyte. It is concluded that further manipulations with electrolyte in order

to control water activity are needed to enable the full potential of NVPF electrodes in ASIBs.

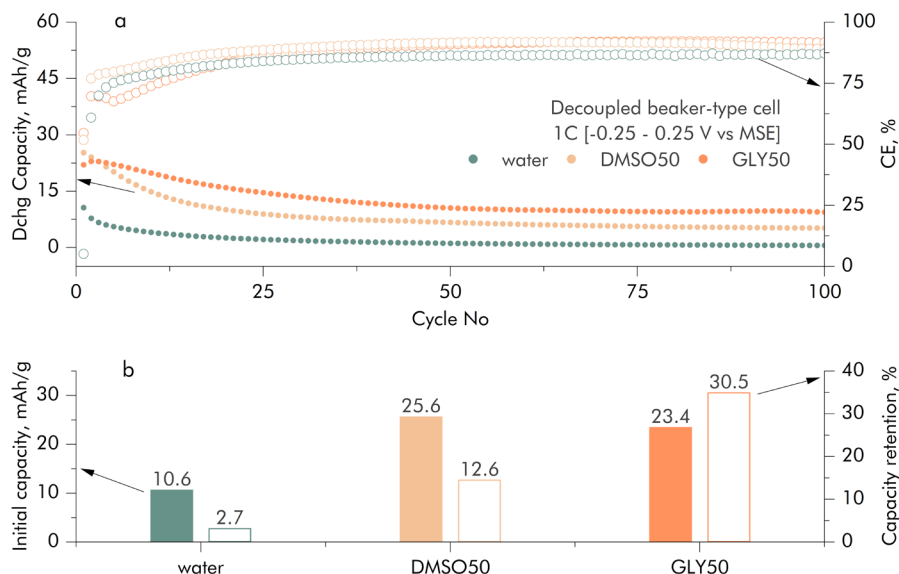


Figure 45. (a) GCD cycling performance of NVPF electrode in different electrolytes at 1C rate and (b) initial capacity with (c) capacity retentions after 200 charge/discharge cycles.

The same investigation was performed with  $\text{Na}_{1.86}\text{Fe}[\text{Fe}(\text{CN})_6] \cdot 2.28\text{H}_2\text{O}$  (NaFeHCF) – a cathode material that has proven to be more stable in aqueous systems. As in the previous investigation, the positive effect on stability was revealed (Fig. 46 a). All three samples delivered similar initial capacities (Fig. 46 b); however, their cycling stability was extremely different. DMSO50 has increased the capacity retention from 38.7% to 73.7% and GLY50 to 108%. A repeated GLY50 GCD cycling experiment confirmed that there is a slight upward trend in capacity values. It might be that the suppression of OER allows to reach the  $\text{Fe}^{2+}/\text{Fe}^{3+}$  reaction which often overlaps with oxygen evolution. The additional capacity comes from this electrochemical reaction.

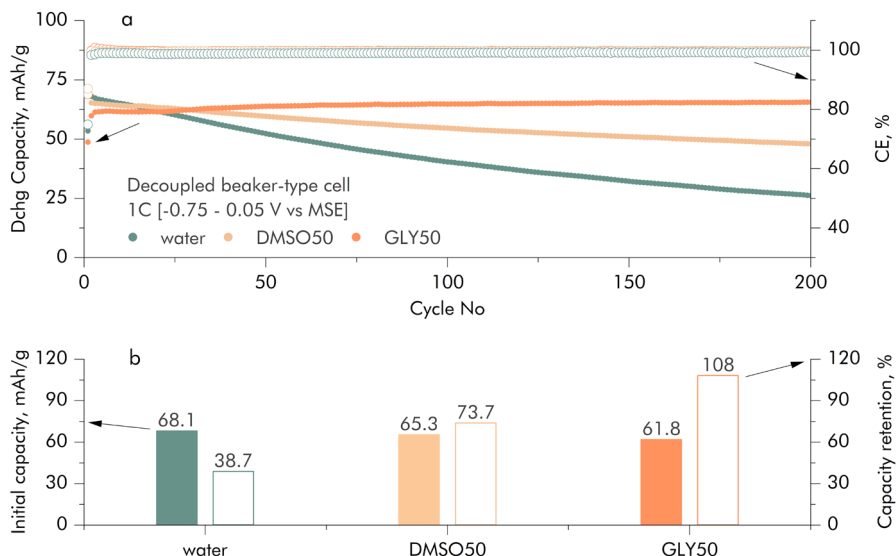


Figure 46. (a) GCD cycling performance of NaFeHCF electrode in different electrolytes at 1C rate and (b) initial capacity with (c) capacity retentions after 200 charge/discharge cycles.

### Full cells

The full cell investigation was inspired by optimistic results of GCD cycling of NTP and NaFeHCF in half-cells. Coin cells were assembled following a procedure described in experimental section with surplus positive electrode ( $\text{NaFeHCF}_{(\text{capacity})} / \text{NTP}_{(\text{capacity})} = 1.33 - 1.36$ ). The overcapacity of cathode is meant to mitigate the parasitic reactions and ensure decent cycling stability for this experiment.<sup>179</sup> This is not ideal in terms of battery design as unnecessary deadweight is introduced into the system; however, it is more suited to demonstrate the effect of co-solvent electrolytes.

Fig. 47 demonstrates the differences in GCD cycling performance between different cathode/anode ratios in full ASIBs in the cycling range of 0.01 – 1.7 V. It is obvious that excess of cathode has beneficial effect on the discharge capacity as well as on the Coulombic efficiency of the assembled full cells. The sample with anode overcapacity (green) is characterized with lowest output capacity and remarkably low efficiency of 27% after 100 cycles, indicating that parasitic side reactions are dominating the charging stage of battery cycling. Batteries with cathodic overcapacity (yellow and orange) demonstrate more or less similar electrochemical behaviour; however, sample with higher P/N ratio exhibits better discharge capacities and higher efficiency (88% vs 79%).

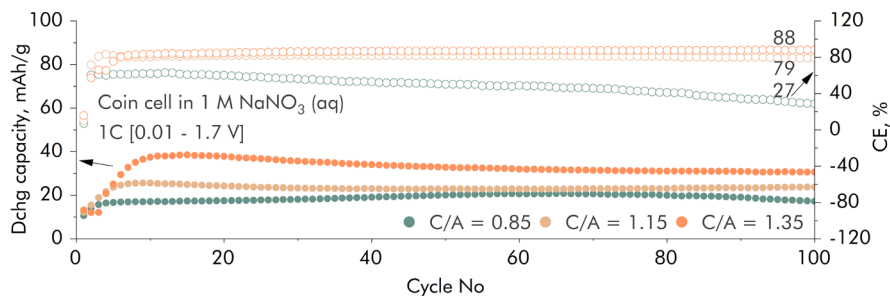


Figure 47. GCD cycling performance of NaFeHCF/NTP full-cell with different cathode/anode ratios at 1C rate.

The GCD investigation of batteries in hybrid electrolyte solutions was carried out using voltage ranges of 0.01 – 1.7/1.8/1.9/2 V in order to obtain more data about cycling stability close to water splitting potentials (Fig. 48). The sample cycled in purely aqueous electrolyte (Fig. 48 a) starts at efficiency around 85% and very low discharge capacities, which improve with widening the voltage cut-off; however, it gives a boost to oxygen related reactions, which can be seen from dropping efficiency. At the end of charging, the parasitic reactions seem to have triggered rapid deterioration. While at low voltages the effect of DMSO (Fig. 48 b) is not too obvious, the ranges of 0.01 – 1.9 V and 0.01 – 2.0 V reveal substantially improved efficiencies (~85%) and great discharge capacity of more than 90 mAh/g. DMSO25 (Fig. 48 c) and DMSO50 (Fig. 38 d) both show enhanced efficiency in the entire range of voltages. DMSO50 achieves efficiency close to 100% in the initial step of voltage ramp cycling, and climbs up to 93% in the range 0.01 – 2.0 V. The results described above are as expected and in good agreement with previous investigations of water activity in hybrid electrolyte solutions revealing a great potential for co-solvents in electrolyte-starved cells, such as those produced commercially.

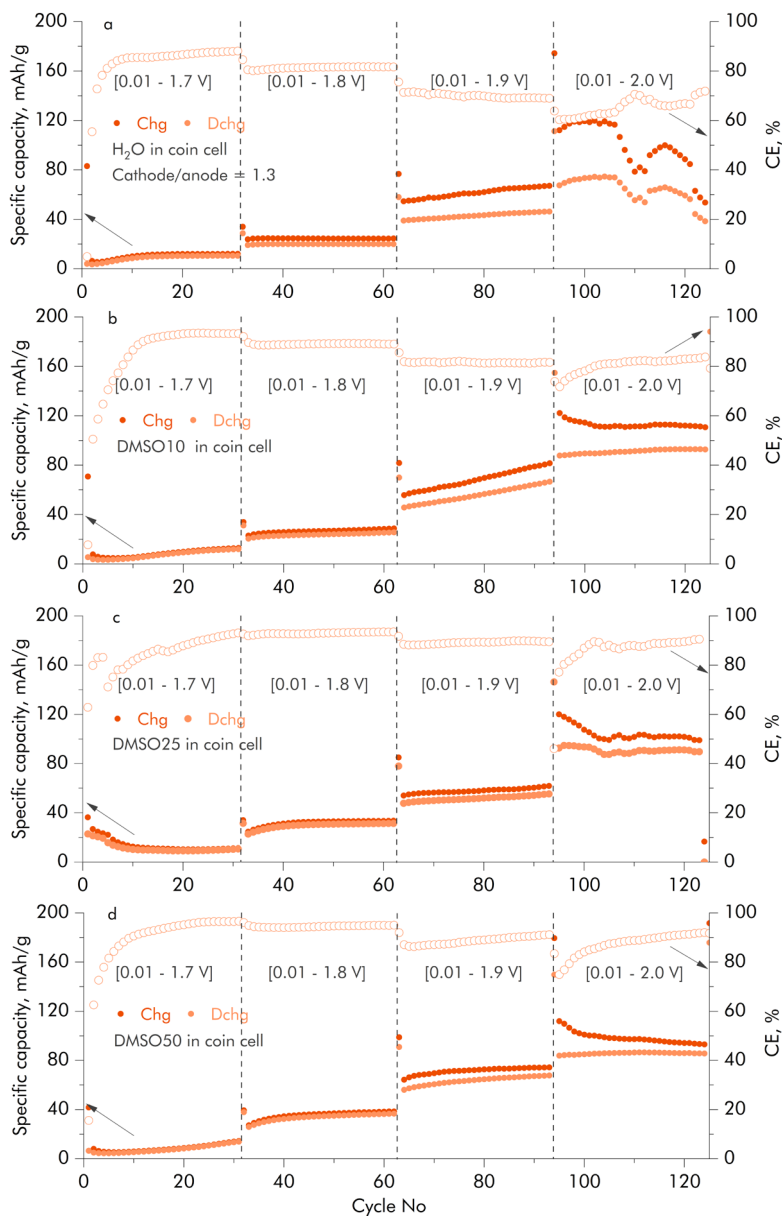


Figure 48. GCD cycling performance of NaFeHCF/NTP coin cell in (a) H<sub>2</sub>O, (b) DMSO10, (c) DMSO25, and (d) DMSO40 electrolytes at 1C rate.

Investigation with GLY series is presented in Fig. 49. The main trends seem to be the same, but efficiency in glycerol-based electrolytes seems to drop with each voltage cut-off and grows within 32 cycles. This indicates a larger input of side reactions during cycling. This, perhaps, might be explained by greater viscosities of this electrolyte solution series and more air dissolved



in it as a result. Despite that, efficiency higher than 90% is still achieved for GLY50 with 95% recorded in the range of 0.01 – 1.9 V. Similarly, to anodes, full batteries in GLY series are characterized by lower discharge capacities ( $\sim 80$  mAh/g based on anode for GLY50) which could be attributed to diffusion limitations induced by the higher viscosities.

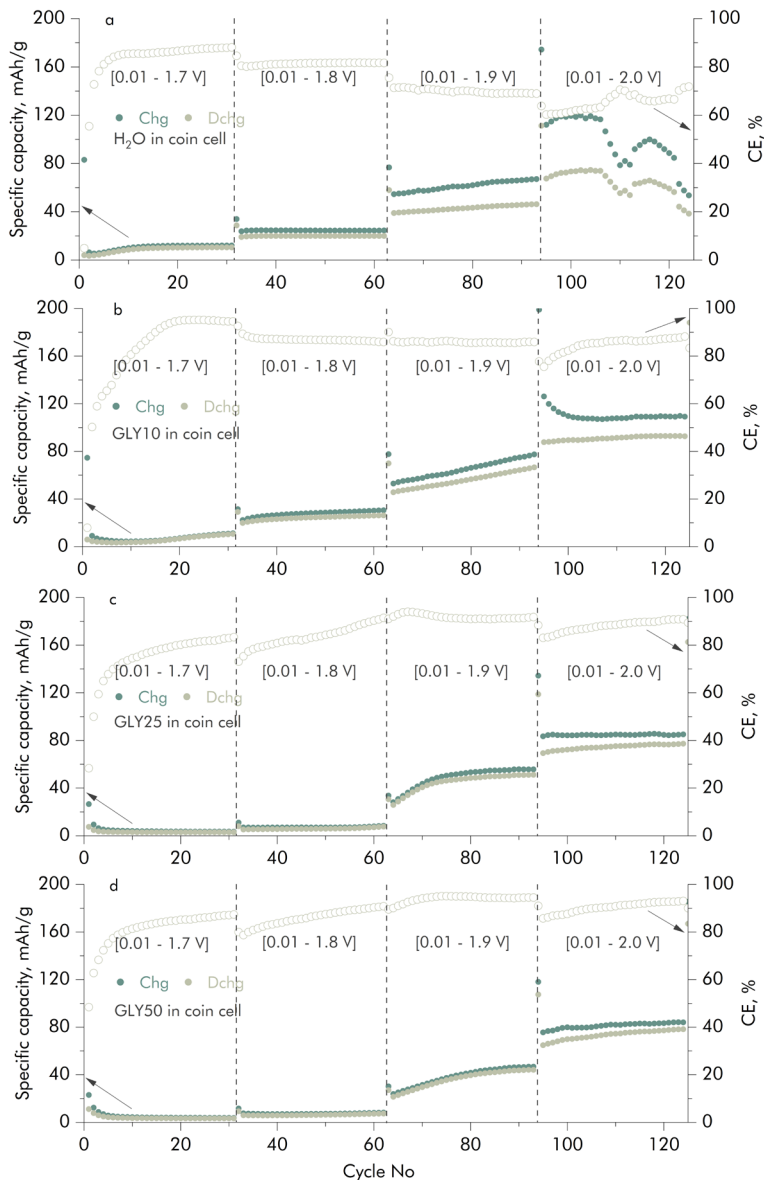


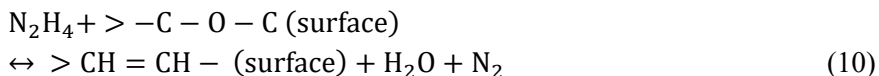
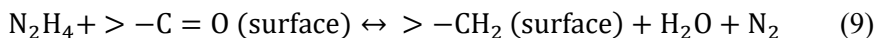
Figure 49. GCD cycling performance of NaFeHCF/NTP coin cell in (a) H<sub>2</sub>O, (b) GLY10, (c) GLY25 and (d) GLY40 electrolytes at 1C rate.

## Capacity balanced full-cells

In the previous section we showed that in full cells the effect of ORR becomes more pronounced with approaching the equal negative and positive electrode capacities. Though overcapacity of cathode is a reliable way of mitigating the ORR and consequent capacity degradation, it is highly impractical in terms of the deadweight introduced to the battery and higher manufacturing costs. The introduction of strong reducing agents, such as hydrazine, could help to achieve the balanced cells with  $N/P=1$  by reducing the dissolved oxygen in electrolytes. Hydrazine ( $N_2H_4$ ) has been widely used in industry as an anticorrosive additive due to its oxygen scavenging properties. Although it is labelled as a hazardous substance, it is considered relatively safe at low concentrations in aqueous solutions. Moreover, it is a sacrificial agent as it fully consumed when used in a well-sealed system.<sup>180</sup> In the aqueous cell hydrazine contributes to increased stability by reacting with dissolved oxygen:



and by reducing the carbonyl or epoxide groups present on the surface of carbon:<sup>181</sup>



Initially, the potential profiles are recorded for the first charging cycle of the negative and positive electrodes in order to determine the optimal amount of hydrazine in standard sulphate aqueous electrolyte between 0, 0.01, 0.02, 0.1, 0.15 mol%. The results presented in Fig. 50 indicate that increased content of  $N_2H_4$  affects the potential profiles in several ways. First of all, open circuit potential (OCP) gradually shifts to more negative regions. Secondly, increased content of hydrazine contributes to the disappearance of a feature at -0.6 V vs MSE, which is attributed to the reduction of carbonaceous phases, once the  $N_2H_4$  concentration threshold of 0.02 mol% is reached. Moreover, higher amounts of hydrazine lead to prolonged times required to reach the cathode potential plateau and shorter times required for anode potential to reach the plateau. The shift of OCP potential and a disappearance of the plateau are interlinked and can be explained by chemical reduction of the carbon surface by hydrazine. The variation of cathode potential, in turn, could be attributed

to the electrooxidation of the hydrazine. It has previously been reported that unprotonated form of hydrazine is electroactive, while its protonated counterpart ( $\text{N}_2\text{H}_5^+$ ) is inactive with  $\text{pK}_a$  of 8.2.<sup>182</sup> This means that some fraction of dissolved hydrazine in neutral aqueous electrolyte might undergo electrooxidation:



This reaction contributes to more acidic environment and results in protonation of hydrazine, hence, making the reaction self-limiting. This suggests that excessive amount of hydrazine in electrolytes could be the cause of unfavourable equilibrium and pose no beneficial effects for the electrochemistry of full cells. Based on these results, 0.1 mol% of hydrazine was deemed an optimal concentration and chosen for the following investigations in this section.

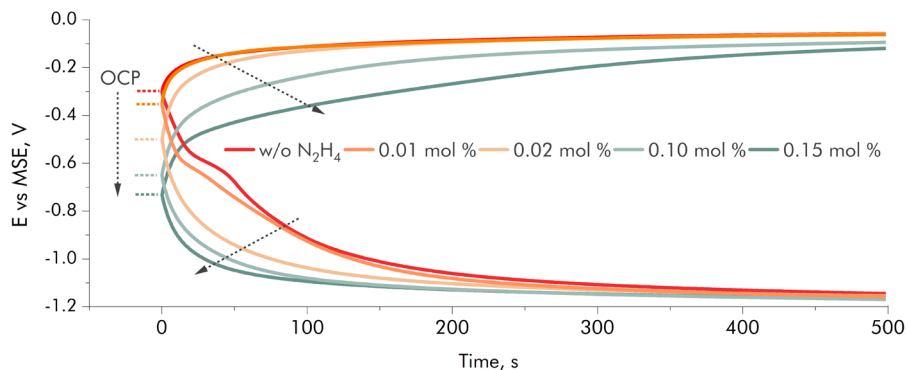


Figure 50. Charging profiles for anode and cathode in symmetric NVTP full cells in the first cycle recorded in 1 M  $\text{Na}_2\text{SO}_4$  (aq) at 1 C rate and different hydrazine concentration.

In this part, hydrazine is employed as a reductive agent in symmetric full NVTP|NVTP cells. For this investigation, symmetric full NVTP cells were assembled with 6 different water-based or hybrid electrolytes. The composition of these electrolytes is summarized in Table 4.

**Table 4.** Nomenclature and composition of electrolytes.

Sample id	S7	S7_HZ	S10	S10_HZ	DMSO	DMSO_HZ
Salt	1 M Na <sub>2</sub> SO <sub>4</sub>	1 M Na <sub>2</sub> SO <sub>4</sub>	1 M Na <sub>2</sub> SO <sub>4</sub>	1M Na <sub>2</sub> SO <sub>4</sub>	1 M NaNO <sub>3</sub>	1 M NaNO <sub>3</sub>
pH	7	7	10	10	-	-
Buffer	-	-	Sodium borate	Sodium borate	-	-
Hydrazine	-	0.1 mol%	-	0.1 mol%	-	0.1 mol%
Co-solvent	-	-	-	-	DMSO 50 mol%	DMSO 50 mol%

The results in Fig. 51 compare GCD performance of samples without hydrazine (a) and with hydrazine (b). Rapid capacity decay during the first cycles for hydrazine-free aqueous electrolytes (Fig. 51 a) is occurring in the absence of excessive capacity in cathode, which could compensate for the charge consumed by parasitic reactions at the anode. The remaining capacities make up only 30% and 9% of initial capacities for samples S7 and S10, respectively. The presence of parasitic reactions is further corroborated by low initial CE in these electrolytes. In case of S10, however, CE remains low throughout all 100 cycles. While increased pH contributed to high and stable coulombic efficiency of NTP electrode in pH investigation (Fig. 35 c), raising pH value in full balanced cells does not prevent capacity decay. As expected, the sample, containing 50 mol% of DMSO showed decent stability (80%) and high CE. This agrees well with the results of previous section, in which benefits of co-solvents were discussed in detail. Interestingly, introducing 0.1 mol% of hydrazine into DMSO electrolyte has brought up capacity retention of the full cell to unprecedented value of 97% (Fig. 51 b). This can be explained by synergetic effect of limited access of oxygen towards the surface of electrode provided by DMSO and less oxygen species due to the reduction by hydrazine. Hydrazine has also substantially improved capacity retention of both S7\_HZ (from 30% to 53%) and S10\_HZ (from 9% to 75%), which confirms successful suppression of ORR and other parasitic reactions. Notably, 0.1 mol% of hydrazine helps to achieve the stability provided by employing 50 mol% of DMSO, emerging as another promising route to design stable and well-performing cells. The rapid growth in coulombic efficiency

values of these samples speak further in favour of using oxygen scavenging agents.

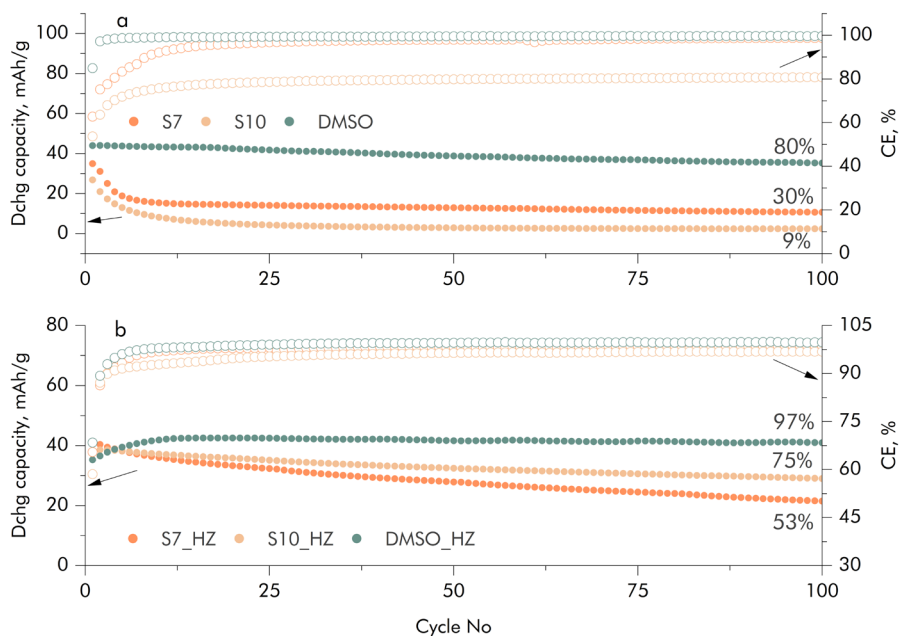
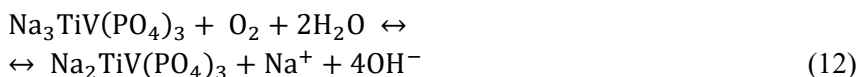


Figure 51. GCD cycling of symmetric NVTP full cell in (a) hydrazine-free and (b) hydrazine-containing electrolytes.

NVTP as well as NTP suffers from oxygen reduction reaction leading to self-discharge in aqueous electrolytes. The reaction occurring between NVTP and oxygen can be written as:



In this study the process of self-discharge in symmetric NVTP capacity balanced cells is investigated. The cells, in which investigation is performed are considered to be airtight and all used electrolytes were naturally aerated. It is noteworthy, that no additional precautions were taken to prevent oxygen access to the cell during measurements. The cells were charged to 1.3 V at 1C rate and left at open circuit conditions to monitor the changes in the voltage which are presented in Fig. 52. The results indicate that the addition of 0.1 mol% of hydrazine in electrolytes has positive effect on the duration of self-discharge of all samples. In case of S\_7 (Fig. 52 a) self-discharge time almost doubled with the introduction of reductive agent (from 5 h to 9 h). The

buffering of electrolyte at pH = 10 had a similar effect (Fig. 52 b). However, the addition of hydrazine resulted in more than double increase in the time cell remained charged (from 9 h to 24 h). Due to restricted water activity in DMSO containing sample, the self-discharge time was much longer (155 h) indicating effective suppression of parasitic reactions (Fig. 52 c). Additional hydrazine contributed to further increase in charged state stability (~200 h), which explains the outstanding GCD performance results of this sample. Concluding, the benefits of reductive agent for the overall electrochemical performance are evident.

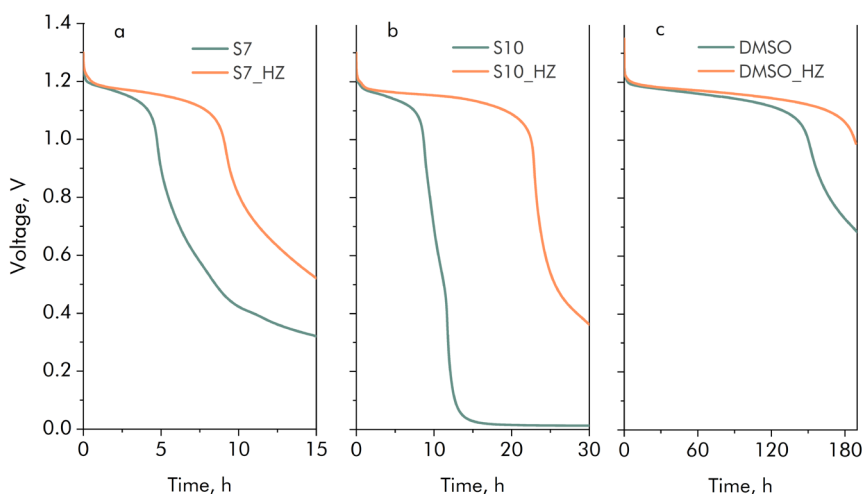


Figure 52. Self-discharge profiles of symmetric NVTP full cells in different electrolytes.

### 3.2.3. Organic solvent-based electrolytes

Organic electrolytes are free from oxygen and hydrogen evolution reactions; hence, they can operate over a broader voltage range compared to aqueous electrolytes.<sup>183</sup> This wider electrochemical stability window allows for higher energy densities in batteries making organic electrolytes suitable for applications requiring compact and lightweight energy storage solutions. Additionally, many high-energy electrode materials, such as lithium and sodium, are more stable and/or perform better with organic electrolytes.<sup>184</sup> These benefits served as a motivation to characterize electrodes in water-free environments not plagued by the parasitic reactions brought by water to reveal the full potential of the electrodes.

Initially, electrochemical performance of NTP-based anode was investigated in conventional 1 M NaPF<sub>6</sub> in propylene carbonate (PC) against

sodium metal (Fig. 53). A good cycling stability is observed when electrode is cycled in the typical voltage range for aqueous electrolyte (92%); however, when one more redox plateau is allowed by decomposition-resistant electrolyte the stability is not so great (62%). Initial capacities are reaching 89% and 80% of theoretical capacities, accordingly.

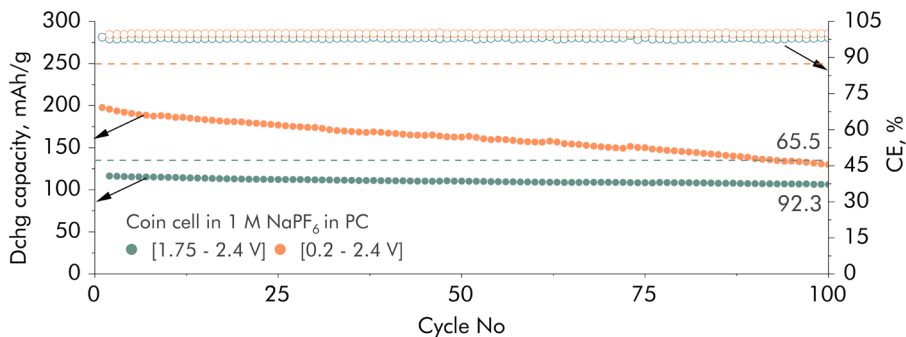


Figure 53. GCD cycling performance of NTP electrode in 1 M NaPF<sub>6</sub>.

Charge-discharge curves in Fig. 54 a-b show presence of all expected plateaus for both samples. There are indications of some irreversible process occurring during discharge (the disappearing feature at 2.1 V). Additionally, electrolyte decomposition propelled formation of solid electrolyte interphase (SEI) layer resulted in polarization and redox potential shifts visible for both samples.

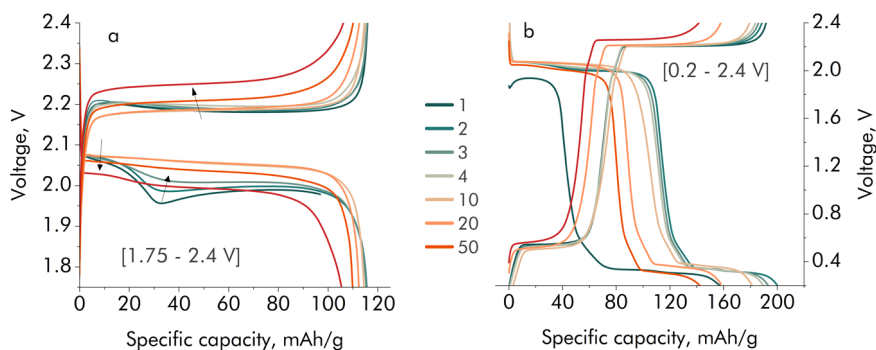


Figure 54. Voltage profiles of GCD cycling in the ranges (a) [1.75 – 2.4 V] and (b) [0.2 – 2.4 V] vs Na/Na<sup>+</sup>.

Characterization in another common salt - NaTFSI - resulted in extraordinary cycling stability of 100% (Fig. 55) for [1.75 – 2.4 V] cycling range, but lower initial capacity of 89 mAh/g. However, such stability was

absent at the extended cut-off and capacity retention barely reached 62% and the initial capacity was 183 mAh/g.

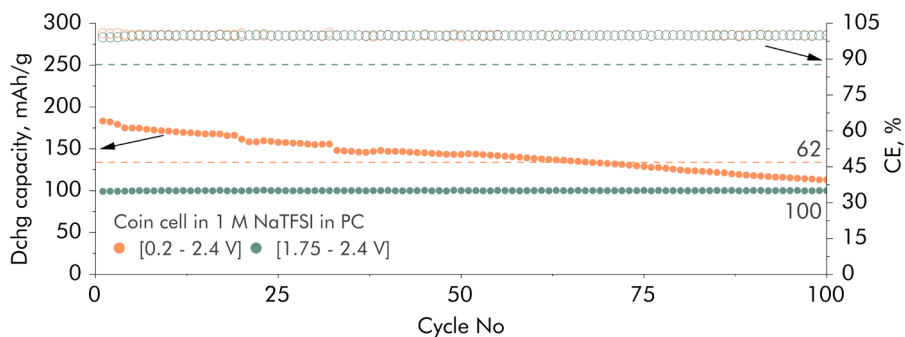


Figure 55. GCD cycling performance of NTP electrode in 1 M NaTFSI.

Voltage curves of GCD cycling are presented in Fig. 56. Interestingly, minimal potential drift is observed in Fig. 56 a, indicating the presence of phenomenon other than SEI formation directly affecting the initial capacity of the electrode.<sup>185</sup> Both plateaus of extended cycling range, peculiarly, seem to shrink as the GCD progresses. This might be attributed to the loss of contact due to chaotic SEI formation or irreversible changes brought by cycling at higher voltages.

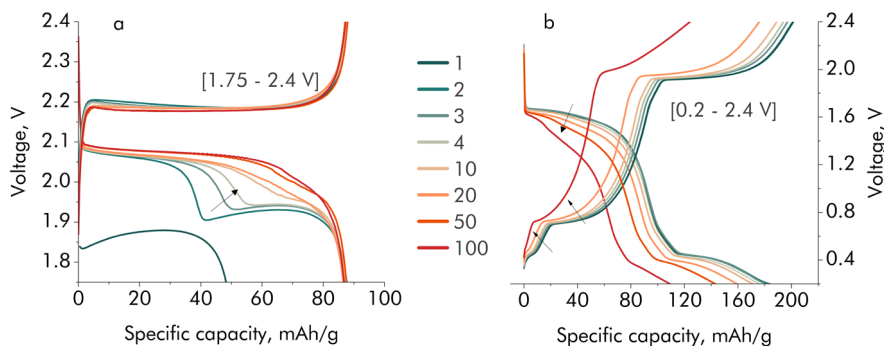


Figure 56. Voltage profiles of GCD cycling in the ranges (a) [1.75 – 2.4 V] and (b) [0.2 – 2.4 V] vs Na/Na<sup>+</sup>.

In OSIBs, electrolyte additives are used to control the degradation of electrolyte and formation of SEI. Two commonly utilized electrolyte additives are 1,3-propane sultone (PS) and fluoroethylene carbonate (FEC) which act as stable SEI promoters.<sup>186,187</sup> Stable SEI bears several benefits for the system: prevents continuous electrolyte decomposition, reduces unwanted side



reactions, reduces gas evolution and promotes safety and stability of the battery.<sup>188</sup>

5 vol% of each additive were added into 1 M NaPF<sub>6</sub> and 1 M NaTFSI in order to investigate if it would improve electrochemical performance. In case of NaPF<sub>6</sub> (Fig. 57), introducing FEC had virtually no effect on initial capacity (approx. 120 mAh/g) or capacity retention. Addition of PS, however, contributed to rapid capacity fade, most probably, due to the reaction between the additive and the active material.

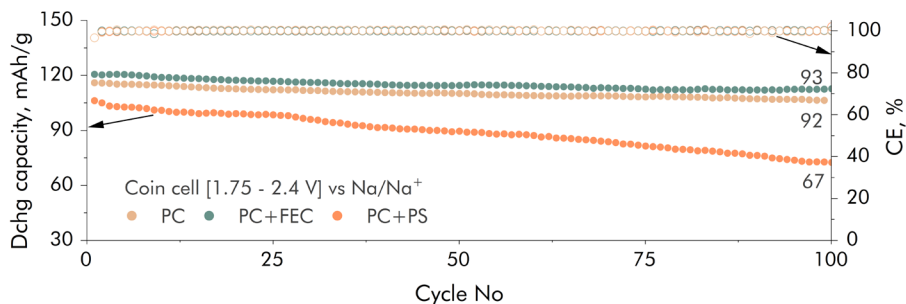


Figure 57. GCD cycling in 1 M NaPF<sub>6</sub> organic electrolytes.

Similarly to the study of NaPF<sub>6</sub>, NaTFSI based electrolytes (Fig. 58) showed best initial capacity with FEC or PS as an additive (~120 mAh/g) or without any additives at all. Pure PC, however, showed excellent stability of 100% upon cycling. In terms of capacity retention, FEC also performed pretty well (96%), but PS-containing electrolyte showed steady decay of capacity, loosing around 23% of initial capacity in 100 cycles.

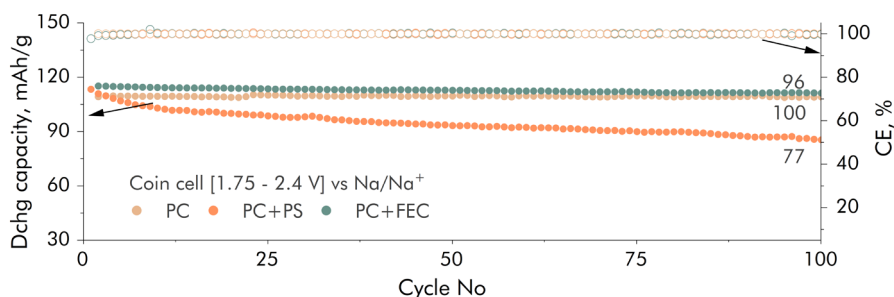


Figure 58. GCD cycling in 1 M NaTFSI organic electrolytes.

This investigation indicates, that, although organic electrolytes are less problematic in terms of parasitic reactions, aqueous electrolytes can reach

similar and, sometimes, even better results with right manipulations, which further underlines their potential in stationary energy storage applications.

### 3.2.4. Summary

In this part of the work, water-based electrolytes for aqueous sodium-ion battery cells were prepared and characterized in great detail. The obtained results are summarized as:

- Chemical oxygen reduction reaction catalyzed by  $\text{Ti}^{+3}$  present in the charged state  $\text{Na}_3\text{Ti}_2(\text{PO}_4)_3$  is identified as the main parasitic reaction responsible for self-discharge and pH increase in aqueous electrolyte solutions. Hydrogen evolution is also important, especially at low  $\text{O}_2$  concentrations and C-rates. The removal of oxygen and pH buffering are beneficial for the capacity retention of  $\text{NaTi}_2(\text{PO}_4)_3$  electrodes during cycling. Acidic environment (pH = 4) results in decent capacity retention but low Coulombic efficiency. Neutral environment (pH = 7) results in excellent capacity retention but reduced Coulombic efficiency. Alkaline environment (pH = 10) is good for suppressing hydrogen evolution and high Coulombic efficiency but low capacity retention.
- Alkaline environment is shown to be the main cause of degradation for  $\text{NaTi}_2(\text{PO}_4)_3$  electrodes resulting in capacity loss. The EDX, XRD, and NMR analyses show that capacity loss is not directly related to Ti dissolution into the electrolyte. The results suggest that capacity loss in  $\text{NaTi}_2(\text{PO}_4)_3$  electrodes is mainly caused by the formation of insoluble Ti-rich interphase which blocks the electrochemical reaction.
- The implementation of organic co-solvents such as glycerol and DMSO results in significant rearrangement of the hydrogen bond network in aqueous systems reducing relative water activity. The electrolytes with organic co-solvent show decent conductivities and salt solubility. The reduction of water activity results in significantly wider electrochemical stability window. This suppresses the parasitic reactions such as hydrogen and oxygen evolution resulting in longer self-discharge times and significantly better capacity retention of  $\text{NaTi}_2(\text{PO}_4)_3$  electrodes during cycling.
- Full cells containing  $\text{NaTi}_2(\text{PO}_4)_3$  and  $\text{Na}_{1.86}\text{Fe}[\text{Fe}(\text{CN})_6] \cdot 2.28\text{H}_2\text{O}$  Prussian Blue Analog also benefited from the addition of co-solvents. The results show that wider cycling voltage windows and significantly better capacity retention is achieved in such electrolytes.

- The introduction of small amounts of reductive agents such as hydrazine into aqueous electrolytes was shown to effectively scavenge oxygen and suppress parasitic reactions such as oxygen reduction. This procedure allowed to prepare capacity balanced (N/P=1)  $\text{Na}_2\text{VTi}(\text{PO}_4)_3$ – $\text{Na}_2\text{VTi}(\text{PO}_4)_3$  full cells with good capacity retention.
- The use of completely organic electrolyte solutions with much wider electrochemical stability window enables to achieve the full charge capacity of  $\text{NaTi}_2(\text{PO}_4)_3$  electrodes reaching the  $\text{Ti}^{3+}/\text{Ti}^{2+}$  redox. However, the obtained cycling stability are similar to the best results obtained using fully optimized aqueous-based electrolytes.

### 3.3. Electrode composite binders for aqueous batteries

The primary function of an electrode binder is to provide cohesion between the active materials and carbon additive and adhesion of the electrode to the current collector. Typically, polymeric binders bear no additional electrochemical benefits for the electrode. Typical binders are polymeric, and represent one of the major components of an electrode. It has been shown that binders affect the processes of ageing and irreversible capacity loss in batteries.<sup>189–191</sup> Some of the major reasons for the rapid degradation of an electrode is poor interconnectivity, self-agglomeration of active materials and delamination of electrode components from the current collector. The discovery and development of an optimal electrode binding materials appears to be a challenging task as there is an impressive list of requirements for a potential binder. Among the properties that have to be taken into consideration are: solubility in safe solvents and no or minimal swelling after curing, electrochemical stability, moderate flexibility, good binding properties at high solid contents, and, in perfect scenario, adhesion to metal substrates in non-aqueous media.<sup>191</sup>

The binding as a function of polymer arises from either chemical (direct binding) or physical (indirect binding) interactions (Fig. 59). In direct or covalent binding strong adsorption of polymeric matrix onto the active material takes place. The interparticle bridges are created by reactive functional groups such as hydroxy (-OH), carboxy (-COOH) groups which are attached to the polymer backbone. Indirect binding occurs in the absence of functional groups through mechanical/physical adsorption on the surface of active materials. In this case binder initially forms a network and then captures the material particles in it.<sup>192</sup> Both binding strategies have been successfully implemented in LIBs and SIBs; however, the covalent binding has not been widely studied in aqueous media. In this work both covalent and noncovalent binders are studied in NTP-based negative electrode in aqueous electrolytes.

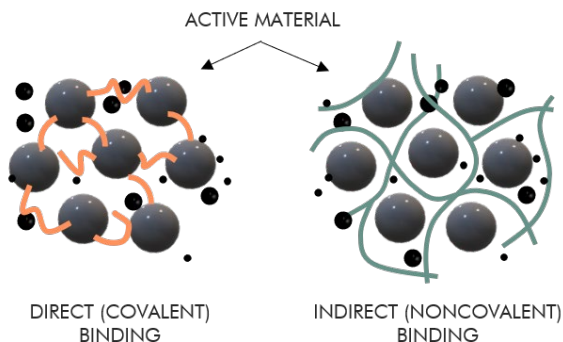
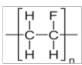
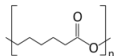
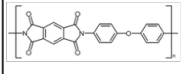
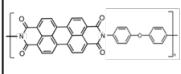
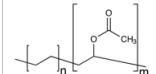


Figure 59. Schematic representation of different binding mechanisms.

### 3.3.1. Indirect (noncovalent) binders

As a rule, the concentration of functional groups and the presence of side chains/branches are major contributors to the binding ability. Hence, indirect binding requires a comparatively larger amount of binder to achieve the levels of adhesion similar to that of direct binding, which is attributed to the necessity to form a strong inert network of polymer which creates structural integrity by immobilizing conductive carbon and active material.<sup>193</sup> Nonetheless, some of the most widely used binders are PTFE and PVDF - exceptionally unreactive polymers. While it might be considered a drawback, no reactive functional groups ensure minimal/no swelling in aqueous electrolytes. Table 5 summarizes indirect binders which were tested in NTP electrodes. In this chapter we focus on indirect binders that satisfy at least some of the requirements for the polymers in aqueous batteries: polyvinylidene fluoride, polyimides, and ethylene-co-vinyl-acetate copolymer.

**Table 5.** Indirect polymeric binders tested in NTP electrodes.

Binder	Structure	Solvent	Binding	Adhesion to metal in water	Adhesion to metal upon cycling	Remarks
Polyvinylidene fluoride		Toluene	+	-	-	Very brittle, cracks on the drying stage
Polycaprolactone		Toluene	-			Very brittle, cracks on the drying stage
Poly(pyromellitic dianhydride-4,4'-oxydianiline)		NMP	+	+	-	Film is difficult to transfer onto mesh.
Poly(naphthalene-tetracarboxylic dianhydride-4,4'-oxydianiline)		NMP	+			Very brittle
Poly(ethylene-vinyl acetate)		Hot toluene	+	+	+	Complicated electrode preparation

#### Polyvinylidene fluoride

Currently, most state-of-the-art aqueous battery electrodes are processed using fluorine-containing polyvinylidene fluoride (PVDF) with structural

formula presented in Table 5. Despite the undeniable advantages such as great mechanical properties, oxidation-reduction resistance, this market-dominating binder is associated with a number of safety and environmental red flags. The most concerns arise due to organic solvents such as toxic *N*-methyl-2-pyrrolidone (NMP) being present in slurry formulations.<sup>73</sup> This, once again, emphasises that switching to alternative binders might be required in the future in order to smoothly transition research advances into manufacturing lines.

Apart from the environmental issues, PVDF is also troubled by a major drawback - lack of adhesion to the metal substrate in aqueous media. This, consequently, introduces an additional step of mechanical transfer onto stainless steel mesh. All additional manipulations with the electrodes contribute to the overall cost of production, hence, should be avoided. The adhesive strength between the coating and the substrate can be increased by: mechanically altering the substrate, introducing new polar interactions with the bonding agent or establishing new chemical bonds with the help of an adhesion promoter.<sup>194</sup> The use of adhesion promoters is, probably, the most versatile technique to achieve increased adhesion, as they can both enhance the bonding strength either through chemical reactions with the phases present or through altering the critical surface tension. The literature review on the topic revealed a promising family of coupling agents able to withstand the attack of water on the adhesive bond and prevent the delamination. Organosilanes are frequently used as adhesion promoters for paints, inks, coatings, and adhesives. These chemicals, characterized by a general structure of four substituents attached to a single silicon atom, act as the bonding/bridging agents in the interphases between organic and inorganic substrates to ensure better adhesion between two dissimilar components.<sup>195</sup> Typically, silicon-based adhesion promoters have one organic group and three inorganic-reactive alkoxy groups, which hydrolyze to silanols in presence of residual moisture on the surface of inorganic component. Subsequently, the coordination with metal -OH groups occurs to form an oxane bond with elimination of water (Fig. 60).<sup>196</sup>

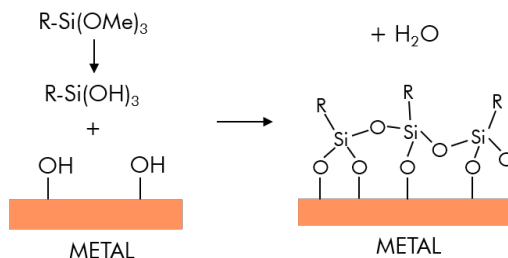


Figure 60. Scheme of silane bonding to inorganic surfaces.

Depending on the chemical reactivity in the polymeric component, matching reactivity of the silane can be adjusted by choosing an appropriate coupling agent. In cases when polymer exhibits no reactivity (e.g. PVDF) the bonding to the polymer becomes challenging. Peculiarly, improved adhesion is still observed for such polymers. Enhanced bonding is best explained by interdiffusion of the binder into the siloxane matrix and formation of interpenetrated network (IPN) at the interphase area.<sup>197</sup> The condensation of silanols results in a multimolecular structure of crosslinked siloxane on the inorganic substrate. The structure is dense in proximity to the surface and becomes more diffused as the distance to the surface is increased (Fig. 61). The formed grid allows polymers to diffuse into the structure where strengthening of the bonding takes place through physical and/or electrostatic effects. In the following investigation, 6 different adhesion promoters from silane family were added to the standard formulation with PVDF polymer (Table 7).

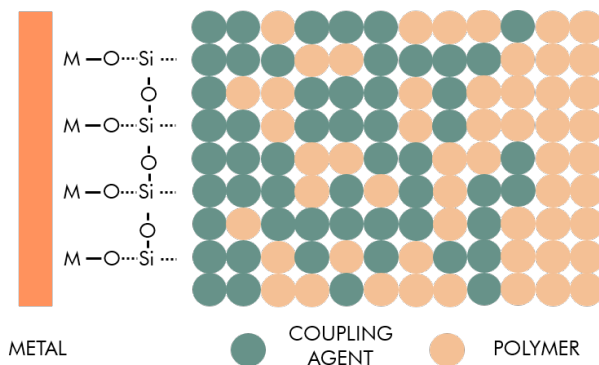
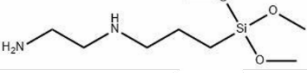
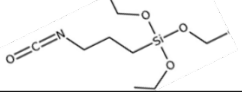
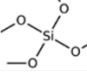
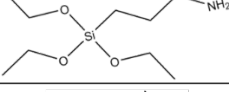
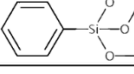
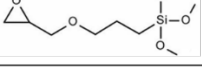


Figure 61. IPN formed between silanes and polymers.

Initially, dry and wet peeling tests were performed to evaluate the effect of additives. Dry peeling test was carried out immediately after casting a film on a stainless-steel foil, and wet peeling test was performed after 24 h and 168 h of soaking the electrodes in water and subsequent 5 min sonification. The results are summarized in Table 6. AP1 and AP5 did not pass neither dry nor wet peeling tests both at lower (1 wt%) and higher (5 wt%) contents of coupling agents. Given the non-reactive nature of PVDF, one can assume that the organic ligands did not form an efficient network to enhance adhesion. Similar situation is observed with AP3. In this case, however, bad adhesion can be explained by the absence of organic functional group, which is

supposed to participate in IPN network, however, has 4 groups capable of bonding to the inorganic substrate.

**Table 6.** Silanes used as adhesion promoters and results of the initial investigation.

Silane	Structural formula	Wt %	Dry peel	Wet peel 24 h	Wet peel 168 h
<u>N-[3-(Trimethoxysilyl)propyl] ethylenediamine (AP1)</u>		1%	-	-	-
		5%	-	-	-
<u>3-(Triethoxysilyl)propyl isocyanate (AP2)</u>		1%	+	+/-	+/-
		5%	+	+	+
<u>Tetramethyl orthosilicate (AP3)</u>		1%	-	-	-
		5%	+	-	-
<u>(3-Aminopropyl) triethoxysilane (AP4)</u>		1%	+/-	+/-	+/-
		5%	+	+	+
<u>Trimethoxyphenylsilane (AP5)</u>		1%	-	-	-
		5%	-	-	-
<u>[3- (2,3-Epoxypropoxy)-propyl]-trimethoxysilane (AP6)</u>		1%	+	+	+
		5%	+	+	+

The electrodes with silanes that passed the wet peeling test were prepared for electrochemical characterization. GCD cycling was performed for both electrodes transferred onto stainless steel mesh and those casted directly onto stainless steel foil. The cycling with mesh as a substrate (Fig. 62) showed lower initial capacities for the samples AP2, AP4, AP6 with adhesion promoters (77, 70, 63 mAh/g) than for the sample with just PVDF (91 mAh/g). The addition of coupling agents has also negatively influenced the capacity retention after 100 cycles (from 80% o 56/64/76%). These findings might suggest that some of the coupling agent binds to the surface of inorganic active material and somehow hinders the transport of charged species to the particles of active material. Another possible explanation could be increased resistance due to the formation of insulating film on the surface of NTP. The overall GCD performance on mesh is, however, comparable with that of samples with insufficient carbon coating.



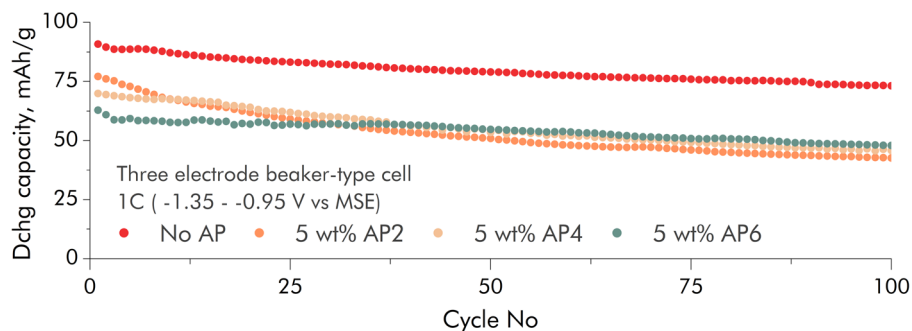


Figure 62. GCD cycling performance of NTP-based electrodes with different adhesion promoters on a stainless-steel mesh.

When the same experiment is performed with samples on stainless steel foil (Fig. 63), all three samples show at least some capacity, compared to the pure PVDF containing sample, which delaminated from the current collector even before the first GCD cycle. This indicates an improvement in adhesion to the current collector. The initial capacity was similar for AP4 sample (69 mAh/g), however, AP2 and AP6 showed much lower initial capacities (49 mAh/g and 35 mAh/g) than the same sample on mesh. Rapid capacity decay was observed for AP4 and AP6 samples and a steady loss of capacity was recorded for AP2 sample. *Post mortem* investigation of the electrodes revealed that none of them remained fully attached to the surface of current collectors. It is unclear if the degree of delamination directly correlated with the remaining capacity after 100 cycles, but delamination itself is definitely responsible for the initial rapid capacity decay which was not recorded for samples on mesh. The best performing sample, AP2 must have undergone the major part of delamination on the resting stage, when electrode was submerged in aqueous electrolyte for two hours, and remained quite stable for the rest of investigation. These results suggest that whilst silanes stay adhered to inorganic substrates in the presence of moisture, the conditions of electrolyte-flooded cell might be too extreme for them. Increasing the content of adhesion promoters does not seem a viable solution as addition of 5 wt% of binder already contributed to initial capacity loss, which is most probably related to the formation of insulating surface film.

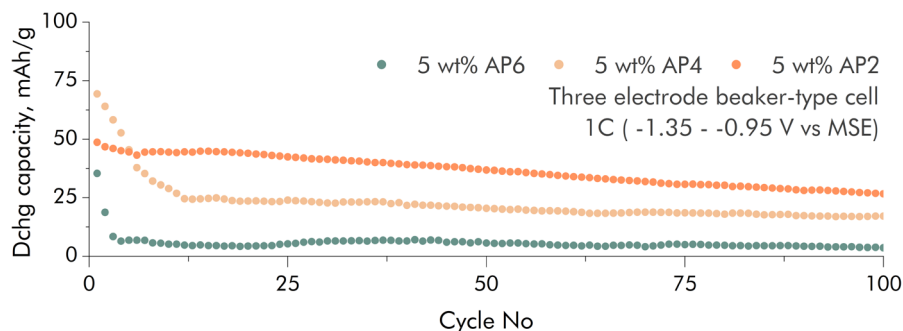


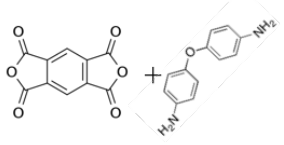
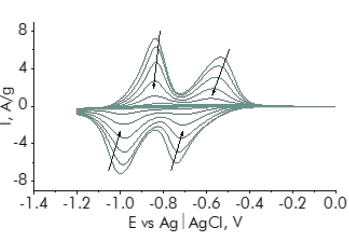
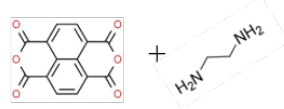
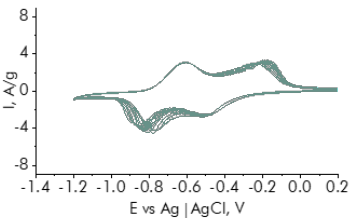
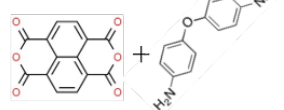
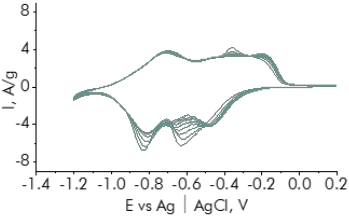
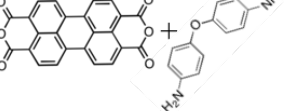
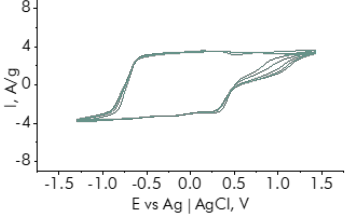
Figure 63. GCD cycling performance of NTP-based electrodes with different adhesion promoters on (a) stainless steel mesh and (b) stainless steel foil at 1C rate in 1 M Na<sub>2</sub>SO<sub>4</sub> (aq).

### Polyimides

Electrochemically active polymers and other organic compounds are often employed as active materials in Na-ion batteries. Polyimides, characterized by high density of electroactive functional groups, have emerged as a promising electrode material for rechargeable batteries.<sup>198</sup> Exceptional thermal stability ensures the stable structure even at fluctuating temperatures – one of the critical aspects for battery operation.<sup>199</sup> Moreover, polyimides have presented great chemical resistance, which allows for longevity and robustness in different environments such as battery electrolytes. Their adhesive properties make them potentially suitable for the role as binders, which would not be considered a deadweight, but rather contribute to the overall electrochemical performance of the battery.<sup>200</sup>

It is important to note, though, that the final polyimides are solid and mostly insoluble, hence, can only be used as binders in a form of dispersions. The intermediate synthesis products, however, can be liquid and suitable for this role. For the initial investigation, 4 different polyimides with redox potentials lying in the same range as NTP materials were synthesized and their electrochemical redox potential as well as stability in 1 M Na<sub>2</sub>SO<sub>4</sub> were evaluated using cyclic voltammetry. Synthesis parameters and initial electrochemical analysis results are summarized in Table 7.

**Table 7.** Synthesized polyimides and results of the initial investigation.

Polyimide and precursors	Cyclic voltammogram	Remarks
<p>Poly(4,4'-oxydiphenylene pyromellitimide)</p> 		<ul style="list-style-type: none"> <li>• Liquid phase</li> <li>• Liquid phase has adhesion to metal <ul style="list-style-type: none"> <li>• Not electrochemically stable</li> </ul> </li> </ul>
<p>1,4,5,8-naphthalenetetracarboxylic dianhydride-derived polyimide</p> 		<ul style="list-style-type: none"> <li>• No liquid phase</li> <li>• Electrochemically stable</li> </ul>
<p>1,4,5,8-naphthalenetetracarboxylic dianhydride-derived polyimide</p> 		<ul style="list-style-type: none"> <li>• No liquid phase</li> <li>• Electrochemically stable</li> </ul>
<p>Perylene-3,4,9,10-tetracarboxylic dianhydride-derived polyimide</p> 		<ul style="list-style-type: none"> <li>• Liquid phase</li> <li>• Liquid phase has poor adhesion to metal <ul style="list-style-type: none"> <li>• Not electrochemically stable</li> </ul> </li> </ul>

The results presented in Table 8 indicate that only poly(4,4'-oxydiphenylene pyromellitimide) commercially known as Kapton (Fig. 64) has both liquid phase stage during synthesis and good adhesion to the metal current collector.

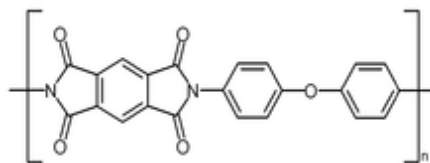


Figure 64. Structural formula of Kapton.

Electrodes with Kapton were prepared for GCD cycling investigation. In a standard formulation, with the polymer making up 10 wt% of the total electrode mass, Kapton did not exhibit the same adhesion to metal substrate as the pure Kapton film, hence, electrodes with 20 wt% of Kapton and 60 wt% of active material were also prepared. Increasing the amount of binder twice did not significantly improve adhesive properties. Both electrodes were transferred onto mesh in order to investigate their GCD performance (Fig. 65). The initial rapid capacity loss can be explained by electrochemical instability of Kapton in water revealed by CV. The GCD profiles indicate, that despite not providing desired adhesion, higher amount of binder contributed to increased initial capacity of the sample (66 vs. 95 mAh/g). This could be explained by the binding abilities of the polymer – no long aliphatic branches, which create active material-capturing networks, are present, hence, the binding capabilities are weaker comparing to the PVDF. Insufficient binding might result in poorer electrode integrity and contact leading to lower initial capacity of the electrode. The sample with 20 wt% Kapton exhibits cycling stability inferior to PVDF (54 wt% vs. 79 wt%), it also comes with no adhesion to metal in formulation, complicated preparation procedure, decreased active material loading in the battery, hence, cannot be considered a viable competitor to PVDF.

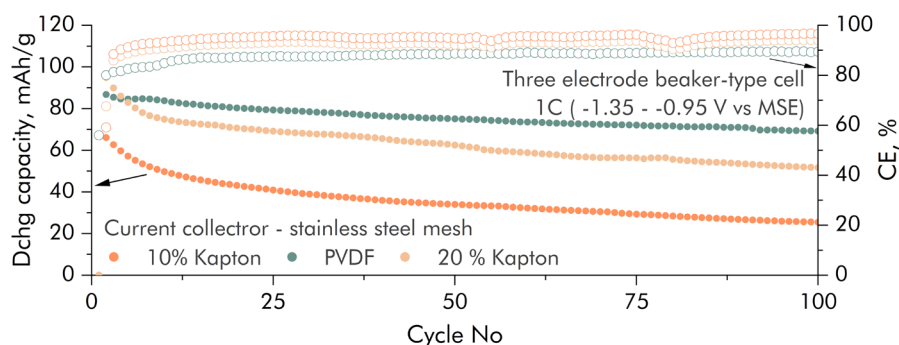


Figure 65. GCD cycling performance of NTP-based electrodes with different binders at 1C rate in 1 M Na<sub>2</sub>SO<sub>4</sub> (aq).

## Poly(ethylene-co-vinyl acetate)

Poly(ethylene-co-vinyl acetate) (PEVA) copolymer with structural formula presented in Table 5 has been successfully used in hot-melt adhesives (HMAs).<sup>201</sup> HMAs are a class of thermoplastic solids, which can be spread onto substrates in their melted form at elevated temperatures and quickly solidify upon cooling.<sup>202</sup> The unit structure of PEVA copolymers is comprised of stiff and partially crystalline polyethylene domains, and flexible, soft vinyl acetate. Generally, the adhesive properties of these copolymers are determined by their vinyl acetate content. PEVA copolymer with 18% of vinyl acetate are not limited to applications in hot-melts. They can be dissolved in certain solvents (e.g. toluene) at elevated temperatures and potentially employed as binders with great adhesive properties.

For this investigation electrode was prepared by a modified procedure: active material and carbon were dispersed in PEVA solution obtained by mixing PEVA granules in toluene at 60 °C. Hot dispersion was casted directly onto stainless steel foil. Evaporation of solvent yielded a flexible and durable electrode. It is obvious from the GCD cycling results presented in Fig. 66, that PEVA-containing electrode exhibits superior capacity retention (86%) compared to PVDF (21%). This confirms excellent adhesion of the electrode to the current collector during cycling. Lower initial capacity (80 mAh/g) might be attributed to imperfect preparational procedure: the mixing at elevated temperatures could not be carried out in planetary ball-mill. Mixing by magnetic stirrer could result in a less homogeneity of slurry than desired. It is also possible that PEVA formed an insulating film on the surface of the active material. However, with given cycling stability, lower initial capacity does not outweigh the obvious advantages of great adhesion.

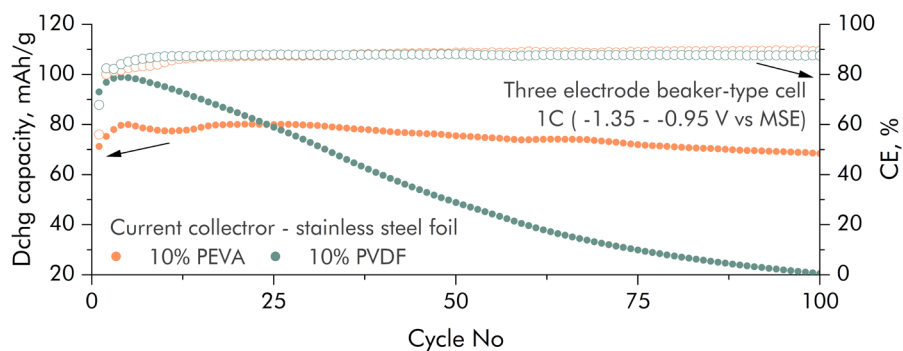
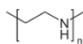
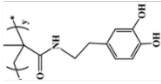
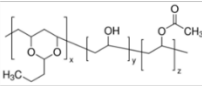
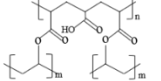
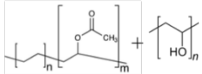
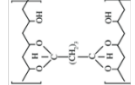
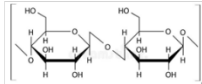
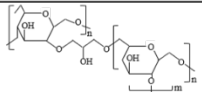


Figure 66. GCD cycling performance of NTP-based electrodes with PVDF and PEVA binders on stainless steel foil at 1C rate in 1 M Na<sub>2</sub>SO<sub>4</sub> (aq).

### 3.3.2. Direct binders

The popularity of direct binders in organic electrolytes arises from the reactive functional groups present at the backbone of these polymers. Reactive groups such as -OH or -NH<sub>2</sub> tend to form bonds with appropriate surface groups of inorganic materials and ensure excellent cohesion within the electrode. Moreover, they are readily available as aqueous solutions or dispersions, elevating preparational procedure to the new level of safety.<sup>203</sup> Unfortunately, the functional groups that are responsible for both good adhesion and cohesion are the same groups that are promoting swelling in water which is the main component of aqueous electrolytes. Once swelling reaches a certain threshold, substantial changes in the volume of the electrode will occur, resulting in electrode deformation and cracking during cycling. Subsequently, battery lifespan is reduced due to the loss of contact or release of active components into the electrolytes.<sup>204–206</sup> Swelling, in theory, can be overcome by crosslinking. However, swelling reduction often comes at the expense of adhesive properties. In this study, we investigated several direct binders for the NTP electrodes. Table 9 summarizes the results of initial investigation. Polyethyleneimine and poly(dopamine methacrylamide) did not form even and uniform coatings with good integrity. Cellulose formed a film with subpar homogeneity, showed substantial swelling even after crosslinking with glutaraldehyde. PEVA dispersion with polyvinyl alcohol as emulsifier also exhibited excessive swelling, which was not sufficiently improved by crosslinking. Notably, the binders that exhibited adhesion to metal current collector in water did not retain the same adhesion to the stainless steel upon cycling. The electrolyte investigation has revealed dramatic changes in pH of the electrolyte upon GCD cycling: the rise of pH was recorded for the unbuffered electrolytes in the first 20 cycles. It is highly probable, that basic solutions negatively affect the adhesive properties of the binders. In the following section we will focus on direct binders that showed none or moderate swelling, that is poly(vinyl butyral-co-vinyl alcohol-co-vinyl acetate) and poly(vinyl alcohol-acrylic acid) copolymers.

**Table 8.** Direct polymeric binders for the NTP electrodes tested in this work.

Binder	Structure	Solvent	Swells	Adhesion to metal in water	Adhesion to metal upon cycling	Remarks
Polyethyleneimine		Water, EtOH				Very brittle, cracks on the drying stage
Poly(dopamine methacrylamide)		NMP				Low solution viscosity, poor dispersion
Poly(Vinyl Butyral-co-Vinyl Alcohol-co-Vinyl Acetate)		NMP, IPA	-	+	-	Film is difficult to transfer onto mesh.
Polyvinyl acetate – polyacrylic acid Ratio 4:1		Water	+	+	-	Very brittle
EVA dispersion. Emulsifying agent - PVA		Water	+	+	-	Good elasticity
EVA dispersion (PVA). Crosslinked		Water	less	-	-	Good elasticity
Cellulose nanocrystals		Water	+	-	-	Brittle film is formed
Cellulose nanocrystal. Crosslinked		Water	less	-	-	Brittle film is formed

### Poly(vinyl butyral-co-vinyl alcohol-co-vinyl acetate)

Poly(vinyl butyral-co-vinyl alcohol-co-vinyl acetate) or PVBA (structural formula is present in Table 8) has been widely employed in the anticorrosive applications.<sup>207</sup> The functional groups of this copolymer chain are responsible for its adsorption properties on various substrates through covalent and/or hydrogen bonding. PVBA has shown to work well as a protective coating in saline environments, which in terms of composition are not that different from the standard electrolytes used in the investigation of NTP electrodes. Hence, it was assumed that this binder could be suitable for the role of binder for aqueous batteries. One undeniable advantage of this copolymer is solubility in isopropanol – a solvent much cheaper and less toxic than NMP.

Despite great initial adhesion to the metal substrate, PVBA-containing electrodes rapidly delaminated from the surface of stainless-steel foil upon cycling. Nevertheless, electrode was transferred onto stainless steel mesh and compared to PVDF through GCD cycling (Fig. 67). The results of the investigation indicate that both samples had very similar initial capacities of 87 and 89 mAh/g for PVDF and PVBA, respectively. Cycling stability revealed slight superiority of PVDF (79%) over PVBA (67%). This could be attributed to the overall tendency of reactive groups to interact with water and swell, which leads to the loss of contact.

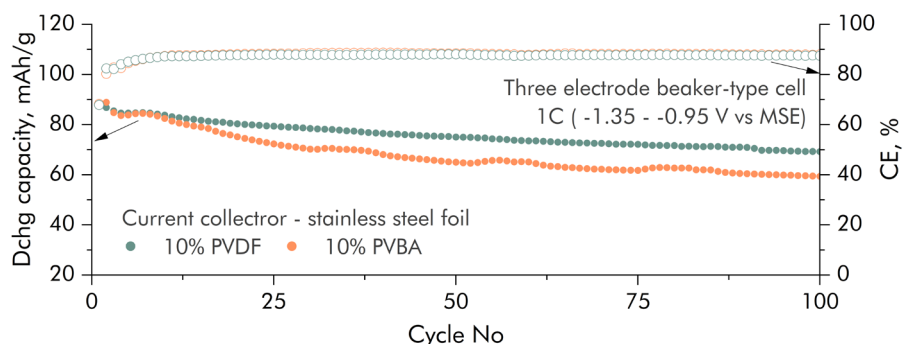


Figure 67. GCD cycling performance of NTP-based electrodes with PVDF and PVBA binders at 1C rate in 1 M Na<sub>2</sub>SO<sub>4</sub> (aq).

Additional investigation revealed that 1000  $\mu\text{m}$  thickness electrode can be casted and dried without cracking, whereas, 300  $\mu\text{m}$  slurry coating was determined as a critical threshold for obtaining crack-free electrodes with good integrity for PVDF. Generally, higher mass loadings are desired for the electrodes and PVBA-based electrodes can provide higher mass loading due to better binding capabilities arising from reactive functional groups. Electrode thickness plays a significant role on the energy density of the electrode since thicker electrodes can reduce the fraction of electrochemically inactive materials such as current collectors and separators.<sup>208</sup> This feature paired up with less toxic solvent, makes PVBA a promising candidate to replace PVDF in ASIBs.

### Poly(vinyl alcohol-acrylic acid)

Poly(vinyl alcohol) (PVA) and poly(acrylic acid) (PAA) – the components of poly(vinyl alcohol-acrylic acid) – are well known for their use in polymer binders owing to their excellent binding strength between electrode materials and current collectors.<sup>209–211</sup> Poly(vinyl alcohol-acrylic acid) (PVA-PAA) has



also previously been reported as a water-soluble binder for silicon anodes and lithium iron phosphate cathodes in LIBs.<sup>212</sup> This blend is capable of building a stable network through hydrogen bonding which contributes to the significantly enhanced adhesion and strength of electrodes.<sup>213</sup> This binder contains carboxylic and hydroxyl functional groups and can be thermally cross-linked in order to improve the mechanical properties. Partial neutralization of PAA can be performed in order to achieve a stronger interconnection between the functional groups and more branched structure of the polymer upon crosslinking.

For this investigation, PVA-PAA copolymer with a mass ratio of 4:1 was prepared by thermal crosslinking. Partial (10%) neutralization of the PAA has been carried out prior to crosslinking. Electrodes with this copolymer as a binder were prepared via standard procedure. Similarly to the PVBA, this binder showed adhesion in water, but delaminated from the metallic substrate during the first cycles. In order to investigate the binding properties of the PVA-PAA, the electrode was transferred onto stainless steel mesh and compared to PVDF through GCD investigation (Fig. 68). The results indicate faster degradation for the PVA-PAA sample – the capacity retention was 61% after 100 cycles. In literature it has been found that PVA-PAA rearranges its network with accordance to the pH and ionic strength of the solution.<sup>214</sup> Higher pH values have shown to induce swelling, hence, lower capacity and capacity stability upon cycling. Buffering electrolyte at acidic values would improve the binder stability, however, as electrolyte investigation shows, is not favourable for the active material. Potentially, co-solvent electrolytes could decrease water activity and alleviate the effects of swelling.

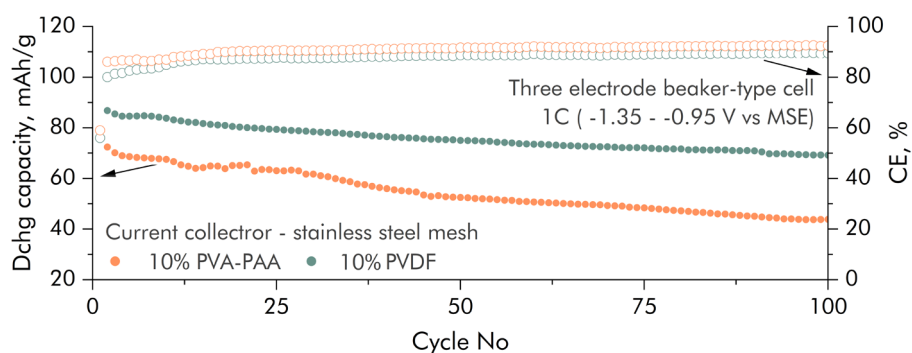


Figure 68. GCD cycling performance of NTP-based electrodes with PVDF and PVA-PAA binders at 1C rate in 1 M Na<sub>2</sub>SO<sub>4</sub> (aq).

### 3.3.3. Summary

In this part of the work, a number of potential alternative polymeric binders to the common polyvinylidene fluoride (PVDF) suitable for aqueous batteries are prepared and characterized in terms of their mechanical, morphological and electrochemical properties. The obtained results are summarized as:

- A number of silane-based adhesion promoters are screened for PVDF based  $\text{NaTi}_2(\text{PO}_4)_3$  composite electrodes in aqueous electrolytes. The results show that, for example, 3-(triethoxysilyl)propyl isocyanate can improve the adhesion of PVDF binder to the stainless-steel foil current collector. However, the adhesive power is still insufficient for preventing delamination of the electrode composite in aqueous electrolytes during cycling. Moreover, the studied adhesion promoters seem to also form a surface insulating film on the metal foils which affects the electrochemical performance.
- Electrochemically-active polyimides such as Kapton provide binding ability of the electrode and some initial extra charge capacity at relatively high content (20%). However, the adhesion to the stainless-steel foil was not sufficient at these contents, most likely, due to the low concentration of aliphatic groups, and electrochemical activity and degradation of the binder itself.
- Thermoplastic poly(ethylene-vinyl acetate) (PEVA) polymeric binder provides good mechanical properties and adhesion of the electrode composite to the surface of even stainless-steel foil. PEVA-based electrodes show good initial capacity and cycling stability on stainless-steel foil current collector. PEVA is found to be the most promising binder for aqueous batteries.
- Poly(vinyl butyral-co-vinyl alcohol-co-vinyl acetate) copolymer is determined to be the best-performing direct binder which forms covalent bonds with the active material particles. PVBA-based composite electrodes do not show strong adhesion to the metal foil. However, on the mesh current collector they delivered good capacity retention similar to PVDF. The other advantages of PVBA include compatibility with less toxic solvents such as isopropanol and higher active material mass loadings than PVDF.
- Poly(vinyl alcohol-acrylic acid) (PVA-PAA) copolymer did not show strong adhesion to the metal foil current collector during cycling. However, on the mesh current collector they delivered good capacity retention similar to PVDF. The instability during cycling was attributed

to swelling due to  $\text{pH} > 7$  with NTP-based electrodes. The most important advantage of this binder is the ability to be cast from aqueous solution, making it the most environmentally-friendly binder found in this study.

## MAIN RESULTS AND CONCLUSIONS

In this work, the active components of aqueous sodium-ion batteries were designed, prepared, characterized, and optimized. The main focus was on the composite electrodes containing NASICON-structured materials such as  $\text{NaTi}_2(\text{PO}_4)_3$  and  $\text{Na}_2\text{VTi}(\text{PO}_4)_3$ , and electrolyte solutions based on aqueous and simple salt systems. The main results and the conclusions of this work can be summarized as:

1. The charge capacity and cycling stability of the  $\text{NaTi}_2(\text{PO}_4)_3$  electrodes is strongly dependent on the particle carbon coating and conductive additives. The particles of  $\text{NaTi}_2(\text{PO}_4)_3$  can be carbon coated by the pyrolysis of organic compounds in inert atmosphere. The samples coated by citric acid pyrolysis showed better capacity retention at lower carbon loading than those coated by glucose pyrolysis, most likely due to different pyrolyzation and graphitization temperatures of these compounds. The samples coated by pyrolysis of surface polymerized polydopamine showed significantly more uniform, controllable and reproducible carbon coatings. The required carbon loading to ensure the same capacity retention is only half of that as in the case of citric acid pyrolysis.

2. The optimal amount of conductive carbon black additive in the lab-scale composite  $\text{NaTi}_2(\text{PO}_4)_3$  electrodes was determined to be 20 wt%. The mechanical pressing of the electrodes during the transfer onto stainless steel mesh results in higher tap density and lower porosity. The optimal electrochemical properties in terms of initial capacities and retentions during cycling was achieved by hydraulic pressing under 6 t. The duration of slurry mixing during electrode preparation shows significant effects on the carbon dispersion and electrode tap density. The introduction of an additional step of dry component pre-mixing results in even better electrode tap density and uniformity. 1 h of dry premixing and 2 h of slurry mixing results in optimal carbon conductive network inside the electrode.

3. Chemical oxygen reduction reaction catalyzed by  $\text{Ti}^{+3}$  present in the charged state  $\text{Na}_3\text{Ti}_2(\text{PO}_4)_3$  is identified as the main parasitic reaction responsible for self-discharge and pH increase in aqueous electrolyte solutions. Hydrogen evolution is also important, especially at low  $\text{O}_2$  concentrations and C-rates. The removal of oxygen and pH buffering are beneficial for the capacity retention of  $\text{NaTi}_2(\text{PO}_4)_3$  electrodes during cycling. Alkaline environment is shown to be the main cause of degradation for  $\text{NaTi}_2(\text{PO}_4)_3$  electrodes resulting in capacity loss. The EDX, XRD, and NMR analyses show that capacity loss is not directly related to Ti dissolution into

the electrolyte but the formation of insoluble Ti-rich interphase which blocks the electrochemical reaction.

4. The implementation of organic co-solvents such as glycerol and DMSO results in reduced relative water activity and significantly expanded electrochemical stability window of the electrolyte solution. This suppresses the parasitic reactions such as hydrogen and oxygen evolution resulting in longer self-discharge times and significantly better capacity retention of  $\text{NaTi}_2(\text{PO}_4)_3$  electrodes during cycling. Full battery cells containing  $\text{NaTi}_2(\text{PO}_4)_3$  and  $\text{Na}_{1.86}\text{Fe}[\text{Fe}(\text{CN})_6] \cdot 2.28\text{H}_2\text{O}$  Prussian Blue Analog also benefited from the addition of co-solvents. The results show that wider voltage windows and significantly better capacity retention in such electrolytes. The introduction of small amounts of reductive agents such as hydrazine into aqueous electrolytes was shown to effectively scavenge oxygen and suppress oxygen reduction reaction. This procedure allowed to prepare capacity balanced (N/P=1)  $\text{Na}_2\text{VTi}(\text{PO}_4)_3$ - $\text{Na}_2\text{VTi}(\text{PO}_4)_3$  battery cells with good capacity retention.

5. The use of siloxane-based adhesion promoters is insufficient for preventing delamination of the PVDF-based electrode composites in aqueous electrolytes during cycling. Electrochemically-active and hydrophilic polyimides such as Kapton provide good binding of the electrode and some initial extra charge capacity. However, the adhesion to stainless-steel foil is not sufficient, most likely, due to electrochemical activity of the binder itself. Thermoplastic poly(ethylene-vinyl acetate) (PEVA) polymeric binder provides good mechanical properties and even the adhesion of the electrode composite to the surface of stainless-steel foil, good initial capacity, and cycling stability. PEVA is found to be the most promising indirect binder for aqueous systems. Poly(vinyl butyral-co-vinyl alcohol-co-vinyl acetate) (PVBA) copolymer showed good capacity retention similar to PVDF. The other advantages of PVBA include compatibility with less toxic solvents such as isopropanol and higher active material mass loadings. Poly(vinyl alcohol-acrylic acid) copolymer also shows good capacity retention similar to PVDF. The instability during cycling was attributed to swelling due to  $\text{pH} > 7$  with NTP-based electrodes. The most important advantage of this binder is the ability to be cast from aqueous solution, making it the most environmentally-friendly binder found in this study.

## SANTRAUKA

### Įvadas

Sparčiai pereinant prie tvarios energetikos atsiranda vis didėjantis poreikis efektyvioms ir saugioms energijos kaupimo sistemoms. Pastaraisiais metais vis daugiau dėmesio sulaukia vandeninės natrio jonų baterijos - patraukli alternatyva tradiciniams ličio jonų akumuliatoriams. Vandeninės baterijos naudoja vandens pagrindu sukurtus elektrolitus, kurie ženkliai pagerina baterijų saugumą. Jų žaliavos (pvz. natriis) yra gausesnės ir pigesnės, kas mažina gamybos kaštus ir prisideda prie išteklių trūkumo problemos sprendimo. Be to, jų poveikis aplinkai yra švelnesnis nes išvengiama toksiškų ir pavojingų medžiagų naudojimo. Unikali vandeninių baterijų chemija nulemia didelį energijos tankį ir ilgą baterijos gyvavimo laiką, todėl jos yra tinkamos įvairioms energijos kaupimo reikmėms. Apibendrinant, natriis yra prieinama, saugi ir aplinkai draugiška energijos kaupimo alternatyva.

NASICON struktūros medžiagos yra elektrodų aktyviųjų medžiagų klasė, pasižyminti aukštu joniniu laidumu ir struktūriniu stabilumu. Jų unikali trimatė struktūra garantuoja efektyvų natrio jonų transportą, todėl šios medžiagos idealiai tinka natrio jonų baterijoms. Nepaisant visų privalumų, NASICON medžiagos vis dėlto susiduria su keliais iššūkiais, įskaitant prastą elektrinį laidumą, mažesnę talpos stabilumą ir nelabai aplinkai draugiško polivinilidenfluorido naudojimą.

Pagrindinis šio darbo tikslas - sukurti, paruošti, apibūdinti ir optimizuoti vandeninių natrio jonų baterijų aktyviuosius komponentus. Aktyviaisiais komponentais laikomi kompozitiniai elektrodai, kuriuose yra NASICON struktūros medžiagų, tokių kaip  $\text{NaTi}_2(\text{PO}_4)_3$  ir  $\text{Na}_2\text{VTi}(\text{PO}_4)_3$ , ir vandens ir paprastų druskų pagrindu sukurti elektrolitų tirpalai. Optimizavimo procesas apibrėžiamas kaip atitinkami paruošimo, formavimo ir modifikavimo etapai, būtini geriausioms šių komponentų elektrocheminėms savybėms vandeninėse natrio jonų baterijose užtikrinti.

Konkretūs šio darbo tikslai yra šie:

1. Sukurti ir optimizuoti kompozitinių  $\text{NaTi}_2(\text{PO}_4)_3$  elektrodų, naudojamų vandeninėse natrio jonų baterijose, paruošimo metodus, įskaitant anglies dengimą, suspensijos ir elektrodų paruošimą. Įvertinti, kaip paruošimo procesai veikia struktūrines, morfologines ir elektrochemines kompozitinių elektrodų savybes.

2. Sukurti ir optimizuoti vandens pagrindo elektrolitus vandeninėms natrio jonų baterijoms, naudojant papildomus organinius tirpiklius ir priedus

stabilumui pagerinti. Išanalizuoti šiuos elektrolitus fizikocheminiais, spektroskopiniais ir elektrocheminiais metodais.

3. Ieškoti, paruošti ir apibūdinti alternatyvius polimerinius rišiklius, pasižyminčius didesniu hidrofiliškumu, skirtus vandeninėms natrio jonų baterijoms. Įvertinti jų savybes kompozitiniuose elektroduose taikant fizikocheminius ir elektrocheminius metodus.

Šio darbo naujumas kyla iš to, kad tai pirmas kryptingas bandymas ištirti ne tik aktyviosios medžiagos, bet ir kitų aktyviųjų baterijos komponentų įtaką vandeninių natrio jonų baterijų veikimui ir jų optimizavimo metodus. Ankstesnių tyrimų šiomis temomis yra labai nedaug, nes dauguma jų pirmiausia skirti naujų elektrodų aktyviųjų fazių paieškai ir apibūdinimui. Be to, dauguma kitų aktyviųjų baterijos komponentų tyrimų buvo skirti organinių elektrolitų sistemoms.

Ginamieji šios disertacijos teiginiai yra:

1.  $\text{NaTi}_2(\text{PO}_4)_3$  elektrodų talpa ir ciklinis stabilumas labai priklauso nuo aktyviosios medžiagos dalelių anglies dangos. Polidopamino pagrindu gautos dangos užtikrina tolygiausius ir atkuriamiausius rezultatus, o norint išlaikyti panašų talpos stabilumą, reikia perpus mažesnio anglies kiekio nei citrinos rūgšties pirolizės metu. Citrinos rūgštis yra pranašesnė nei gliukozė dėl grafitizacijos temperatūros skirtumų.

2. Optimalus porėtos anglies kiekis laboratorinio mastelio  $\text{NaTi}_2(\text{PO}_4)_3$  elektroduose yra 20 % masės. Hidraulinis suspaudimas 6 t pagerina elektrodo tankį ir sumažina porėtumą, todėl pagerėja elektrocheminės savybės. Optimali anglies dispersija ir elektrodo struktūra gaunamos kai sausi dispersijos komponentai maišomi 1 val. prieš 2 val. suspensijos maišymo.

3.  $\text{NaTi}_2(\text{PO}_4)_3$  elektrodų savaiminį išsikrovimą ir pH padidėjimą daugiausia lemia  $\text{Ti}^{3+}$  katalizuojama deguonies redukcija ir vandenilio skyrimosi reakcija. Deguonies pašalinimas ir buferinių tirpalų naudojimas pagerina talpos stabilumą. Šarminės sąlygos skatina degradaciją ne dėl Ti ištirpimo, o dėl paviršių blokuojančios, Ti turinčios fazės susidarymo.

4. Papildomi organiniai tirpikliai, tokie kaip glicerolis ir DMSO, mažina vandens aktyvumą, išplečia elektrocheminio stabilumo langą ir slopina dujų skyrimosi reakcijas. Tai sulėtina savaiminį išsikrovimą ir pagerina talpos stabilumą. Pilnoms  $\text{NaTi}_2(\text{PO}_4)_3\text{-Na}_{1,86}\text{Fe}[\text{Fe}(\text{CN})_6] \cdot 2,28\text{H}_2\text{O}$  baterijoms tai sąlygoja platesnį įtampos langą ir geresnį veikimą. Be to, nedideli hidrazino kiekiai suredukoja deguonį, todėl galima sukurti subalansuotas pagal talpą  $\text{Na}_2\text{VTi}(\text{PO}_4)_3\text{-Na}_2\text{VTi}(\text{PO}_4)_3$  baterijas, kurios geriau išlaiko talpą ciklinant.

5. Elektrochemiškai aktyvūs poliimidai, tokie kaip kaptonas, pasižymi geromis rišamosiomis savybėmis, bet prasta adhezija su metaliniu srovės kolektoriumi, greičiausiai dėl jų pačių elektrocheminio aktyvumo. PEVA

užtikrina stiprią adheziją su nerūdijančių plienų ir gerą talpos stabilumą, todėl yra perspektyviausias rišiklis vandeninėms sistemoms. PVBA kopolimeras užtikrina puikias elektrochemines savybes, leidžia naudoti didesnius aktyvios medžiagos kiekius ir mažiau toksiškus tirpiklius, tačiau neužtikrina adhezijos su metaliniu srovės kolektoriumi. PVA ir akrilo rūgšties kopolimeras yra ekologiškiausias variantas dėl tirpumo vandenyje. Jis pasižymi geru talpos stabilumu, tačiau išbrinksta šarminiuose elektrolitų tirpaluose.

## 1. Literatūros apžvalga

Akumuliatorių elementai, kaip elektrocheminiai prietaisai, efektyviai paverčia sukaupytą cheminę energiją į elektros energiją vykstant oksidacijos-redukcijos reakcijoms. Elektrocheminio energijos kaupimo istorija prasidėjo XVIII a., kai Alessandro Volta sukonstravo pirmą elektrocheminę bateriją.<sup>7</sup> XIX ir XX amžiaus technologijų vystymasis paskatino mokslinę pažangą energijos šaltinių technologijų srityje. Svarbiausias šio laikotarpio proveržis – įkraunamų baterijų išradimas. Įkraunamąją bateriją sudaro teigiamas ir neigiamas elektrodai bei elektrolitas. Baterijos iškrovimo metu neigiamas elektrodas oksiduojamas, jo elektronai keliauja per išorinę grandinę į teigiamąjį elektrodą, kuriame vyksta redukcija. Tiek įkrovimo, tiek iškrovimo procesų metu elektrolitu juda jonai, užtikrinantys elektroneutralumą.

Šiuo metu ličio jonų baterijos dominuoja įkraunamų baterijų rinkoje. Šios technologijos, pagrįstos grįžtamu jonų įterpimu/ištraukimu vykstant įkrovimui ir iškrovimui, privalumai yra neginčytini, tačiau ribotas ličio prieinamumas, svyruojanti žaliavų kaina ir augantys reikalavimai saugumui nulemia nuolat vykstančią alternatyvų paiešką.<sup>21,22</sup> Natrio jonų baterijos, veikiančios tuo pačiu principu, sulaukia daug dėmesio dėl didesnio paplitimo ir stabilesnių kainų. Natrio jonų baterijos negali pakeisti ličio jonų baterijų srityse, kurios reikalauja aukšto energijos tankio, mažų baterijų matmenų ir greitų įkrovimo greičių, tačiau puikiai tinka pritaikymui sferose, kur baterijos dydis ir svoris nėra tokie svarbūs, pavyzdžiui, stacionariam energijos kaupimui.<sup>26,28</sup>

NASICON-struktūros medžiagos yra atskira natrio jonų baterijoms skirtų medžiagų klasė.<sup>59</sup> Nepaisant to, kad šios medžiagos yra plačiai tyrinėjamos, jų pritaikymo perspektyvos priklauso nuo to ar pavyks įveikti pagrindinius jų trūkumus: prastą elektrinį laidumą, parazitines reakcijas ir nedraugiško aplinkai rišiklio naudojimą. Prastas elektroninis laidumas sulėtina difuzijos procesus, ko pasekoje atsiranda nepatenkinama talpa, lėtas įkrovimo ir iškrovimo greitis, taip pat energijos nuostoliai dėl padidėjusios vidinės varžos,



prastas elektroninis laidumas.<sup>38,67</sup> Parazitinės šalutinės reakcijos, vykstančios vandeninėje terpėje, neigiamai veikia baterijų kuloninį efektyvumą ir baterijų gyvavimo laiką.<sup>38</sup> Siekiant sukurti baterijas su aukšta ir stabilia talpa, labai svarbu slopinti šiuos procesus. Tuo pačiu metu, siekiant tvarumo ir ekologiškumo baterijų paruošimo ir perdirbimo metu, reikia ieškoti alternatyvų fluoruotiems polimerams dėl pavojingų tirpiklių naudojimo.<sup>73</sup>

## 2. Eksperimentiniai metodai

Šiame darbe buvo tiriamos  $\text{NaTi}_2(\text{PO}_4)_3$ ,  $\text{Na}_3\text{V}_2(\text{PO}_4)_3$ ,  $\text{Na}_2\text{VTi}(\text{PO}_4)_3$  ir  $\text{Na}_{1.86}\text{Fe}[\text{Fe}(\text{CN})_6] \cdot 2.28\text{H}_2\text{O}$  medžiagos, kurių sintezės yra apibendrintos 1 lentelėje. Po sintezės, siekiant suvienodinti dalelių dydį, medžiagos buvo sumalamos planetariniame malūne (350 rpm, 2 h). Po malimo visos medžiagos buvo dengiamos anglimi.

1 lentelė. Darbe tiriamų medžiagų sintezės metodų apibendrinimas

Medžiaga	Sintezės metodas
$\text{NaTi}_2(\text{PO}_4)_3$	Išsodinimo
$\text{Na}_3\text{V}_2(\text{PO}_4)_3$	Kietafazė
$\text{Na}_2\text{VTi}(\text{PO}_4)_3$	Kietafazė
$\text{Na}_{1.86}\text{Fe}[\text{Fe}(\text{CN})_6] \cdot 2.28\text{H}_2\text{O}$	Išsodinimo

Iš susintetintų aktyviųjų medžiagų buvo ruošiami elektrodai. Kai kurios susintetintos ir anglimi padengtos medžiagos buvo tiriamos įvairiais metodais:

- Rentgeno spindulių difrakcine analize (Bruker D2 Phaser),
- Skenuojančia elektronų mikroskopija (Hitachi TM-600),
- Peršviečiamąja elektronų mikroskopija (G2 F20 X-TWIN FEI),
- Energijos dispersinės Rentgeno spindulių spektroskopija (Hitachi TM-600),
- Furjė transformacijos infraraudonąją spektroskopiją (Frontier, Perkin-Elmer),
- Rentgeno fotoelektronų spektroskopija (Kratos Axis Supra),
- Paviršiaus ploto analize (Anton Paar NOVA 600),
- Termogravimetrine analize (PerkinElmer STA6000),
- Elementine analize (Thermo Scientific Flash 200).

Elektrodų paruošimo procedūra prasideda nuo 70% aktyviosios medžiagos, 20% anglies, 10% rišiklio ir atitinkamo tirpiklio sumaišymo

planetariniame malūne. Gauta suspensija 300  $\mu\text{m}$  sluoksniu buvo užtepama ant aliuminio/nerūdijančio plieno folijos. Nuo aliuminio folijos išdžiūvę kompozitiniai elektrodai buvo perkeliami ant nerūdijančio plieno tinklelio hidraulinio preso pagalba.

Paruošti elektrodai buvo charakterizuojami vandens pagrindo elektrolituose ciklinės voltamperometrijos (PGSTAT302 Metrohm Autolab) ir galvanostatinio įkrovimo/iškrovimo (Neware CT-4008) metodu pagalba.

Elektrolitų tyrimai buvo vykdomi pasitelkiant Ramano (Renishaw QONTOR) ir branduolių magnetinio rezonanso spektroskopiją (Bruker AVANCE III HD). Elektrolitų laidumas ir pH buvo vertinami naudojant Mettler Toledo SevenCompact s220 su atitinkamais jutikliais.

### 3. Rezultatai ir jų aptarimas

#### 3.1. Anglinės medžiagos elektroduose

Egzistuoja keli veiksmingi būdai aktyviosios medžiagos elektroniniam laidumui pagerinti: dalelių dydžio mažinimas, legiravimas ir laidžių medžiagų naudojimas.<sup>85–87</sup> Pastarasis būdas veikia sukurdamas išorinį laidų tinklą, užtikrinantį greitą ir sklandų elektronų judėjimą.<sup>215</sup> Anglinės medžiagos, tokios kaip porėta anglis, anglies nanovamzdeliai ir grafenas, sėkmingai sumažina varžą ir pagerina kompozitinio elektrodo laidumą.<sup>89,90</sup> Sukurti kompozitinį elektrodą su nepertraukiamu laidžiu tinklu, panaudojant kuo mažiau anglies, yra didžiausia siekiamybė. Tam pasiekti anglis turi būti naudojama ne tik elektrodo paruošimo metu, bet ir dengiant aktyvias medžiagas.

#### Anglies juodasis

Anglies vaidmuo elektrode neapsiriboja laidumo pagerinimu, jis taipogi prisideda prie homogeniškumo užtikrinimo. Homogeniški elektrodai pasižymi geresniu mechaniniu integralumu pakrovimo/iškrovimo metu, kas nulemia ilgesnį baterijos gyvavimo laiką. Anglies juodasis – pigi, saugi ir stabili anglis, kuri rado pritaikymą baterijų gamyboje.<sup>99</sup> Anglies juodojo kiekis, reikalingas geriausioms elektrocheminėms savybėms pasiekti, yra pakankamai didelis ir gali neigiamai atsiliiepti mechaninėms elektrodo savybėms.<sup>100</sup> Taip pat svarbu nepamiršti, kad bet kokio papildomo komponento dalies didinimas vyksta aktyviosios medžiagos sąskaita, kas mažina baterijos energijos tankį ir padaro tokią bateriją mažiau tinkamą

praktiniams pritaikymams. Todėl, nustatant optimalią elektrodo sudėtį, yra labai svarbu ieškoti kompromiso.

$\text{NaTi}_2(\text{PO}_4)_3$  elektrodų, paruoštų su trimis skirtingais anglies juodojo kiekiais (5, 10, 20 %), elektrocheminės savybės buvo tiriamos galvanostatinio įkrovimo/iškrovimo būdu. Išsiaiškinta, kad anglies kiekis buvo tiesiogiai proporcingas ir elektrodų stabilumui ir pradinėms talpoms. Mažesnės pradinės talpos (81,1 ir 85,4 mAh/g) mėginams su 5 ir 10 % anglies gali būti paaiškintos nepakankamu elektrodo laidumu ir lėta kinetika.<sup>107</sup> Padvigubinus anglies juodojo kiekį, pradinė talpa išaugo iki 94,6 mAh/g, kas byloja apie pagerėjusį elektronų transportą. Didinant anglies kiekį elektrodo sudėtyje augo ir talpos stabilumas po 100 įkrovimo/iškrovimo ciklų (27,7 → 59,9 → 62,5 %). Augantis ciklinimo stabilumas – geresnio elektronų transporto pasekmė. Nepaisant teigiamų tendencijų, toliau didinti anglies kiekį yra tiesiog nepraktiška elektrodo energijos tankiui.

#### Aktyviųjų medžiagų paviršiaus dengimas anglimi

Yra keletas plačiai naudojamų metodų anglies dangai ant keraminių medžiagų suformuoti. Vienas iš jų pagrįstas anglies pirtakų, naudojamų sintezės ar papildomo apdorojimo metu, pirolize.<sup>109</sup> Pirolizės metu organiniai junginiai suyra inertinėje atmosferoje, palikdami daug anglies turintį pirolizės produktą. Šis metodas užtikrina kontroliuojamą pirtakų virsmą į anglines plėveles, kurios pagerina laidumą ir elektrodų talpas.<sup>111</sup> Kadangi NTP pasižymi terminiu stabilumu, leidžiančiu atlikti pirolizę aukštoje temperatūroje, šiam tyrimui buvo pasirinktas būtent šis metodas.

Šiame tyrime buvo lyginamas dviejų anglies pirtakų - citrinos rūgšties (CA) ir gliukozės - poveikis elektrocheminėms savybėms. Pirtakų kiekis sudarė 10, 15, 20, 30 % nuo bendros masės. Termogravimetrinis tyrimas parodė, kad, nepaisant panašaus anglies kiekio pirtakuose, anglies kiekis galutiniame kompozite buvo didesnis gliukozės (3,14 – 10,24 %) nei citrinos rūgšties (1,74 – 4,94 %) serijai. Galvanostatinio įkrovimo/iškrovimo tyrimas parodė, kad talpos stabilumas ciklinant augo didinant anglies kiekį  $\text{NaTi}_2(\text{PO}_4)_3\text{-C}$  kompozite. Abejose serijose talpos stabilumas pasiekė plato ties 80 %, tačiau šiam rezultatui pasiekti prireikė skirtingo anglies kiekio – 3,45 % elektrodai paruoštam su citrinos rūgštimi ir 6,32 % elektrodai paruoštam su gliukoze. Šio tyrimo metu išsiaiškinta, kad naudojant citrinos rūgštį kaip anglies pirtaką ant aktyviosios medžiagos, susidaro anglies danga, kuri efektyviau apsaugo medžiagą nuo degradacijos.

Užauginus polidopamino sluoksnį ant aktyvios medžiagos dalelių paviršiaus prieš pirolizę buvo gauti  $\text{NaTi}_2(\text{PO}_4)_3\text{-C}$  kompozitai, kurie buvo

lyginami su citrinos rūgšties pagrindu susintetintais kompozitais. FTIR analizė patvirtino sėkmingą polimerinės dangos susidarymą ir anglinės dangos susidarymą po pirolizės. Termogravimetrinė analizė parodė, kad anglies kiekis galutiniame kompozite priklauso ne tik nuo dopamino (pirmtako) kiekio, bet ir nuo polimerizacijos reakcijos trukmės. Peršviečiamosios elektronų mikroskopijos analizė parodė, kad mėginiai, gauti po citrinos rūgšties pirolizės, pasižymi ne tik amorfiniu anglies sluoksniu ant dalelių paviršiaus, bet ir didelėm anglinėm struktūrom tarp dalelių. Tuo tarpu polidopaminu dengtų dalelių atveju visa anglis pasiskirstė tik ant dalelių paviršiaus, suformuodama vientisą sluoksnį. Taipogi paviršiaus elementinės sudėties analizės metu nustatyta, kad dengiant polidopaminu paviršiuje gaunamas stochiometrinis Na/Ti santykis, o dengiant citrinos rūgštimi jis yra iškreipiamas. Tai dar kartą patvirtina, kad polidopaminas nesąveikauja su  $\text{NaTi}_2(\text{PO}_4)_3$ . Elektrocheminių savybių tyrimo metu išsiaiškinta, kad paviršinė anglis gauta po polidopamino pirolizės sąlygojo aukštesnes pradines talpas (98-111 mAh/g) nei citrinos rūgšties pirolizės metu gauta anglis (90 - 95 mAh/g). Šis skirtumas paaiškinamas geresniu elektroniniu laidumu, kuris atsirado dėl tolygesnio anglies pasiskirstymo paviršiuje. Taip pat nustatyta, kad talpos stabilumas ciklinant augo didinant anglies kiekį  $\text{NaTi}_2(\text{PO}_4)_3$ -C kompozite. Aukščiausias (38 %) talpos stabilumas po 200 įkrovimo/iškrovimo ciklų buvo gautas mėginams su 11,9 % (anglies pirmtakas – citrinos rūgštis) ir 6.7 % (anglies pirmtakas – polidopaminas) anglies galutiniame kompozite. Anglies danga, gauta iš polidopamino, yra labiau homogeniška ir vientisa, todėl geriau apsaugo aktyviąją medžiagą nuo vandeninėje terpėje vykstančių parazitinių reakcijų.

#### Elektrodų paruošimas

Anglies pasiskirstymas elektrode turi įtakos mechaninėms bei elektrocheminėms elektrodo savybėms. Eksperimentinėje dalyje pateiktas elektrodų paruošimo procesas yra čia pateikto tyrimo rezultatas.

Elektrodo kompozito tankis rodo mikrostruktūros homogeniškumą ir optimizuotą elektrodo sudėtį. Pramonėje paruošti elektrodai yra papildomai sutankinami spaudžiant, kad būtų pagerintas sukibimas ir padidintas elektrodų tankis. Tyrimai rodo, kad, didėjant elektrodo tankiui, iki tam tikros ribos didėja elektrodo stabilumas ciklinant. Tai patvirtina spaudimo poveikio elektrocheminėms savybėms tyrimas. Elektrodų, perkeltų ant nerūdijančio plieno tinklelio, ciklinis stabilumas didėja perkėlimo slėgiui didėjant nuo 4 iki 8 t (35,5 % → 44,2 %). Tačiau spaudžiant elektrodą 8 t pasidaro sudėtinga atskirti aliuminio foliją nuo elektrodo, kas gali atsiliepti pašalinėmis

reakcijomis vandeninėje terpėje ir netiksliai masės nustatymu elektrodo svėrimo metu. Pradinė talpa turi nedidelę augimo tendenciją (82,55 mAh/g → 87,65 mAh/g).

Tinkamai parinktas srovės kolektorius taip pat turi įtakos elektrocheminėms elektrodo savybėms. Kai naudojamas itin retas nerūdijančio plieno tinklelis (#80), elektrodas parodo prastesnį (24,4 %) stabilumą ciklinant nei elektrodai ant tankesnių (#200, #325, #400) tinklelių (35,5 %, 58,9 %, 61,5 %). Galima daryti išvadą, kad kai tinklelis turi nepakankamai kontakto su elektrodu, jis negali užtikrinti greito elektronų transporto į visus elektrodo taškus, todėl jo veikimas yra prastesnis.

Padidinti elektrodo tankį galima ir ilginant elektrodo suspensijos maišymo laiką. Ilginant maišymo planetariniame malūne trukmę nuo 30 min iki 180 min buvo gauti labiau homogeniški ir didesnio tankio elektrodai (0,60 → 0,65 mg/cm<sup>3</sup>). Įvedus papildomą kietųjų komponentų (anglies ir aktyviosios medžiagos) sumaišymo žingsnį gauti dar labiau homogeniški ir tankūs elektrodai. Optimalus homogeniškumas ir tankis (0,96 mg/cm<sup>3</sup>) buvo nustatyti elektrodui, kurio kietieji komponentai buvo maišomi 1 h 3 mm keraminiais rutuliais, o elektrodo dispersija buvo maišoma 2 h 5 mm keraminiais rutuliais.

### 3.2. Elektrolitai

Vandens pagrindo elektrolitai pasižymi geresniu terminiu stabilumu, ekologiškumu ir dideliu joniniu laidumu palyginti su organiniais, polimeriniais ir kietaisiais elektrolitais.<sup>147</sup> Vandenilinių ryšių tinklas palengvina greitą jonų difuziją į elektrodų paviršių. Tačiau siauras vandens elektrocheminio stabilumo langas lemia parazitines reakcijas, pavyzdžiui, vandenilio ir deguonies išsiskyrimo reakcijas, kurios mažina įkrovos ir iškrovos ciklo Kuloninį efektyvumą.<sup>148</sup> Be to, šios reakcijos sukelia vietinius pH pokyčius, kurie ilgainiui paveikia aktyviąją medžiagą, todėl nukenčia elektrodų ciklo stabilumas.<sup>132,149</sup>

#### Vandeniniai elektrolitai

Dvi pagrindinės reakcijos, prisidedančios prie vietinio pH augimo yra vandenilio skyrimosi reakcija



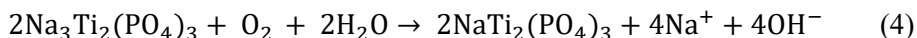
ir ištirpusio deguonies redukcija



arba



Dar viena reakcija, kuri itin prisideda prie elektrolito tirpalo šarmėjimo, yra cheminė deguonies redukcija. Ji atsakinga už talpos degradaciją ir sumažėjusį elektrodo gyvavimo laiką.<sup>157,158</sup>  $\text{Ti}^{\text{III}}$ , kurį galima rasti įkrautame  $\text{Na}_3\text{Ti}_2(\text{PO}_4)_3$ , katalizuoja cheminės redukcijos reakciją:



Šią reakciją galima nuslopinti pašalinus ištirpusį deguonį iš elektrolito tirpalo inertinių dujų pagalba. Du  $\text{NaTi}_2(\text{PO}_4)_3$  elektrodai buvo ciklinami įkraunant/iškraunant ore ir azoto dujų atmosferoje. Elektrodas su ribotu deguonies patekimu pasiekė ~99 % kuloninį efektyvumą per 10 ciklą ir išliko stabilus per kitus 90 ciklą. Talpos sumažėjimas po 100 ciklą siekė tik 6 %. Tai patvirtina mintį, kad deguonies pašalinimas slopina parazitines reakcijas, lemiančias pH pokyčius ir talpos sumažėjimą. Tuo pačiu metu ore ciklinamas elektrodas pasiekė 92 % kuloninį efektyvumą ir prarado 76 % pradinės talpos. Abiejų elektrolitų pH buvo stebimas ciklinimo metu ir pastebėta, kad aukščiausias pH, pasiektas elektrolitui oro atmosferoje, yra 10,5, o inertinių dujų atmosferoje tik 8,5. Akivaizdu, kad pH kenkia elektrodo veikimui.

pH įtaka  $\text{NaTi}_2(\text{PO}_4)_3$  elektrodams buvo toliau tiriama skirtingose pradinėse elektrolito pH. Elektrolitų pH buvo užtikrinamas pasitelkus buferių pagalbą. Galvanostatinio įkrovimo/iškrovimo tyrimas parodė, kad esant pH=4 stebimas itin žemas (~24 %) pradinis kuloninis efektyvumas, kuris paaugo iki 75 % per 100 ciklą. Toks žemas efektyvumas gali būti paaiškintas sparčiais vykstančiu vandenilio skyrimusi, kuris buvo stebimas ir plika akimi. Šio elektrodo talpa buvo žema, tačiau talpos stabilumas po 100 ciklą siekė net 90 %. Esant pH=7 buvo stebimas aukštesnis kuloninis efektyvumas ir aukštesnė pradinė talpa (~ 120 mAh/g). Akivaizdu, kad vandenilio skyrimosi įtaka sumažėjo. Kai elektrolito tirpalo pH buvo 10, kuloninis efektyvumas siekė beveik 100 %, tačiau, per 100 ciklą elektrodas prarado apie pusę pradinės talpos. Tai reiškia, kad šarminė terpė įneša pagrindinį indelį į elektrodų talpos praradimą.

Elektrodui, ciklintam šarminiame elektrolite, buvo užrašytos rentgeno spindulių difraktogramos. Pasinaudojus vidinio standarto metodu buvo nustatyta, kiek kristalinės  $\text{NaTi}_2(\text{PO}_4)_3$  fazės lieka elektrode ciklinant. Nustatytas kristalinės fazės praradimas (~ 15 %) buvo daug mažesnis nei talpos praradimas ciklinant.

Energijos dispersinė Rentgeno spindulių spektroskopija parodė, kad, nepaisant kristalinės fazės sumažėjimo, Ti kiekis elektrode išliko stabilus. Šie rezultatai parodo, kad talpos praradimas vyksta dėl netirpaus sluoksnio ant aktyvios medžiagos paviršiaus formavimosi. Šis sluoksnis blogina prieigą prie aktyvios medžiagos ir lemia kontakto ir talpos praradimą.

### Hibridiniai elektrolitai

Papildomų tirpiklių naudojimas padeda sukurti vandens-tirpiklis sąveikų tinklą, kas sumažina vandens aktyvumą ir padeda pagerinti elektrocheminį stabilumą. Saugūs ir nebrangūs tirpikliai dimetilsulfoksidas ir glicerolis sudaro vandenilines jungtis su vandeniu, todėl puikiai tinka ko-tirpiklio rolei.

Šiam tyrimui buvo paruoštos dvi elektrolitų tirpalų serijos: su dimetilsulfoksidu ir gliceroliu. Ko-tirpiklio kiekis tirpikliuose kito nuo 10 iki 60 mol%. Laidumo ir klampos tyrimai parodė, kad visų gautų elektrolitų tirpalų fizikocheminiai parametrai yra jau paskelbtų ir naudojamų elektrolitų tirpalų laidumo ir klampos ribose. Linijinė skenuojanti voltamperometrija padėjo išsiaiškinti, kad didėjant ko-tirpiklio moliniam procentui elektrolito tirpiklyje plėtėsi elektrocheminio stabilumo langas. Ramano spektroskopijos pagalba išsiaiškinta, kad tarp ko-tirpiklio ir vandens susidaro stipresni vandeniliniai ryšiai nei tarp vandens molekulių. Elektrocheminis charakterizavimas parodė, kad didinant ko-tirpiklio kiekį elektrolito tirpale galima pasiekti aukštą talpos stabilumą. Elektrodas, ciklintas vandeniniame elektrolite prarado 72 % pradinės talpos, tuo metu kai panaudojus 40 ir 50 mol % glicerolio ir dimetilsulfoksido talpos netekimas siekė tik 5 ir 12 %, atitinkamai. Toks talpos stabilumo pagerėjimas paaiškinamas sumažėjusiu vandens aktyvumu ir mažesniu parazitinių reakcijų indėliu. Savaiminio išsikrovimo tyrimas parodė, kad ko-tirpikliai padeda prailginti savaiminio išsikrovimo laiką. Elektrolitų tirpalai, turintys glicerolio savo sudėtyje, parodė geresnį atsparumą procesams, kurie sunaudoja elektrodo krūvį – parazitinėms reakcijoms ir difuzijai. Dėl didesnės klampos glicerolis sudaro prastesnes sąlygas difuzijai, tad elektrodai ilgiau lieka įkrauti. Ko-tirpiklių naudojimas turėjo teigiamos įtakos ne tik  $\text{NaTi}_2(\text{PO}_4)_3$ , bet ir  $\text{Na}_{1,86}\text{Fe}[\text{Fe}(\text{CN})_6] \cdot 2,28\text{H}_2\text{O}$  elektrodui. Pilna baterija, susidedanti iš šių elektrodų, buvo surinkta ir elektrochemiškai ištirta hibridiniuose elektrolituose. Tyrimas atskleidžia, kad ko-tirpiklių panaudojimas padėjo išplėsti ciklinimo potencialų langus, gauti aukštesnes talpas ir geresnį kuloninį efektyvumą. Tai byloja apie sėkmingą parazitinių reakcijų slopinimą.

### Redukuojantys priedai

Kaip jau išsiaiškinta, cheminė deguonies redukcija vaidina svarbiausią vaidmenį elektrodo talpos degradacijoje. Redukuojančių priedų, tokių kaip hidrazinas, panaudojimas leidžia atsikratyti nepageidaujamos ištirpusios deguonies elektrolito tirpale:



0,1 M hidrazino buvo pridėta į tris skirtingus elektrolitų tirpalus: su neutraliu pH, su šarminiu pH ir su DMSO ko-tirpikliu. Elektrodų (su ir be hidrazino) galvanostatinio iškrovimo/įkrovimo rezultatai palyginti tarpusavyje ir parodyta, kad hidrazinas turėjo itin teigiamos įtakos talpos stabilumui. Talpos stabilumo pagerėjimas akivaizdžiausias elektrolito tirpalui su šarminiu pH. Be redukuojančio priedo jo talpos stabilumas siekė vos 9 %, o 0,1 M hidrazino padėjo nuslopinti cheminę deguonies redukciją ir talpos stabilumas pakilo iki 75 %. Neutraliame elektrolito tirpale, kur deguonies skyrimosi įtaka yra stipresnė, talpos stabilumas paaugo nuo 30 % iki 53 %. Elektrolito tirpalas su ko-tirpikliu sėkmingai slopina vandenilio skyrimosi reakciją, todėl, pašalinus iš jo ištirpusį deguonį, talpos stabilumas ciklinant pasikeitė iš 80 % iki 97 %. Toks rezultatas pabrėžia, kad sujungus hibridinio elektrolito ir redukuojančio agento privalumus galima gauti elektrolito tirpalą, kuriame beveik nevyksta šalutinės reakcijos.

#### Organinių tirpiklių pagrindo elektrolitai

Organiniuose elektrolituose nevyksta deguonies ir vandenilio skyrimosi reakcijos, todėl, palyginti su vandeniniais elektrolitais, jie gali veikti platesniame įtampos diapazone.<sup>183</sup> Šis platesnis elektrocheminio stabilumo diapazonas leidžia pasiekti didesnę energijos tankį baterijose, todėl organiniai elektrolitai tinkami naudoti tais atvejais, kai reikia kompaktiškų ir lengvų energijos saugojimo sprendimų. Be to, daugelis didelės energijos elektrodų medžiagų, pavyzdžiui, litis ir natris, yra stabilesnės ir (arba) geriau veikia su organiniais elektrolitais.<sup>184</sup> Šie privalumai tapo paskata apibūdinti elektrodus aplinkoje, kurioje nėra vandens, kad būtų atskleistas visas elektrodų potencialas.

$\text{NaTi}_2(\text{PO}_4)_3$  elektrodai buvo tiriami elektrolitų tirpaluose propilenkarbonato pagrindu.  $\text{NaPF}_6$  ir NATFSI – dvi populiarios organinių elektrolitų druskos – buvo naudojamos elektrolitams paruošti. Galvanostatinis įkrovimas/iškrovimas parodė, kad  $\text{NaTi}_2(\text{PO}_4)_3$  elektrodai labai stabiliai ciklinasi šiuose elektrolitų tirpaluose (92 % ir 100 %). Toks stabilumas nestebina, žinant, kad elektrodų neįtakoja nei vandenilio skyrimasis nei



ištirpusios deguonies redukcija. Didesnis elektrolitų tirpalų elektrocheminis stabilumas leidžia pasiekti dar vieną  $\text{NaTi}_2(\text{PO}_4)_3$  redokso reakciją  $\text{Ti}^{3+/2+}$ , ir gauti talpą, kurios negalima gauti elektrolituose. Išplėtus ciklinimo potencialą iki [0,2 – 2,4 V] buvo gautos apie 200 mAh/g pradinės talpos, kurios, deja greitai degradavo ciklinant (62 % ir 65 %). Papildomų priedų naudojimas nepadėjo pagerinti talpos stabilumo organiniuose elektrolitų tirpaluose. Šie rezultatai pabrėžia, kad atsakingai parenkant vandeninio elektrolito sudėtį galima pasiekti elektrodų našumą analogišką organiniams elektrodams.

### 3.3. Rišikliai

Priklausomai nuo polimero, surišimas atsiranda dėl cheminės (tiesioginis surišimas) arba fizinės (netiesioginis surišimas) sąveikos. Tiesioginio arba kovalentinio surišimo atveju vyksta stipri polimerinės matricos adsorbcija ant veikliosios medžiagos. Netiesioginis surišimas vyksta nesant reaktyvių funkcinių grupių dėl mechaninės/fizinės adsorbcijos veikliųjų medžiagų paviršiuje. Šiame darbe tiek tiesioginiai, tiek netiesioginiai rišikliai tiriami  $\text{NaTi}_2(\text{PO}_4)_3$  elektrode vandeniniuose elektrolituose.

#### Netiesioginiai rišikliai

Polivinildenfluoridas šiuo metu yra plačiausiai naudojamas polimerinis rišiklis. Jis yra itin chemiškai atsparus ir stabilus, tačiau nepasižymi gera adhezija prie metalų. Dėl to visi elektrodai turi būti perkeliami ant nerūdijančio plieno tinklelio. Šis papildomas žingsnis yra technologiškai nenaudingas, nes reikalauja papildomų sąnaudų. Polivinildenfluorido adheziją prie metalų buvo bandyta pagerinti silaniniais junginiais, kurie dažnai naudojami adhezijos gerinimui. Naudojant 5 % šių priedų adhezija buvo ženkliai pagerinta, bet nepakankamai, kad metodas būtų praktiškai pritaikomas. Tuo pačiu metu elektrodų pradinės talpos sumažėjo. Tikėtina, kad adheziją gerinančios medžiagos suformavo izoliuojantį sluoksnį ant aktyviųjų medžiagų paviršiaus.

Kitas polimeras naudojamas kaip netiesioginis rišiklis  $\text{NaTi}_2(\text{PO}_4)_3$  elektroduose buvo poliimidas kaptonas. Standartinėje formuluotėje, kurioje polimerai sudaro 10 % visos elektrodo masės, kaptonas neturėjo tokio pat sukibimo su metaliniu substratu kaip gryna kaptono plėvelė. Taip pat buvo paruoštas elektrodas, kurio 20 % sudaro kaptonas ir 60 % aktyvioji medžiaga. Padidinus rišiklio kiekį du kartus, adhezija labai nepagerėjo. Abu elektrodai buvo perkelti ant tinklelio, siekiant ištirti jų elektrochemines savybes. Pradinę greitą talpos sumažėjimą galima paaiškinti elektrocheminiu kaptono

nestabilumu vandenyje, kurį atskleidė CV tyrimas. Iš įkrovimo/iškrovimo rezultatų matyti, kad, nepaisant to, jog nebuvo užtikrintas pageidaujamas sukibimas, didesnis rišiklio kiekis padėjo padidinti pradinę bandinio talpą (66 ir 95 mAh/g). Elektrodas su 20 % kaptono pasižymi mažesniu cikliniu stabilumu nei elektrodas polivinilidenfluorido pagrindu (54 % palyginti su 79 %). Be to elektrodai su kaptonu turi prastą sukibimą su metalu, sudėtingą paruošimo procedūrą, sumažėjusį aktyviosios medžiagos kiekį ir negali sudaryti konkurencijos elektrodams su polivinilidenfluoridu.

Dar vienas polimeras naudojamas kaip netiesioginis rišiklis  $\text{NaTi}_2(\text{PO}_4)_3$  elektroduose yra poli(etilen-ko-vinil acetatas). Šiam tyrimui elektrodas buvo paruoštas pagal modifikuotą procedūrą: veiklioji medžiaga ir anglis buvo disperguotos tirpale, gautame ištirpinant poli(etilen-ko-vinil acetato) granules toluene 60 °C temperatūroje. Karšta dispersija buvo liejama tiesiai ant nerūdijančio plieno folijos. Išgarinus tirpiklį gautas lankstus ir patvarus elektrodas. Elektrodai buvo charakterizuoti galvanostatiškai ciklinant ir parodyta, kad poli(etilen-ko-vinil acetato) turintis elektrodas pasižymi geresniu talpos stabilumu (86 %), palyginti su polivinilidenfluoridu (21 %). Tai patvirtina puikų elektrodo sukibimą su srovės kolektoriumi ciklinimo metu. Mažesnę pradinę talpą (80 mAh/g) galima paaiškinti netobula paruošimo procedūra: maišymą reikėjo atlikti esant aukštai temperatūrai, todėl jo nebuvo galima atlikti planetiniame malūne. Maišant magnetine maišykle, suspensija galėjo būti mažiau homogeniška nei norėta. Taip pat gali būti, kad EVA ant veikliosios medžiagos paviršiaus suformavo izoliacinę plėvelę. Tačiau, esant tokiam talpos stabilumui, mažesnė pradinė talpa neatsveria akivaizdžių adhezijos prie metalo privalumų.

#### Tiesioginiai rišikliai

Poli(vinil butiralo-vinil alkoholio-vinil acetatas) (PVBA) buvo išbandytas  $\text{NaTi}_2(\text{PO}_4)_3$  elektrodo sudėtyje. Nepaisant didelio pradinio sukibimo su metaliniu substratu, galvanostatiškai ciklinant PVBA turintys elektrodai greitai atsilupo nuo nerūdijančio plieno folijos paviršiaus. Nepaisant to, elektrodas buvo perkeltas ant nerūdijančio plieno tinkelio ir, atliekant ciklinimo tyrimą, nustatyta, kad PVBA ir polivinilidenfluorido pradinės talpos buvo labai panašios - 87 ir 89 mAh/g, atitinkamai. Talpos stabilumas atskleidė nedidelį polivinilidenfluorido pranašumą (67 % prieš 79 %). Tai galima paaiškinti bendra reaktyviųjų grupių tendencija sąveikauti su vandeniu ir brinkti, todėl gali keistis elektrodo tūris ir kaip pasekmė prarandamas kontaktas. Svarbu paminėti, kad šis polimeras yra tirpus izopropanolyje, o tai gera alternatyva toksiškam ir brangiam N-metil-2-pirolidonui. Papildomi

tyrimai parodė, kad naudojant PVBA galima gauti 1000  $\mu\text{m}$  storio elektrodą kai polivinilidenfluoridui buvo nustatyta 300  $\mu\text{m}$  storio kritinė riba, kai elektrodai dar gaunami be įtrūkimų ir su geru vientisumu. Elektrodo storis turi didelę reikšmę elektrodo energijos tankiui, nes storesni elektrodai gali sumažinti elektrochemiškai neaktyvių medžiagų, tokių kaip srovės kolektoriai ir separatoriai, masės indelį į bateriją.

Šiam tyrimui poli(vinilo alkoholio-akrilo rūgštis) PVA-PAA, kurios masės santykis yra 4:1, buvo paruošta kopolimerizuojant šias medžiagas. Elektrodai su šiuo kopolimeru buvo paruošti pagal standartinę procedūrą. Kaip ir PVBA, šis rišiklis pasižymėjo sukibimu su metalu vandenyje, tačiau po pirmųjų ciklų atsiskyrė nuo metalinio pagrindo. Siekiant ištirti PVA-PAA rišamąsias savybes, elektrodas buvo perkeltas ant nerūdijančiojo plieno tinklelio. Galvanostatiškai ciklinant šį elektrodą talpos stabilumas siekė 61 % po 100 ciklų. Literatūros analizė parodė, kad PVA-PAA tinklas persitvarko priklausomai nuo tirpalo pH.<sup>214</sup> Nustatyta, kad didesnės pH vertės sukelia brinkimą, todėl ciklinimo metu mažėja talpa ir talpos stabilumas. Elektrolito buferiavimas rūgštinėje terpėje pagerintų rišiklio stabilumą, tačiau paskatintų vandenilio skyrimąsi. Hibridinių elektrolitų naudojimas galėtų sumažinti vandens aktyvumą ir sušvelninti brinkimo poveikį.

#### 4. Pagrindiniai rezultatai ir išvados

Šiame darbe buvo paruošti, apibūdinti ir optimizuoti vandeninių natrio jonų baterijų aktyvūs komponentai. Daugiausia dėmesio skirta kompozitiniams elektrodams, kurių sudėtyje yra NASICON struktūros medžiagų, tokių kaip  $\text{NaTi}_2(\text{PO}_4)_3$  ir  $\text{Na}_2\text{VTi}(\text{PO}_4)_3$ , ir elektrolitų tirpalams, kurie pagaminti vandens ir paprastų druskų pagrindu. Šio darbo išvadas galima apibendrinti taip:

1.  $\text{NaTi}_2(\text{PO}_4)_3$  elektrodų talpa ir ciklo stabilumas labai priklauso nuo anglies dalelių dangos ir laidžiųjų priedų.  $\text{NaTi}_2(\text{PO}_4)_3$  dalelės gali būti padengtos anglimi pirolizės būdu vykdant organinių junginių pirolizę inertinėje aplinkoje. Bandiniai, padengti citrinų rūgšties pirolizės metodu, pasižymėjo geresniu talpos stabilumu esant mažesnei anglies masei nei bandiniai, padengti gliukozės pirolizės būdu, greičiausiai dėl skirtingos šių junginių pirolizės ir grafitizacijos temperatūros. Bandiniai, padengti paviršinio polidopamino pirolizės būdu, pasižymėjo žymiai tolygesnėmis, kontroliuojamomis ir atsikartojančiomis anglies dangomis. Tam, kad būtų užtikrintas toks pat talpos stabilumas, reikalingas perpus mažesnis anglies kiekis nei citrinos rūgšties pirolizės atveju.

2. Nustatyta, kad optimalus laidžiosios anglies priedo kiekis kompozitiniuose  $\text{NaTi}_2(\text{PO}_4)_3$  elektroduose yra 20 masės %. Praktiniam naudojimui tolesnis užpildo kiekio didinimas yra neįmanomas. Perkelti elektrodus ant nerūdijančiojo plieno tinklelio mechaniškai suspaudus, gaunamas didesnis tankis ir mažesnis porėtumas. Optimalios elektrocheminės savybės, susijusios su pradinėmis talpomis ir talpos stabilumu, buvo pasiektos atliekant hidraulinį suspaudimą, kai slėgis buvo mažesnis nei 6 t. Elektrodo dispersijos maišymo trukmė ruošiant elektrodus turi didelę įtaką anglies dispersijai ir elektrodų tankiui. Įvedus papildomą sausų komponentų išankstinio maišymo etapą, pasiekiamas dar geresnis elektrodo tankis ir tolygumas. Po 1 val. sausų komponentų išankstinio maišymo ir 2 val. suspensijos maišymo elektrodo viduje susidaro optimalus laidus anglies tinklas.

3. Cheminė deguonies redukcijos reakcija, kurią katalizuoja  $\text{Ti}^{+3}$ , esantis įkrautame  $\text{Na}_3\text{Ti}_2(\text{PO}_4)_3$ , yra pagrindinė parazitinė reakcija, lemianti savaiminį išsikrovimą ir pH padidėjimą vandeniniuose elektrolitų tirpaluose. Vandenilio išsiskyrimas taip pat yra svarbus, ypač esant mažai  $\text{O}_2$  koncentracijai ir C greičiui. Deguonies pašalinimas ir pH buferiavimas yra naudingi  $\text{NaTi}_2(\text{PO}_4)_3$  elektrodų talpos stabilumui ciklinimo metu. Įrodyta, kad šarminė aplinka yra pagrindinė  $\text{NaTi}_2(\text{PO}_4)_3$  elektrodų degradacijos priežastis, dėl kurios prarandama talpa. EDX, XRD ir NMR analizės rodo, kad talpos praradimas tiesiogiai susijęs ne su Ti ištirpimu elektrolite, o su netirpios Ti turinčios fazės, blokuojančios elektrocheminę reakciją, susidarymu.

4. Papildomų organinių tirpiklių, pavyzdžiui, glicerolio ir DMSO, naudojimas pertvarko vandens vandenilinių ryšių tinklą, sumažindamas santykinį vandens aktyvumą ir gerokai išplėsdamas elektrocheminio stabilumo langą. Tai slopina vandenilio ir deguonies išsiskyrimą, todėl pailgėja savaiminio išsikrovimo laikas ir pasiekiamas žymiai geresnis talpos stabilumas.  $\text{NaTi}_2(\text{PO}_4)_3$  -  $\text{Na}_{1,86}\text{Fe}[\text{Fe}(\text{CN})_6] \cdot 2,28\text{H}_2\text{O}$  pilnai baterijai taip pat naudingi organiniai papildomi tirpikliai: pasiekiami platesni įtampų langai ir žymiai geresnis talpos stabilumas. Nedideli redukuojančių medžiagų, tokių kaip hidrazinas, kiekiai efektyviai suriša deguonį ir slopina deguonies redukcijos reakciją, todėl galima paruošti subalansuotos talpos  $\text{Na}_2\text{VTi}(\text{PO}_4)_3$ - $\text{Na}_2\text{VTi}(\text{PO}_4)_3$  baterijas, kurių talpa išlieka stabili.

5. Siloksano pagrindu pagamintų sukibimą skatinančių medžiagų nepakanka, kad būtų išvengta kompozitų atsisluoksniavimo nuo nerūdijančio plieno folijos vandeniniuose elektrolituose ciklinimo metu. Elektrochemiškai aktyvūs ir hidrofiliniai poliimidai, tokie kaip kaptonas, užtikrina gerą elektrodo sukibimą ir tam tikrą pradinę papildomą įkrovos talpą. Tačiau sukibimas su metaline folija nėra pakankamas, greičiausiai dėl paties rišiklio

elektrocheminio aktyvumo. Termoplastinis poli(etileno-vinilacetato) (PEVA) polimerinis rišiklis užtikrina geras mechanines savybes ir net elektrodų kompozito sukibimą su nerūdijančio plieno folijos paviršiumi, gerą pradinę talpą ir talpos stabilumą. Nustatyta, kad PEVA yra perspektyviausia rišamoji medžiaga vandeninėms sistemoms. Nustatyta, kad poli(vinilbutiralis-ko-vinilo alkoholis-ko-vinilacetatas) (PVBA) kopolimeras yra geriausiai veikiantis tiesioginis rišiklis. PVBA pagrindu pagaminti kompozitiniai elektrodai pasižymi geru talpos stabilumu, panašiu į PVDF. Kiti PVBA privalumai - suderinamumas su mažiau toksiškais tirpikliais, tokiais kaip izopropanolis, ir didesnė veikliosios medžiagos masė. Polivinilo alkoholio ir akrilo rūgšties kopolimeras taip pat pasižymi geru talpos stabilumu, panašiu į PVDF. Talpos degradacija ciklinimo metu buvo siejamas su išbrinkimu dėl elektrolitų šarmėjimo. Svarbiausias šios rišamosios medžiagos privalumas – tirpumas vandenyje, todėl ji yra ekologiškiausias šiame tyrime nustatytas rišiklis.

## ACKNOWLEDGEMENTS

I am eternally grateful for this chance to explore the study subject as well as the limits of my character. The terrors persisted, but so did I. Completion of this research would not be possible without a favourable star alignment and lots of external help. For the latter I would like to express my gratitude to:

My supervisor Linas Vilčiauskas for setting a high bar for what great mentorship should look like. The credit of trust You gave me felt, at times, unearned, but nonetheless motivating and encouraging. I can only hope I will someday be as hardworking and dedicated as You.

Jurgis Pilipavičius for being involved and supportive (majority of time) of my scientific shenanigans and having immense tolerance to the nonsense that sometimes came out of my mouth.

Gintarė for being a partner in lab, in lunch and in crime. Our office was always filled with a friendly chatter and shared enthusiasm for future discoveries. Your company was a cherry on the top of my academic life.

Davit for homemade muffins and disagreeing with me on so many occasions. It made me master my googling – a useful skill, indeed.

Special thanks to Skirmantė and Monika for timely validation of my feelings and provision of much needed reassurance and support. Your encouragement was not lost on me.

The rest of the team: Milda Petrulevičienė, Jurga Juodkazytė, Laurynas Staišiūnas for their assistance in navigating the complicated world of electrochemistry and being great teammates.

DBU foundation., Prof. Philipp Adelhelm and his group for making my Humboldt University of Berlin fellowship possible.

My husband, Tadas, who was my rock during this time. With his support everything felt manageable.

Family and friends who had no idea of what I am doing but were supportive anyways. Especially my mom, who always wished for a doctor in the family.

My friends Laura and Vaidas, who actually had an idea about what am I doing and were patient listeners and motivators through all this journey.

## CURRICULUM VITAE

Name and surname      Nadežda Traškina  
Email                      Nadezda.traskina@ftmc.lt

### Education

**2020 – 2025**              Chemistry N003 doctoral studies, Centre for Physical Sciences and Technology, Department of chemical engineering.

**2016 – 2019**              Master's studies in nanomaterial's chemistry in Vilnius University, Faculty of Chemistry and Geosciences, department of applied chemistry.

**2012 – 2016**              Bachelor's studies in nanotechnology and material science in Vilnius University, Faculty of Chemistry, department of applied chemistry.

**2000 – 2012**              Lukiškių secondary school, Vilnius, Lithuania.

### Fellowships

**2015.02 – 2015.05**      Student's scientific research funded by Lithuanian Science Academy in Vilnius University, Faculty of Chemistry.

**2015.08 – 2015.11**      Internship in biomolecular design laboratory in iNANO institute, Denmark

**2016.07 – 2016.10**      Absolvent's internship in bioorganometallic chemistry laboratory in ITQB institute, Portugal.

**2024.02 – 2024.08**      Fellowship in Humboldt University of Berlin funded by the CEE programme at the German Federal Environmental Foundation (DBU).

### Work experience

**2016.10 – 2017.02**      Lab technician, JSC „Veika“

**2017.02 – 2020.10**      Researcher, JSC „Veika“

**2020.11 – 2022.11**      Engineer, Centre for Physical Sciences and Technology, department of chemical engineering.

**2022.11 –**                  Junior researcher, Centre for Physical Sciences and Technology, department of chemical engineering.

**2022.02 – 2023.05**      Junior Researcher in 01.2.2-LMTK-718-02-0005 project “Understanding and Applications of

- Aqueous Na-ion Technologies for Energy Storage (NaAquaCell)”
- 2023.05 –** Junior Researcher in P-MIP-23-146 project “Investigation of degradation and aging processes of NASICON type materials in aqueous media: towards in situ NMR (ELEGRANT)”
- 2025.01 –** Junior Researcher in project “Sustainable Electrochemical Recovery of Zn-Mn-O Materials from spent alkaline non-rechargeable batteries for rechargeable applications” (SusEReMat) from the Polish National Science Centre and Lithuanian Research Council DAINA3.



## PUBLICATIONS AND CONFERENCES

Included in thesis:

- Milda Petrulėvičienė, Nadežda Traškina, Jurgis Pilipavičius, Jurga Juodkazytė, Linas Vilčiauskas. The Use of Reductive Agents for Developing Capacity Balanced Aqueous Sodium-Ion Batteries. *Batteries and Supercaps* **6**, e202300129 (2023)
- Nadežda Traškina, Gintarė Gečė, Jurgis Pilipavičius, Linas Vilčiauskas. Polydopamine Derived  $\text{NaTi}_2(\text{PO}_4)_3$  - Carbon Core-Shell Nanostructures for Aqueous Batteries and Deionization Cells. *ACS Applied Nano Materials* **6**, 11780–11787 (2023).
- Jurgis Pilipavičius, Nadežda Traškina, Jurga Juodkazytė, Linas Vilčiauskas. The mechanism of  $\text{NaTi}_2(\text{PO}_4)_3$  aqueous electrochemical degradation revisited. *Electrochimica Acta* **465**, 142993 (2023).
- Linas Vilčiauskas, Jurga Juodkazyte, Jurgis Pilipavicius, Milda Petrulėvičienė, Nadezda Traskina. Aqueous Electrochemical Energy Storage Cell and A Method for Manufacturing the Same (*US2024-0243353A1*)
- Nadežda Traškina, Paulina Nemanaitė, Jurgis Pilipavičius, Vytautas Klimavičius. Linas Vilčiauskas Aqueous Hybrid Electrolytes for Sodium-Ion Batteries (*in preparation*).

Not included in thesis:

- Gintarė Gečė, Jurgis Pilipavičius, Nadežda Traškina, Audrius Drabavičius, Linas Vilčiauskas. Solvothermal Engineering of  $\text{NaTi}_2(\text{PO}_4)_3$  Nanomorphology for Applications in Aqueous Na-Ion Batteries. *ACS Sustainable Chemistry & Engineering* **11**, 3429-3436 (2023).
- Vytautas Klimavičius, Nadežda Traškina, Aurimas Dubauskas, Matas Manionis, Jurgis Pilipavičius, and Linas Vilčiauskas. Multinuclear Solid-State NMR Study of the Aqueous Solid-Electrolyte Interphase Formation in  $\text{NaTi}_2(\text{PO}_4)_3$ . *ACS Applied Energy Materials* **7**, 11665-11669 (2024).

Conferences:

- “Open Readings” (online, 2021-03-15 – 18). Poster presentation: “Optimization of anode preparation process for aqueous Na-ion batteries”.

- “Advanced Materials and Technologies” (Palanga, 2021-08-23 – 27). Poster presentation: “Precisely controlled carbon coating of  $\text{NaTi}_2(\text{PO}_4)_3$  for enhanced electrochemical performance”.
- “Chemistry and Chemical Technology” (Vilnius, 2021-09-24). Poster presentation: “Tuneable carbon coating of  $\text{NaTi}_2(\text{PO}_4)_3$  for improved battery performance”.
- “FizTeCh” (Vilnius, 2021-10-20 – 21). Oral presentation: “Optimization of the carbon coating of active materials for aqueous Na-ion batteries”.
- “RSCBatteries Twitter Poster Conference” (online, 2021-12-07 – 08). Poster title: “Optimization of anode preparation process for aqueous Na ion batteries”.
- “Open Readings” (online, 2022-03-15 – 18). Poster presentation: “Adjusting electrolyte for hydrogen evolution suppression in Na-ion aqueous batteries”.
- “eSPARK: International Summer School on Experimental Electrochemistry” (Warsaw, Poland 2022-09-18 – 25). Poster presentation: “Effective hydrogen evolution suppression in Na-ion aqueous batteries”.
- “FizTeCh” (Vilnius, 2022-10-19 – 20). Oral presentation: “Effective hydrogen evolution suppression in Na-ion aqueous batteries”.
- “International Society of Electrochemistry (ISE) 74<sup>th</sup> Annual Meeting” (Lyon 2023-09-03 – 08). Poster presentation: “Alternative binders for Na-ion aqueous batteries”.
- “FizTeCh” (Vilnius, 2023-10-18 – 20). Oral presentation: “CNC based binders for Na-ion aqueous batteries”.

## LIST OF REFERENCES

1. Xu, G. *et al.* Challenges in Developing Electrodes, Electrolytes, and Diagnostics Tools to Understand and Advance Sodium-Ion Batteries. *Adv Energy Mater* **8**, 1702403 (2018).
2. Sun, T. *et al.* Path to net zero is critical to climate outcome. *Sci Rep* **11**, 1–10 (2021).
3. Guan, Y. *et al.* Burden of the global energy price crisis on households. *Nat Energy* **8**, 304–316 (2023).
4. Frischmann, C. J. *et al.* The Global South is the climate movement’s unsung leader. *Nat. Clim. Change* **12**, 410–412 (2022).
5. Goodenough, J. B. Batteries. 1053–1061 (2013).
6. World Energy Outlook 2022.
7. Chapter 5 - Alessandro Volta. *Late Eighteenth Century European Scientists*, 127–142 (1966).
8. Xie, J. & Lu, Y. C. A retrospective on lithium-ion batteries. *Nat Commun* **11**, 9–12 (2020).
9. Fichtner, M. *et al.* Rechargeable Batteries of the Future – The State of the Art from a BATTERY 2030+ Perspective. *Adv Energy Mater* **12**, (2022).
10. May, G. J. *et al.* Lead batteries for utility energy storage: A review. *J. Energy Storage* **15**, 145–157 (2018).
11. Whittingham, M. S. Lithium Batteries: 50 Years of Advances to Address the Next 20 Years of Climate Issues. *Nano Lett* **20**, 8435–8437 (2020).
12. Fichtner, M. *et al.* Rechargeable Batteries of the Future—The State of the Art from a BATTERY 2030+ Perspective. *Adv Energy Mater* **12**, (2022).
13. Schmidt-Rohr, K. How Batteries Store and Release Energy: Explaining Basic Electrochemistry. *J Chem Educ* **95**, 1801–1810 (2018).
14. Wulandari, T. *et al.* Lithium-based batteries, history, current status, challenges, and future perspectives. *Battery Energy* **2**, (2023).
15. Olabi, A. G *et al.* Rechargeable batteries: Technological advancement, challenges, current and emerging applications. *Energy J* **266**, 126408 (2023).
16. Deng, C. *et al.* Recent advances in rocking chair batteries and beyond. *Energy Storage Mater* **60** (2023).
17. Choi, S. *et al.* Revisiting Classical Rocking Chair Lithium-Ion Battery. *Macromol. Res* **28**, 1175–1191 (2020).
18. Olabi, A. G. *et al.* Rechargeable batteries: Technological advancement, challenges, current and emerging applications. *Energy* **266**, 126408 (2023).

19. Goodenough, J. B. & Park, K.-S. The Li-Ion Rechargeable Battery: A Perspective. *J Am Chem Soc* **135**, 1167–1176 (2013).
20. Varzi, A. *et al.* Current status and future perspectives of lithium metal batteries. *J Power Sources* **480**, (2020).
21. Park, S. *et al.* Electrochemical Properties of  $\text{NaTi}_2(\text{PO}_4)_3$  Anode for Rechargeable Aqueous Sodium-Ion Batteries. *J Electrochem Soc* **158**, A1067 (2011).
22. Vaalma, C. *et al.* A cost and resource analysis of sodium-ion batteries. *Nat Rev Mater* **3**, 18013 (2018).
23. Begum, W. *et al.* A comprehensive review on the sources, essentiality and toxicological profile of nickel. *RSC Adv* **12**, 9139–9153 (2022).
24. Yadav, P. *et al.* Sodium-based batteries: development, commercialization journey and new emerging chemistries. *Oxf. Open Mater. Sci* **3** (2023).
25. Liu, T. *et al.* Exploring competitive features of stationary sodium ion batteries for electrochemical energy storage. *Energy Environ Sci* **12**, 1512–1533 (2019).
26. Tarascon, J.-M. Na-ion versus Li-ion Batteries: Complementarity Rather than Competitiveness. *Joule* **4**, 1616–1620 (2020).
27. Zhou, W. *et al.* Recent Advance in Ionic-Liquid-Based Electrolytes for Rechargeable Metal-Ion Batteries. *Adv. Sci* **8** (2021).
28. Zhao, L. *et al.* Engineering of Sodium-Ion Batteries: Opportunities and Challenges. *Eng. J* **24**, 172–183 (2023).
29. Nayak, P. K. *et al.* From Lithium-Ion to Sodium-Ion Batteries: Advantages, Challenges, and Surprises. *Angew Chem Int Ed Engl* **57**, 102–120 (2018).
30. Lyu, L. *et al.* Graphite Co-Intercalation Chemistry in Sodium Ion Batteries. *Batter Supercaps* **8** (2024).
31. Ponrouch, A. *et al.* Towards high energy density sodium ion batteries through electrolyte optimization. *Energy Environ Sci* **6**, 2361–2369 (2013).
32. Hasa, I. *et al.* Challenges of Today for Na-Based Batteries of the Future: From Materials to Cell Metrics. *J. Power Sources* **482** (2020).
33. Chen, S. *et al.* Challenges and Perspectives for NASICON-Type Electrode Materials for Advanced Sodium-Ion Batteries. *Adv Mater* **29**, 1700431 (2017).
34. Goodenough, J. B. Batteries. 1053–1061 (2013).
35. Zhao, Y. *et al.* Considerations of advanced aqueous batteries recycling: A perspective. *Energy Chem* **93**, 46–54 (2024).

36. Tang, W. *et al.* Aqueous rechargeable lithium batteries as an energy storage system of superfast charging. *Energy Environ Sci* **6**, 2093–2104 (2013).
37. Bin, D. *et al.* Progress in Aqueous Rechargeable Sodium-Ion Batteries. *Adv Energy Mater* **8**, 1703008 (2018).
38. Rao, R. *et al.* Issues and challenges facing aqueous sodium-ion batteries toward practical applications. *Battery Energy* **3**, (2024).
39. Qiao, S. *et al.* Advanced Anode Materials for Rechargeable Sodium-Ion Batteries. *ACS Nano* **17**, 11220–11252 (2023).
40. Li, Y. *et al.* Review on layered oxide cathodes for sodium-ion batteries: Degradation mechanisms, modification strategies, and applications. *Interdisciplinary Materials* **4** (2025)
41. Jin, T. *et al.* Polyanion-type cathode materials for sodium-ion batteries. *Chem Soc Rev* **49**, 2342–2377 (2020).
42. Zhai, J. *et al.* Suppressing the irreversible phase transition from P2 to O2 in sodium-layered cathode via integrating P2- and O3-type structures. *Mater Today Energy* **29**, 101106 (2022).
43. Zuo, W. *et al.* Layered Oxide Cathodes for Sodium-Ion Batteries: Storage Mechanism, Electrochemistry, and Techno-economics. *Acc Chem Res* **56**, 284–296 (2023).
44. Zhang, Y. *et al.* Three-dimensional lamination-like P2- $\text{Na}_{2/3}\text{Ni}_{1/3}\text{Mn}_{2/3}\text{O}_2$  assembled with two-dimensional ultrathin nanosheets as the cathode material of an aqueous capacitor battery. *Electrochim Acta* **148**, 195–202 (2014).
45. Gu, M. *et al.* Research progress of oxygen redox in sodium-layered oxides. *Battery Energy* **3**, 20230046 (2024).
46. Campéon, B. D. L. *et al.* Mechanistic study on moisture exposure of Ti-based layered oxides for sodium storage applications. *J Mater Chem A Mater* **13** (2025)
47. He, B. *et al.* Conversion Synthesis of Self-Standing Potassium Zinc Hexacyanoferrate Arrays as Cathodes for High-Voltage Flexible Aqueous Rechargeable Sodium-Ion Batteries. *Small* **15**, 1905115 (2019).
48. Gao, Y. *et al.* A 30-year overview of sodium-ion batteries. *Carbon Energy* **6** (2024).
49. Qian, J. *et al.* Prussian Blue Cathode Materials for Sodium-Ion Batteries and Other Ion Batteries. *Adv Energy Mater* **8**, 1702619 (2018).
50. Bauer, A. *et al.* The Scale-up and Commercialization of Nonaqueous Na-Ion Battery Technologies. *Adv Energy Mater* **8**, 1702869 (2018).

51. Liu, Q. *et al.* The Cathode Choice for Commercialization of Sodium-Ion Batteries: Layered Transition Metal Oxides versus Prussian Blue Analogs. *Adv. Funct. Mater* **30** (2020).
52. Liu, X. *et al.* Defect Engineering in Prussian Blue Analogs for High-Performance Sodium-Ion Batteries. *Adv Energy Mater* **12**, 2202532 (2022).
53. Gao, Y. *et al.* Towards defect-free Prussian, blue-based battery electrodes. *J Alloys Compd* **950**, 169886 (2023).
54. Barpanda, P. *et al.* Polyanionic Insertion Materials for Sodium-Ion Batteries. *Adv Energy Mater* **8**, 1703055 (2018).
55. Masquelier, C. & Croguennec, L. Polyanionic (Phosphates, Silicates, Sulfates) Frameworks as Electrode Materials for Rechargeable Li (or Na) Batteries. *Chem Rev* **113**, 6552–6591 (2013).
56. Hasa, I. *et al.* Sodium-Ion Battery based on an Electrochemically Converted NaFePO<sub>4</sub> Cathode and Nanostructured Tin–Carbon Anode. *ChemPhysChem* **15**, 2152–2155 (2014).
57. Gao, R.-M. *et al.* Recent advances and prospects of layered transition metal oxide cathodes for sodium-ion batteries. *Energy Storage Mater* **30**, 9–26 (2020).
58. Hong, H. Y.-P. Crystal structures and crystal chemistry in the system Na<sub>1+x</sub>Zr<sub>2</sub>Si<sub>x</sub>P<sub>3-x</sub>O<sub>12</sub>. *Mater Res Bull* **11**, 173–182 (1976).
59. Goodenough, J. B. *et al.* Fast Na<sup>+</sup>-ion transport in skeleton structures. *Mater Res Bull* **11**, 203–220 (1976).
60. Jian, Z. *et al.* NASICON-Structured Materials for Energy Storage. *Adv Mater* **29**, 1601925 (2017).
61. Anantharamulu, N. *et al.* A wide-ranging review on Nasicon type materials. *J Mater Sci* **46**, 2821–2837 (2011).
62. Pang, G. *et al.* Synthesis of NASICON-type structured NaTi<sub>2</sub>(PO<sub>4</sub>)<sub>3</sub>–graphene nanocomposite as an anode for aqueous rechargeable Na-ion batteries. *Nanoscale* **6**, 6328–6334 (2014).
63. Delmas, C., Cherkaoui, F., Nadiri, A. & Hagemuller, P. A nasicon-type phase as intercalation electrode: NaTi<sub>2</sub>(PO<sub>4</sub>)<sub>3</sub>. *Mater Res Bull* **22**, 631–639 (1987).
64. Wu, M. *et al.* NASICON-Structured NaTi<sub>2</sub>(PO<sub>4</sub>)<sub>3</sub> for Sustainable Energy Storage. *Nano-Micro Lett* **11**, s40820-019-0273-1 (2019).
65. Liang, Y. *et al.* Universal quinone electrodes for long cycle life aqueous rechargeable batteries. *Nat Mater* **16**, 841–848 (2017).
66. Kim, Y. *et al.* High-Capacity Anode Materials for Sodium-Ion Batteries. *Chem. – Eur. J* **20**, 11980–11992 (2014).

67. Wu, C.-Y. *et al.* High-rate  $\text{NaMo}_{0.05}\text{Ti}_{1.95}(\text{PO}_4)_3$  for aqueous sodium-ion battery anode material. *MRS Energy Sustain* **9**, 350–359 (2022).
68. Gu, C. *et al.* Polymerization increasing the capacitive charge storage for better rate performance: A case study of electrodes in aqueous sodium-ion capacitors. *Battery Energy* **1**, 20220031 (2022).
69. Li, X.-T. *et al.* Hydrogen isotope effects: A new path to high-energy aqueous rechargeable Li/Na-ion batteries. *eScience* **3**, 100121 (2023).
70. Miranda, D. *et al.* Theoretical simulation of the optimal relation between active material, binder and conductive additive for lithium-ion battery cathodes. *Energy J* **172**, 68–78 (2019).
71. Xiao, W. *et al.* Understanding the Critical Role of Binders in Phosphorus/Carbon Anode for Sodium-Ion Batteries through Unexpected Mechanism. *Adv Funct Mater* **30**, 2000060 (2020).
72. Rajeevan, S., John, S. & George, S. C. The effect of poly(vinylidene fluoride) binder on the electrochemical performance of graphitic electrodes. *J Energy Storage* **39**, 102654 (2021).
73. Bresser, D. *et al.* Alternative binders for sustainable electrochemical energy storage – the transition to aqueous electrode processing and bio-derived polymers. *Energy Environ Sci* **11**, 3096–3127 (2018).
74. Zheng, G. *et al.* Per- And Polyfluoroalkyl Substances (PFAS) in Breast Milk- And Trends for Current-Use PFAS. *Environ Sci Technol* **55**, 7510–7520 (2021).
75. Cousins, I. T. *et al.* Outside the Safe Operating Space of a New Planetary Boundary for Per- and Polyfluoroalkyl Substances (PFAS). *Environ Sci Technol* **56**, 11172–11179 (2022).
76. Zhang, W. *et al.* Sodium-ion battery anodes: Status and future trends. *EnergyChem* **1**, 100012 (2019).
77. Yin, J. *et al.* Synthesis strategies of hard carbon anodes for sodium-ion batteries. *MRE* **4** (2024).
78. Yi, J. & Xia, Y. Advanced aqueous batteries: Status and challenges. *MRS Energy Sustain* **9**, 106–128 (2022).
79. Schneider, C. A. *et al.* NIH Image to ImageJ: 25 years of image analysis. *Nat Methods* **9**, 671–675 (2012).
80. Yang, A. *et al.* A comprehensive investigation of lithium-ion battery degradation performance at different discharge rates. *J Power Sources* **443**, (2019).
81. Raza, H. *et al.* Li-S Batteries: Challenges, Achievements and Opportunities. *EER* **6**, 29 (2023).

82. Tang, Z. *et al.* Improving the Initial Coulombic Efficiency of Carbonaceous Materials for Li/Na-Ion Batteries: Origins, Solutions, and Perspectives. *EER* **6**, 8 (2023).
83. Ding, C. *et al.* Advances in Mn-Based Electrode Materials for Aqueous Sodium-Ion Batteries. *Nano-Micro Letters* **15** (2023).
84. Tian, R. *et al.* Quantifying the Effect of Electronic Conductivity on the Rate Performance of Nanocomposite Battery Electrodes. *ACS Appl Energy Mater* **3**, 2966–2974 (2020).
85. Jian, Z., Hu, Y. S., Ji, X. & Chen, W. NASICON-Structured Materials for Energy Storage. *Adv Mater* **29**, (2017).
86. Liu, X. *et al.* A promising mechanical ball-milling method to synthesize carbon-coated Co<sub>9</sub>S<sub>8</sub> nanoparticles as high-performance electrode for supercapacitor. *J Mater Sci* **52**, 13552–13560 (2017).
87. Bommier, C. *et al.* Sodium ion insertion in hollow carbon nanowires for battery applications. *Nano Lett* **4**, 1870 (2013).
88. Li, B. *et al.* Superior Reversibility of NASICON-Na<sub>3.5</sub>Mn<sub>0.5</sub>V<sub>1.5</sub>(PO<sub>4</sub>)<sub>3</sub> Cathode Enabled by Dual-Carbon Conductive Network. *J Alloys Compd* **977**, 1–8 (2024).
89. Li, P. *et al.* Dual or multi carbonaceous coating strategies for next-generation batteries. *J Mater Chem A Mater* **6**, 1900–1914 (2018).
90. Kondo, H. *et al.* Influence of the Active Material on the Electronic Conductivity of the Positive Electrode in Lithium-Ion Batteries. *J Electrochem Soc* **166**, A1285–A1290 (2019).
91. Shi, Y. *et al.* Research progress of interface protective layer materials in zinc anode. *J Energy Storage* **80** (2024).
92. Guan, P. *et al.* Recent progress of surface coating on cathode materials for high-performance lithium-ion batteries. *J. Energy Chem* **43**, 220–235 (2020).
93. Wang, F. *et al.* Engineering of carbon and other protective coating layers for stabilizing silicon anode materials. *Carbon Energy* **1**, 219–245 (2019).
94. Raj, H. & Sil, A. Effect of carbon coating on electrochemical performance of LiFePO<sub>4</sub> cathode material for Li-ion battery. *Ionics (Kiel)* **24**, 2543–2553 (2018).
95. Peng, K. *et al.* Mechanical integrity of conductive carbon-black-filled aqueous polymer binder in composite electrode for lithium-ion battery. *Polymers (Basel)* **12**, 1–16 (2020).
96. Min, B. S. *et al.* NaTi<sub>2</sub>(PO<sub>4</sub>)<sub>3</sub> nanoparticles embedded in double carbon networks as a negative electrode for an aqueous sodium-polyiodide flow battery. *Electrochim Acta* **361**, 137075 (2020).



97. Yaroslavtsev, A. B. & Stenina, I. A. Carbon coating of electrode materials for lithium-ion batteries. *Surf. Innov* **9**, 92–110 (2020).
98. Jharia, M. *et al.* Research progress on efficient battery thermal management system (BTMs) for electric vehicles using composite phase change materials with liquid cooling and nanoadditives. *J Therm Anal Calorim* **149** (2024)
99. Casanova, A. *et al.* Carbon black as conductive additive and structural director of porous carbon gels. *J Mater* **13**, (2020).
100. Taherian, R. & Kausar, A. Electrical Conductivity in Polymer-Based Composites: Experiments, Modelling, and Applications. 19–40 (2018).
101. Higgins, T. M. *et al.* Effect of Percolation on the Capacitance of Supercapacitor Electrodes Prepared from Composites of Manganese Dioxide Nanoplatelets and Carbon Nanotubes. *ACS Nano* **8**, 9567–9579 (2014).
102. Raymundo-Piñero, E. *et al.* Carbon Nanotubes as Nanotexturing Agents for High Power Supercapacitors Based on Seaweed Carbons. *ChemSusChem* **4**, 943–949 (2011).
103. Zhang, B. *et al.* Percolation threshold of graphene nanosheets as conductive additives in  $\text{Li}_4\text{Ti}_5\text{O}_{12}$  anodes of Li-ion batteries. *Nanoscale* **5**, 2100–2106 (2013).
104. Takahashi, K. *et al.* Mechanical Degradation of Graphite/PVDF Composite Electrodes: A Model-Experimental Study. *J Electrochem Soc* **163**, A385–A395 (2016).
105. Grillet, A. M. *et al.* Conductivity Degradation of Polyvinylidene Fluoride Composite Binder during Cycling: Measurements and Simulations for Lithium-Ion Batteries. *J Electrochem Soc* **163**, A1859 (2016).
106. Zheng, H. *et al.* Cooperation between Active Material, Polymeric Binder and Conductive Carbon Additive in Lithium Ion Battery Cathode. *J. Phys. Chem. C* **116**, 4875–4882 (2012).
107. Ebner, E. *et al.* Carbon blacks for lead-acid batteries in micro-hybrid applications – Studied by transmission electron microscopy and Raman spectroscopy. *J Power Sources* **222**, 554–560 (2013).
108. Bauer, W., Nötzel, D., Wenzel, V. & Nirschl, H. Influence of dry mixing and distribution of conductive additives in cathodes for lithium ion batteries. *J Power Sources* **288**, 359–367 (2015).
109. Sim, S. *et al.* Use of carbon coating on  $\text{LiNi}_{0.8}\text{Co}_{0.1}\text{Mn}_{0.1}\text{O}_2$  cathode material for enhanced performances of lithium-ion batteries. *Sci Rep* **10**, 1–9 (2020).

110. Zhang, D. *et al.* Effect of pyrolysis temperature on carbon materials derived from reed residue waste biomass for use in supercapacitor electrodes. *J. Phys. Chem. Solids* **178**, (2023).
111. Kim, J. K. *et al.* Electrochemical properties of LiFePO<sub>4</sub>/C composite cathode material: Carbon coating by the precursor method and direct addition. *J. Phys. Chem. Solids* **69**, 1257–1260 (2008).
112. Niu, Y. *et al.* M. Pyro-synthesis of a nanostructured NaTi<sub>2</sub>(PO<sub>4</sub>)<sub>3</sub>/C with a novel lower voltage plateau for rechargeable sodium-ion batteries. *J Colloid Interface Sci* **474**, 88–92 (2016).
113. Tomczyk, A. *et al.* Biochar physicochemical properties: pyrolysis temperature and feedstock kind effects. *Rev Environ Sci Biotechnol* **19**, 191–215 (2020).
114. Li, H. & Zhou, H. Enhancing the performances of Li-ion batteries by carbon-coating: Present and future. *ChemComm* **48**, 1201–1217 (2012).
115. Wang, J. & Sun, X. Understanding and recent development of carbon coating on LiFePO<sub>4</sub> cathode materials for lithium-ion batteries. *Energy Environ Sci* **5**, 5163–5185 (2012).
116. Sung, M. K. *et al.* Norepinephrine: Material-independent, multifunctional surface modification reagent. *J Am Chem Soc* **131**, 13224–13225 (2009).
117. Postma, A. *et al.* Self-polymerization of dopamine as a versatile and robust technique to prepare polymer capsules. *J. Mater. Chem. A* **21**, 3042–3044 (2009).
118. Wang, Y. *et al.* The design of a LiFePO<sub>4</sub>/carbon nanocomposite with a core-shell structure and its synthesis by an *in situ* polymerization restriction method. *Angew. Chem., Int. Ed* **47**, 7461–7465 (2008).
119. Han, B. *et al.* Nitrogen-doped carbon decorated LiFePO<sub>4</sub> composite synthesized via a microwave heating route using polydopamine as carbon-nitrogen precursor. *Ceram Int* **42**, 2789–2797 (2016).
120. Liu, S. *et al.* Porous Si@C composite anode material prepared using dopamine as a carbon source for high-performance lithium-ion batteries. *Int J Electrochem Sci* **15**, (2020).
121. Ye, Q. *et al.* Bioinspired catecholic chemistry for surface modification. *Chem Soc Rev* **40**, 4244–4258 (2011).
122. Quilty, C. D. *et al.* Electron and Ion Transport in Lithium and Lithium-Ion Battery Negative and Positive Composite Electrodes. *Chem Rev* **123** (2022).
123. Yaroslavtsev, A. B. & Stenina, I. A. Carbon coating of electrode materials for lithium-ion batteries. *Surf Innov* **9**, 92–110 (2020).

124. Tutlienè, S. *et al.* Electrochemical Performance of Sol-Gel Synthesized  $\text{NaTi}_2(\text{PO}_4)_3$  - Carbon Composites as Aqueous Na-Ion Battery Anodes. *J Electrochem Soc* **168**, 060545 (2021).
125. Palla, S. *et al.* Characterization, conductivity and photocatalytic studies of  $\text{AHfM}(\text{PO}_4)_3$  (A = Na and Ag; M = Ti and Zr) powders synthesized by sol-gel method. *J Solgel Sci Technol* **67**, 507–518 (2013).
126. Pang, G. *et al.* Mesoporous  $\text{NaTi}_2(\text{PO}_4)_3$ /CMK-3 nanohybrid as anode for long-life Na-ion batteries. *J Mater Chem A Mater* **2**, 20659–20666 (2014).
127. Dreyer, D. R. *et al.* Elucidating the structure of poly(dopamine). *Langmuir* **28**, 6428–6435 (2012).
128. Kong, J. *et al.* Highly electrically conductive layered carbon derived from polydopamine and its functions in  $\text{SnO}_2$ -based lithium ion battery anodes. *ChemComm* **48**, 10316–10318 (2012).
129. Daud, N. A. *et al.* Functionalizing graphene oxide with alkylamine by gamma-ray irradiation method. *Nanomaterials* **7**, (2017).
130. Wang, N. *et al.* N-doped catalytic graphitized hard carbon for high-performance lithium/sodium-ion batteries. *Sci Rep* **8**, 1–8 (2018).
131. Cong, R. *et al.* Three-dimensional network of nitrogen-doped carbon matrix-encapsulated Si nanoparticles/carbon nanofibers hybrids for lithium-ion battery anodes with excellent capability. *Sci Rep* **12**, (2022).
132. Plečkaitytė, G. *et al.* Understanding and mitigation of  $\text{NaTi}_2(\text{PO}_4)_3$  degradation in aqueous Na-ion batteries. *J Mater Chem A Mater* **9**, 12670–12683 (2021).
133. Mohamed, A. I. & Whitacre, J. F. Capacity Fade of  $\text{NaTi}_2(\text{PO}_4)_3$  in Aqueous Electrolyte Solutions: Relating pH Increases to Long Term Stability. *Electrochim Acta* **235**, 730–739 (2017).
134. Zhan, X. & Shirpour, M. Evolution of solid/aqueous interface in aqueous sodium-ion batteries. *ChemComm* **53**, 204–207 (2017).
135. Yang, W. *et al.* Unravelling capacity fading mechanisms in sodium vanadyl phosphate for aqueous sodium-ion batteries. *J Colloid Interface Sci* **627**, 913–921 (2022).
136. Tekin, B. Nafion-protected  $\text{Na}_3\text{V}_2(\text{PO}_4)_3$  electrodes for aqueous zinc-ion batteries: A breakthrough in dissolution resistance and electrochemical enhancement. *MSEB* **307**, 117534 (2024).
137. Reynolds, C. *et al.* Impact of Formulation and Slurry Properties on Lithium-ion Electrode Manufacturing. *Batter Supercaps* **7**, (2024).
138. Shim, J. & Striebel, K. A. Effect of electrode density on cycle performance and irreversible capacity loss for natural graphite anode in lithium-ion batteries. *J Power Sources* **119–121**, 934–937 (2003).

139. Fernandez-Diaz, L. *et al.* Mixing methods for solid state electrodes: Techniques, fundamentals, recent advances, and perspectives. *Chem. Eng. J* **464** (2023).
140. Trevey, J. E. *et al.* High Power Nanocomposite  $\text{TiS}_2$  Cathodes for All-Solid-State Lithium Batteries. *J Electrochem Soc* **158**, A1282 (2011).
141. Bockholt, H. *et al.* Intensive powder mixing for dry dispersing of carbon black and its relevance for lithium-ion battery cathodes. *Powder Technol* **297**, 266–274 (2016).
142. Clough, M. T. Organic electrolyte solutions as versatile media for the dissolution and regeneration of cellulose. *Green Chemistry* **19**, 4754–4768 (2017).
143. Chen, R. *et al.* A Comparative Review of Electrolytes for Organic-Material-Based Energy-Storage Devices Employing Solid Electrodes and Redox Fluids. *ChemSusChem* **13**, 2205–2219 (2020).
144. An, Z. *et al.* Effect of organic electrolyte and voltage on electrochemical performances and capacity degradation for Li-ion hybrid capacitors based on  $\text{Nb}_2\text{O}_5$  anode. *Solid State Electrochem* (2025)
145. Lu, L. *et al.* A review on the key issues for lithium-ion battery management in electric vehicles. *J Power Sources* **226**, 272–288 (2013).
146. Ribière, P. *et al.* Investigation on the fire-induced hazards of Li-ion battery cells by fire calorimetry. *Energy Environ Sci* **5**, 5271–5280 (2012).
147. Ahn, H. *et al.* Challenges and possibilities for aqueous battery systems. *Commun Mater* **4**, (2023).
148. Miao, L. *et al.* Three-functional ether-based co-solvents for suppressing water-induced parasitic reactions in aqueous Zn-ion batteries. *Energy Storage Mater* **49**, 445–453 (2022).
149. Pilipavičius, J. *et al.* The mechanism of  $\text{NaTi}_2(\text{PO}_4)_3$  aqueous electrochemical degradation revisited. *Electrochim Acta* **465**, 142993 (2023).
150. Bayaguud, A. *et al.* Interfacial parasitic reactions of zinc anodes in zinc ion batteries: Underestimated corrosion and hydrogen evolution reactions and their suppression strategies. *Energy Chem* **64**, 246–262 (2022).
151. Wang, X. *et al.* An Aqueous Rechargeable Lithium Battery Using Coated Li Metal as Anode. *Sci Rep* **3**, (2013).
152. Nakamoto, K. *et al.* Effect of concentrated electrolyte on aqueous sodium-ion battery with sodium manganese hexacyanoferrate cathode. *Int J Electrochem* **85**, 179–185 (2017).

153. Mohamed, A. I. & Whitacre, J. F. Capacity Fade of  $\text{NaTi}_2(\text{PO}_4)_3$  in Aqueous Electrolyte Solutions: Relating pH Increases to Long Term Stability. *Electrochim Acta* **235**, 730–739 (2017).
154. Guo, Z. *et al.* Multi-functional Flexible Aqueous Sodium-Ion Batteries with High Safety. *Chem* **3**, 348–362 (2017).
155. Zhu, Z. *et al.* Hydrogen-Induced Degradation of  $\text{NaMnO}_2$ . *Chem Mater* **31**, 5224–5228 (2019).
156. Yokoyama, Y. *et al.* Origin of the Electrochemical Stability of Aqueous Concentrated Electrolyte Solutions. *J Electrochem Soc* **165**, A3299–A3303 (2018).
157. Li, Y. *et al.* Suppressing the oxygen-related parasitic reactions in  $\text{NaTi}_2(\text{PO}_4)_3$ -based hybrid capacitive deionization with cation exchange membrane. *J Colloid Interface Sci* **591**, 139–147 (2021).
158. Wu, W. *et al.* Relating Electrolyte Concentration to Performance and Stability for  $\text{NaTi}_2(\text{PO}_4)_3/\text{Na}_{0.44}\text{MnO}_2$  Aqueous Sodium-Ion Batteries. *J Electrochem Soc* **162**, A803–A808 (2015).
159. Yi, J. *et al.* Challenges, mitigation strategies and perspectives in development of zinc-electrode materials and fabrication for rechargeable zinc-air batteries. *EES* **11**, 3075–3095 (2018).
160. Xie, J. *et al.* Molecular crowding electrolytes for high-voltage aqueous batteries. *Nat Mater* **19**, 1006–1011 (2020).
161. Kilburn, D. *et al.* Molecular crowding stabilizes folded RNA structure by the excluded volume effect. *J Am Chem Soc* **132**, 8690–8696 (2010).
162. Gao, M. *et al.* Faltung einer RNA-Haarnadel in der dicht gedrängten Zelle. *Angew Chem* **128**, 3279–3283 (2016).
163. Huang, Z. *et al.* Small-Dipole-Molecule-Containing Electrolytes for High-Voltage Aqueous Rechargeable Batteries. *Adv Mater* **34**, 1–12 (2022).
164. Chen, Y. *et al.* Low Current-Density Stable Zinc-Metal Batteries Via Aqueous/Organic Hybrid Electrolyte. *Batter Supercaps* **5**, (2022).
165. Zhang, C. *et al.* A  $\text{ZnCl}_2$  water-in-salt electrolyte for a reversible Zn metal anode. *ChemComm* **54**, 14097–14099 (2018).
166. Zhao, J. *et al.* “Water-in-deep eutectic solvent” electrolytes enable zinc metal anodes for rechargeable aqueous batteries. *Nano Energy* **57**, 625–634 (2019).
167. Dou, Q. *et al.* “Water in salt/ionic liquid” electrolyte for 2.8 V aqueous lithium-ion capacitor. *Sci Bull (Beijing)* **65**, 1812–1822 (2020).
168. Nakagawa, H. & Oyama, T. Molecular Basis of Water Activity in Glycerol–Water Mixtures. *Front Chem* **7**, (2019).

169. Lam, S. Y. & Benoit, R. L. Some Thermodynamic Properties of the Dimethylsulfoxide-Water and Propylene Carbonate-Water Systems at 25 °C. *Can. J. Chem* **52** (1974).
170. Sekar, P. *et al.* Tailoring potential window of aqueous electrolyte via steric molecular engineering for high voltage supercapacitors. *Appl Mater Today* **32**, (2023).
171. Hédoux, A. *et al.* Vibrational and structural properties of amorphous n-butanol: A complementary Raman spectroscopy and X-ray diffraction study. *Chem Phys* **138**, (2013).
172. Yang, B. *et al.* Investigation of hydrogen bonding in Water/DMSO binary mixtures by Raman spectroscopy. *Spectrochim Acta A Mol Biomol Spectrosc* **228**, (2020).
173. Skaf, M. S. Molecular dynamics study of dielectric properties of water-dimethyl sulfoxide mixtures. *Phys. Chem. A* **103**, 10719–10729 (1999).
174. Nakagawa, H. & Oyama, T. Molecular Basis of Water Activity in Glycerol–Water Mixtures. *Front Chem* **7**, (2019).
175. He, Y. *et al.* Boosting sodium-storage behaviors of NASICON-type  $\text{NaTi}_2(\text{PO}_4)_3$  anode by synergistic modulations in both materials and electrolytes towards aqueous Na-ion batteries. *Electrochim Acta* **447**, (2023).
176. Wang, Y. *et al.* Strong Hydrogen-Bonded Interfacial Water Inhibiting Hydrogen Evolution Kinetics to Promote Electrochemical  $\text{CO}_2$  Reduction to  $\text{C}_2^+$ . *ACS Catal* **14**, 3457–3465 (2024).
177. Alexowsky, C. *et al.* M. Porous poly(vinylidene fluoride) membranes with tailored properties by fast and scalable non-solvent vapor induced phase separation. *J Memb Sci* **577**, 69–78 (2019).
178. Shang, W. *et al.* Insight into the self-discharge suppression of electrochemical capacitors: Progress and challenges. *Adv. Powder Mater* **2** (2023).
179. Liu, Y. *et al.* Advanced characterizations and measurements for sodium-ion batteries with NASICON-type cathode materials. *eScience* **2**, 10–31 (2022).
180. Niemeier, J. K. & Kjell, D. P. Hydrazine and Aqueous Hydrazine Solutions: Evaluating Safety in Chemical Processes. *Org Process Res Dev* **17**, 1580–1590 (2013).
181. Park, S. *et al.* Hydrazine-reduction of graphite- and graphene oxide. *Carbon N Y* **49**, 3019–3023 (2011).
182. Miao, R. & Compton, R. G. Mechanism of hydrazine oxidation at Palladium electrodes: Long-lived radical di-cation formation. *Electrochim Acta* **388**, (2021).

183. Xu, K. Nonaqueous liquid electrolytes for lithium-based rechargeable batteries. *Chem Rev* **104**, 4303–4417 (2004).
184. Goodenough, J. B. & Kim, Y. Challenges for rechargeable Li batteries. *Chem Mater* **22**, 587–603 (2010).
185. Ma, L. A. *et al.* Fundamental Understanding and Quantification of Capacity Losses Involving the Negative Electrode in Sodium-Ion Batteries. *Adv. Sci* **11**, (2024).
186. Liao, L. *et al.* Fluoroethylene carbonate as electrolyte additive to improve low temperature performance of LiFePO<sub>4</sub> electrode. *Electrochim Acta* **87**, 466–472 (2013).
187. Self, J. *et al.* The role of prop-1-ene-1,3-sultone as an additive in lithium-ion cells. *J Power Sources* **298**, 369–378 (2015).
188. Mo, W. *et al.* Designing multifunctional artificial SEI layers for long-term stability of sodium metal anodes. *J Colloid Interface Sci* **683**, 600–609 (2025).
189. Buqa, H. *et al.* Study of styrene butadiene rubber and sodium methyl cellulose as binder for negative electrodes in lithium-ion batteries. *J Power Sources* **161**, 617–622 (2006).
190. Guy, D. *et al.* New Composite Electrode Architecture and Improved Battery Performance from the Smart Use of Polymers and Their Properties. *Adv Mater* **16**, 553–557 (2004).
191. Lingappan, N. *et al.* The significance of aqueous binders in lithium-ion batteries. *RSER* **147**, 111227 (2021).
192. Pejovnik, S. *et al.* Electrochemical binding and wiring in battery materials. *J Power Sources* **184**, 593–597 (2008).
193. Saal, A. *et al.* Polymers for Battery Applications—Active Materials, Membranes, and Binders. *Adv. Energy Mater* **11** (2021).
194. Munger, C. *et al.* Corrosion Prevention by Protective Coatings Third Edition. (2014).
195. Pape, P. G. Adhesion Promoters: Silane Coupling Agents. in *Plastics Design Library* **29**, 503–517 (2011)
196. Pape, P. G. & Plueddeman, E. P. History of silane coupling agents in polymer composites. *History of Polymeric Composites* 105–139 (1986).
197. Plueddemann, E. P. Nature of Adhesion Through Silane Coupling Agents BT. *Silane Coupling Agents* 115–152 (1991).
198. Häupler, B. *et al.* Carbonyls: Powerful organic materials for secondary batteries. *Adv Energy Mater* **5**, (2015).
199. Wang, H. *et al.* Sulphur-containing phenylethynyl terminated polyimide via chemical crosslinking method for excellent thermal properties and antibacterial performance. *React Funct Polym* **186** (2023).

200. Sun, Z. *et al.* N-Type Polyoxadiazole Conductive Polymer Binders Derived High-Performance Silicon Anodes Enabled by Crosslinking Metal Cations. *ACS Appl Mater Interfaces* **15**, 12946–12956 (2023).
201. Park, Y. J. *et al.* Adhesion and rheological properties of EVA-based hot-melt adhesives. *Int J Adhes Adhes* **26**, 571–576 (2006).
202. Li, W. *et al.* Current research and development status and prospect of hot-melt adhesives: A review. *Ind. Eng. Chem. Res* **47**, 7524–7532 (2008).
203. Zhou, M. *et al.* Issues and optimization strategies of binders for aqueous zinc metal batteries. *Chem. Eng. J* **497** (2024).
204. Wang, L. *et al.* SBR-PVDF based binder for the application of SLMP in graphite anodes. *RSC Adv* **3**, 15022–15027 (2013).
205. Toigo, C. *et al.* A Method to Measure the Swelling of Water-Soluble PVDF Binder System and Its Electrochemical Performance for Lithium Ion Batteries. *J Electrochem Soc* **167**, 020514 (2020).
206. Lingappan, N. *et al.* The significance of aqueous binders in lithium-ion batteries. *RSER* **147** (2021).
207. Zhu, Z. *et al.* Enhanced anticorrosion properties of composite coatings containing polyvinyl butyral and polyaniline-carbonized polyaniline. *Prog Org Coat* **180** (2023).
208. Yu, D. Y. W. *et al.* Effect of Electrode Parameters on LiFePO<sub>4</sub> Cathodes. *J Electrochem Soc* **153**, A835 (2006).
209. Sun, J. *et al.* Effect of poly (acrylic acid)/Poly (vinyl alcohol) blending binder on electrochemical performance for lithium iron phosphate cathodes. *J Alloys Compd* **783**, 379–386 (2019).
210. Manjuladevi, R. *et al.* Mg-ion conducting blend polymer electrolyte based on poly(vinyl alcohol)-poly (acrylonitrile) with magnesium perchlorate. *Solid State Ion* **308**, 90–100 (2017).
211. Tanaka, S. *et al.* Acrylonitrile-grafted poly(vinyl alcohol) copolymer as effective binder for high-voltage spinel positive electrode. *J Power Sources* **358**, 121–127 (2017).
212. He, J. & Zhang, L. Polyvinyl alcohol grafted poly (acrylic acid) as water-soluble binder with enhanced adhesion capability and electrochemical performances for Si anode. *J Alloys Compd* **763**, 228–240 (2018).
213. Sun, J. *et al.* Effect of poly (acrylic acid)/Poly (vinyl alcohol) blending binder on electrochemical performance for lithium iron phosphate cathodes. *J Alloys Compd* **783**, 379–386 (2019).
214. Quintero, S. M. M. *et al.* Swelling and morphological properties of poly(vinyl alcohol) (PVA) and poly(acrylic acid) (PAA) hydrogels in solution with high salt concentration. *Polymer (Guildf)* **51**, 953–958 (2010).



215. Li, B. *et al.* Superior Reversibility of NASICON- $\text{Na}_{3.5}\text{Mn}_{0.5}\text{V}_{1.5}(\text{PO}_4)_3$  Cathode Enabled by Dual-Carbon Conductive Network. *J Alloys Compd* **977**, 1–8 (2024)





Vilniaus universiteto leidykla  
Saulėtekio al. 9, III rūmai, LT-10222 Vilnius  
El. p. [info@leidykla.vu.lt](mailto:info@leidykla.vu.lt), [www.leidykla.vu.lt](http://www.leidykla.vu.lt)  
[bookshop.vu.lt](http://bookshop.vu.lt), [journals.vu.lt](http://journals.vu.lt)  
Tiražas 20 egz.